REPORT

July 11, 2008
EWI Project No. 47572GTH

Continuation of Studies on Development of ODS Heat Exchanger Tubing

Final Report
Cooperative Agreement No.: DE-FC26-05NT42238

Reporting Period:
February 28, 2005 through April 15, 2008

by

Principal Authors:

Lawrence Brown, EWI
David Workman, EWI
Bimal Kad, UCSD
Gaylord Smith, SMC
Archie Robertson, FWDC
Ian Wright, ORNL

July 11, 2008

Submitted by:

Edison Welding Institute, Inc.
1250 Arthur E. Adams Drive
Columbus, OH 43221-3585

Subcontractors:

Foster Wheeler Development Corporation
Perryville Corporate Park
Clinton, NJ 08809

Dept. of Structural Engineering
University of California – San Diego
La Jolla, CA 92093-0085

Special Metals Corporation
3200 Riverside Drive
Huntington, WV 25705-1771

Oak Ridge National Laboratory
P.O. Box 2008
Oak Ridge, TN 37831

Final Report
Cooperative Agreement No.: DE-FC26-05NT42238

Project No. 47572GTH

on

Continuation of Studies on Development of ODS Heat Exchanger Tubing

to

U.S. Department of Energy
National Energy Technology Laboratory
626 Cochrans Mill Road
P.O. Box 10940
Pittsburgh, PA

July 11, 2008

Lawrence E. Brown
EDISON WELDING INSTITUTE
1250 Arthur E. Adams Drive
Columbus, OH 43221

Disclaimer

This report was prepared as an account of work sponsored by an agency of the United States Government. Neither the United States Government nor any agency thereof, nor any of their employees, makes any warranty, express or implied, or assumes any legal liability or responsibility for the accuracy, completeness, or usefulness of any information, apparatus, product or processes disclosed in this report, or represents that its use would not infringe privately owned rights. Reference herein to any specific commercial product, process, or service by trade name, trademark, manufacturer, or otherwise, does not necessarily constitute or imply its endorsement, recommendation, or favoring by the United States Government or any agency thereof. The views and opinions of authors expressed herein do not necessarily state or reflect those of the United States Government or any agency thereof.

Disclaimer of Warranties and Limitations of Liabilities

This report was prepared by the organizations named below as an account of work sponsored or co-sponsored by the U.S. Department of Energy and Special Metals Corporation (dba Huntington Alloys). Neither the U.S. Department of Energy, Special Metals Corporation, the organizations named below, nor any person acting on behalf of any of them:

(A) Makes any warranty or representation whatsoever, express or implied, (i) with respect to the use of any information, apparatus, method, process, or similar item disclosed in this report, including merchantability and fitness for a particular purpose, or (ii) that such use does not infringe on or interfere with privately owned rights, including any party's intellectual property or (iii) that this report is suitable to any particular users circumstance, or (B) assumes any responsibility for any damages or other liability whatsoever (including any consequential damages, even if DOE or any DOE Representative has been advised of the possibility of such damages) resulting from your selection or use of this report or any information, apparatus, method, process, or similar item disclosed in this report.

Special Metals Corporation (dba Huntington Alloys)	Foster Wheeler Development Corporation
Oak Ridge National Laboratory	University of California at San Diego
Edison Welding Institute	

Abstract

The Department of Energy (DOE), National Energy Technology Center (NETL), has initiated a strategic plan for the development of advanced technologies needed to design and build fossil fuel plants with very high efficiency and environmental performance. These plants, referred to as "Vision 21" and FutureGen programs by DOE, will produce electricity, chemicals, fuels, or a combination of these products, and possibly secondary products such as steam/heat for industrial use.

MA956 is a prime candidate material being considered for a high temperature heat exchanger in the "Vision 21" and FutureGen programs. This material is an oxide dispersion strengthened (ODS) alloy; however, there are some gaps in the data required to commit to the use of these alloys in a full-size plant. To fill the technology gaps for commercial production and use of the material for “Advanced Power Generation Systems” this project has performed development activity to significant increase in circumferential strength of MA956 as compared to currently available material, investigated bonding technologies for bonding tube-to-tube joints through joining development, and performed tensile, creep and fire-side corrosion tests to validate the use and fabrication processes of MA956 to heat exchanger tubing applications.

Development activities within this projected has demonstrated increased circumferential strength of MA956 tubes through flow form processing. Of the six fabrication technologies for bonding tube-to-tube joints, inertia friction welding (IFW) and flash butt welding (FBW) were identified as processes for joining MA956 tubes. Tensile, creep, and fire-side corrosion test data were generated for both base metal and weld joints. The data can be used for design of future systems employing MA956.

Based upon the positive development activities, two test probes were designed and fabricated for field exposure testing at 1204°C (~2200°F) flue gas. The probes contained tube portions with FBW and IFW welded MA956. Field testing of the probes and remaining heat exchanger design activity will be performed by Oak Ridge National Laboratory under DOE Contract DE-AC05-00OR22725.

Contents

Contents

Page

Tables

Contents

Page

Figures

Contents

Page

Contents

Contents

Contents

Page

Executive Summary

The Department of Energy (DOE), National Energy Technology Center (NETL), initiated a strategic plan for the development of advanced technologies needed to design and build fossil fuel plants with very high efficiency and environmental performance. Oxide dispersion strengthened (ODS) ferritic alloys based on FeCrAl and intermetallic Fe3Al alloys were promising materials for high-temperature, high-pressure tubing, liner and shell applications due to their creep strength at very high temperatures and excellent corrosion resistance in oxidizing, oxidizing/sulphidizing and oxidizing/chlorinating environments compared to available high-temperature alloys. Requirements for such a combination of properties are found in advanced systems being developed for utilization of fossil fuels, such as the DOE's Vision 21 and FutureGen programs and in improved gas turbines being developed for power generation.

The project goal was to investigate the applicability of MA956 alloy in the high temperature heat-exchanger tubing as proposed under the proposed DOE and NETL Vision-21 program metrics, intended to sustain internal pressures up to 6.9 MPa (1000 psi) at service temperatures of 1000-1200°C (1832-2192°F). Within the framework of this target application, the development of the ODS material and processes strived to deliver a combination of high mechanical strength at temperature and prolonged creep-life in service. Such design requirements are often at odds with each other. Current tube processing methods cause material flow in the longitudinal direction, resulting in extreme dispersoid and powder surface impurity fibering in the axial direction in ODS materials. Thus, elongated grains are produced aligned parallel to the longitudinal direction, with a fine grain spacing in the hoop direction. ODS-alloys exhibited intrinsic creep strength sufficient to meet design requirements, but the performance was exhibited only in the longitudinal direction. Ultimate failure in transverse (hoop) creep involved creep cavity concentration, which strongly depended on the dominant grain boundary orientation with respect to the loading axis. Such fibering, unless altered by post-flow forming, was expected to thwart attempts to arrive at the large transverse grain size considered essential for improved creep performance in the hoop direction.

To fill the technology gaps for commercial production and use of the material for "Advanced Power Generation Systems" this project performed development activity to:

1. Produce a MA956 tube with a significant increase in circumferential strength compared to currently available material.

2. Develop the welding technology required to produce a cost-effective joint between an ODS tube as well as to a heat resistant alloy.

3. Characterize the MA956 alloy in environments likely to be encountered on the inner diameter of the tube (working fluid side) and the outer diameter of the tube (fireside).

Post production thermo-mechanical processing in the form of ambient temperature flow forming and hot cross rolling are shown to produce a significant and reproducible improvement in creep response. Hence, the proposed notion of creep enhancement by such forming treatments had significant merit. Flow-formed processing up to 80% reduction in wall thickness had shown increased creep strength in the 800-1000°C (1472-1832°F) temperature range. Maximum test exposures of about 9900 hours and 6400 hours were recorded for tests at 975°C and 1000°C (1787°F and 1832°F), respectively.

Six candidate weld processes were investigated for joining MA956 tubing to itself as well as joining to Inconel 601. The processes investigated that appeared to be the most amenable to weld fabrication of the tubing were inertia friction welding (IFW) and flash butt welding (FBW). Evaluations of the joint creep performance for flash-upset and inertia-welded joints revealed robust performance in creep compared to baseline MA956 performance.

Corrosion testing was performed upon the Alloy 230 (Baseline), MA956 and the weld joints produced by IFW and FBW. Test specimens were coated with coal ashes and exposed to high temperature gases in electrically heated furnaces to determine the material's susceptibility to corrosion. The tests were conducted at three different temperatures with two different gas compositions and three different ashes each for 1000 hours. The results of the corrosion experiments revealed that MA956 alloy exhibited better corrosion resistance than the alloy 230. The MA956 weld surfaces sustained little to no gross wall loss after 1000 hours of exposure at 1093°C (2000°F). Metal loss, when noted, was very shallow and localized to discrete pit sites (e.g., no general wastage). The calculated corrosion rates along the MA956 weld surfaces were comparable to the base metal.

Two test probes were designed and fabricated for field exposure testing at 1204°C (~2200°F) flue gas in Duke Energy's Gibson Station Unit Number 5 Boiler. The probes contained tube portions with FBW and IFW welded MA956. Field testing of the probes and remaining heat exchanger design activity were performed by Oak Ridge National Laboratory under DOE Contract No. DE-AC05-00OR22725.

Acknowledgments

This work was conducted by the Edison Welding Institute under Cooperative Agreement DE-FC26-05NT42238 to The Department of Energy (DOE), National Energy Technology Center (NETL). The author acknowledges the work, advice and guidance of the following project team partners throughout the duration of the project:

Richard Read	The Department of Energy (DOE), National Energy Technology Center (NETL)
Horst Hack	Foster Wheeler Development Corporation (FWDC)
Greg Stanko	Foster Wheeler Development Corporation (FWDC)
Archie Robertson	Foster Wheeler Development Corporation (FWDC)
Bimal Kad	University of California, San Diego (UCSD)
Ian Wright	Oak Ridge National Laboratory (ORNL)
Gaylord Smith	Special Metals Corporation (SMC)
Vonne Linse	Regal Technologies
David Workman	Edison Welding Institute

1.0 Introduction

The Department of Energy (DOE), National Energy Technology Center (NETL), has initiated a strategic plan for the development of advanced technologies needed to design and build fossil fuel plants with very high efficiency and environmental performance. These plants, referred to as "Vision 21" and FutureGen programs by DOE, will produce electricity, chemicals, fuels, or a combination of these products, and possibly secondary products such as steam/heat for industrial use.

MA956 is a prime candidate material being considered for a high temperature heat exchanger. This material is an oxide dispersion strengthened (ODS) alloy. However, there are some gaps in the data required to commit to the use of these alloys in a full-size plant. To fill the technology gaps for commercial production and use of the material for “Advanced Power Generation Systems” this project is performing development activity to:

- Produce a MA956 tube with a significant increase in circumferential strength compared to currently available material.
- Develop the welding technology required to produce a cost-effective joint between an ODS tube as well as to a heat resistant alloy.
- Characterize the MA956 alloy in environments likely to be encountered on the inner diameter of the tube (working fluid side) and the outer diameter of the tube (fireside).
- Generate data to be used by heat exchanger designers and the ASME BPV Code.
- Analyze the data for the purpose of setting limits on the design of an MA956 heat exchanger.

2.0 Objectives

The objective of this project is to develop an INCOLOY® alloy MA956 heat exchanger tube which will lead to the design and fabrication of an MA956 full-scale tube heat exchanger. The necessary steps required for the commercial production of such a tube are: (1) produce an MA956 tube with a significant increase in circumferential strength compared to currently available material; (2) develop the welding technology required to produce a cost-effective joint between an ODS tube and an ODS tube, and a joint between an ODS tube and a heat resistant alloy; (3) determine the critical strain the MA956 material can withstand during tube bending and not undergo recrystallization during subsequent operation; (4) characterize the MA956 alloy in environments likely to be encountered on the inner diameter of the tube (working fluid side) and the outer diameter of the tube (fireside); (5) generate data to be used by heat exchanger designers and the ASME BPV Code; (6) analyze the data for the purpose of setting limits on the design of an MA956 heat exchanger.

3.0 Technical Approach

Of the estimated 152 Qbtu of electricity generated throughout the world in the year 2000, 36% of the fuel consumed for this purpose will be coal.[(1)] Furthermore, this percentage is projected to remain constant through the year 2020, when global electricity demand is expected to be 230 Qbtu, thereby ensuring that coal will continue as the largest contributor to the world's electricity production.[(1)] Although the burning of coal is one of the most

economical methods for producing electrical power, significant amounts of air pollutants such as sulfur dioxide, nitrogen oxides, and the greenhouse gas carbon dioxide, are generated and released into the atmosphere. Therefore, in order to protect the environment and produce a plentiful supply of clean low cost energy, the development of new "clean energy" technologies is imperative.

The Department of Energy (DOE), National Energy Technology Center (NETL), has initiated a strategic plan for the development of advanced technologies needed to design and build fossil fuel plants with very high efficiency and environmental performance. These plants, referred to as "Vision 21" by DOE, will produce electricity, chemicals, fuels, or a combination of these products, and possibly secondary products such as steam/heat for industrial use. In addition, this program will achieve radical improvements in the performance of existing power technologies and seek to virtually eliminate the environmental concerns associated with the use of fossil fuels.

Interest in increasing the efficiency of coal-fired power plants has led to the examination of alternatives to the steam boiler-Rankine cycle systems, for which increases in efficiency have been limited by both the slow progress in its capability to handle steam at temperatures above 565°C (1050°F), and the unavailability of easily-accessible sources of naturally-occurring low-temperature cooling water. Indirect-firing of gas turbines in open or closed cycles is one approach to linking the higher efficiencies possible via the Brayton cycle while still using coal as the fuel. An experimental program in the 1980's [2] demonstrated a coal-fired, low-emissions heat exchanger (fluidized-bed combustor) capable of heating air to 843°C (1550°F) in a metallic heat exchanger, and to 954°C (1750°F) or 1232°C (2250°F) with an additional ceramic heat exchanger. Current programs using indirectly-fired gas turbine cycles are aimed at high cycle efficiencies, of about 47 percent based on the higher heating value (HHV) of the fuel, and involve open cycle systems in which air is heated to 760°C (1400°F) in a metallic heat exchanger, followed by further heating to 982°C (1800°F) in a natural gas-fired ceramic heat exchanger. [3-5] A variant of this approach is where part of the coal is pyrolyzed to produce fuel gas used to fire the ceramic heat exchanger or turbine with air entering the turbine heated to 1288°C (2350°F). A further program envisions using a coal-fired ceramic heat exchanger for the purpose of heating air to 1200°C (2192°F). [6]

Successful implementation of indirectly-fired cycle technologies will require the development of a durable coal-fired *heat exchanger* capable of heating the working fluid to very high temperatures, in addition to adapting a gas turbine for this particular duty. In practice, the form of the heat exchanger surfaces may be considerably different from those in a steam boiler, and there will be other differences such as the fact that the lower temperature portion of the conventional heat exchanger will be significantly smaller, since there is no requirement to provide any latent heat of vaporization. Nevertheless, the fireside corrosion problems will be similar to those in current coal-fired boilers, with some fuels being less aggressive than others, but with much higher tube metal temperatures. On the working fluid side, the heat exchanger wastage mechanism will be the same as gas turbine materials problems, or less severe, than in a conventionally-fired turbine using a clean fuel.

Prime candidate materials for a high temperature heat exchanger are oxide dispersion strengthened (ODS) alloys; however, there are some gaps in the data required to commit to the use of these alloys in a full-size plant. The high temperatures possible with ODS alloys would allow the size of any following ceramic heat exchanger to be reduced, with the possibility that more appropriate or innovative designs could be better tailored to accommodate the needs of ceramics, especially the difficult ceramic-to-metal joints.

The present proposal study will:

- Develop an innovative ODS heat exchanger tube capable of operating at very high temperatures (T_{metal} > 1093°C (2000°F)).
- Develop at least one new method for properly and adequately welding ODS tubes.
- Generate the necessary tube property data required for the design of a heat exchanger made from an ODS alloy.

4.0 Experimental Approach

Team members that performed research activities in this project are Edison Welding Institute (EWI), Foster Wheeler Development Corporation (FWDC), Special Metals Corporation (SMC), and the University of California, San Diego (UCSD). Oak Ridge National Laboratory also participated in aspects of the project; those activities were funded by a previously approved Field Work Proposal (FWP FEAAA058) that was part of the original award made to SMC under Contract No. 00NT40970.

The scope of work was divided into proposed eight tasks. The tasks corresponded to the primary activities associated with increasing the circumferential strength, flow forming and joining of MA956 tubing, and assembling property data for the alloy, and determining the implication of the property data on the design of an ODS heat exchanger. The project tasks are outlined below in the following sections and indicated in the Work Breakdown Schedule (WBS) chart (Figure 1).

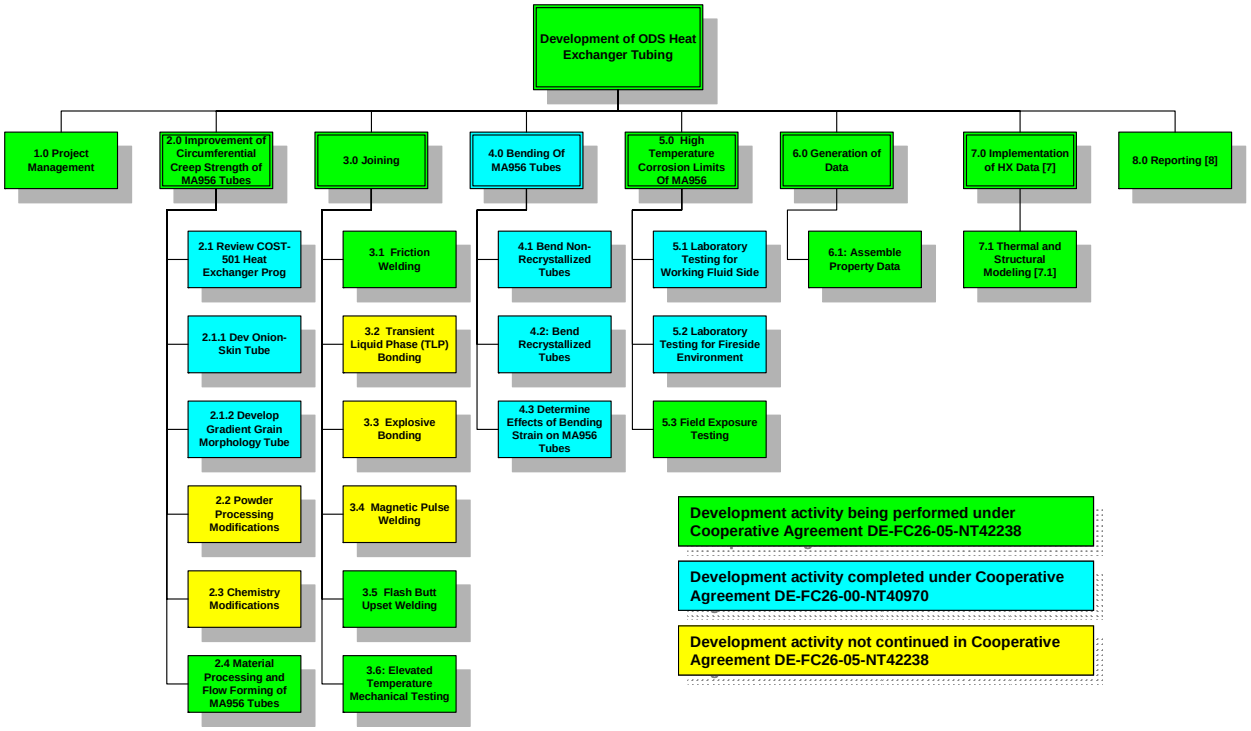

Figure 1. Proposed Project Work Breakdown Schedule

4.1 Task 1. Project Management

An integrated project teaming approach was applied for detailed planning and execution of this project. This approach took advantage of the existing experience base and capital resources of the team, minimizing the investment required for development. The role of each team member is noted in Figure 2.

Note: Portions of the project work plan and associated tasks were funded by DOE-NETL under Cooperative Agreement DE-FC26-00NT40970, initially awarded to Special Metals Corporation (SMC) (dba Huntington Alloys), Huntington, WV, to conduct a study entitled "Development of ODS Heat Exchanger Tubing". Upon declaration of, and emergence from, bankruptcy in late September 2003, Huntington Alloys indicated it would not continue in its capacity as primary sponsor and maintain overall project management oversight for this project, and thus informed DOE that it could not complete the remaining tasks as defined in the original SOW. EWI as one of the primary subcontractors on the 40970 project, assumed responsibility as overall project lead, overseeing completion of the original study. Thus, the project completed the remaining tasks under Cooperative Agreement DE-FC26-05NT42238.

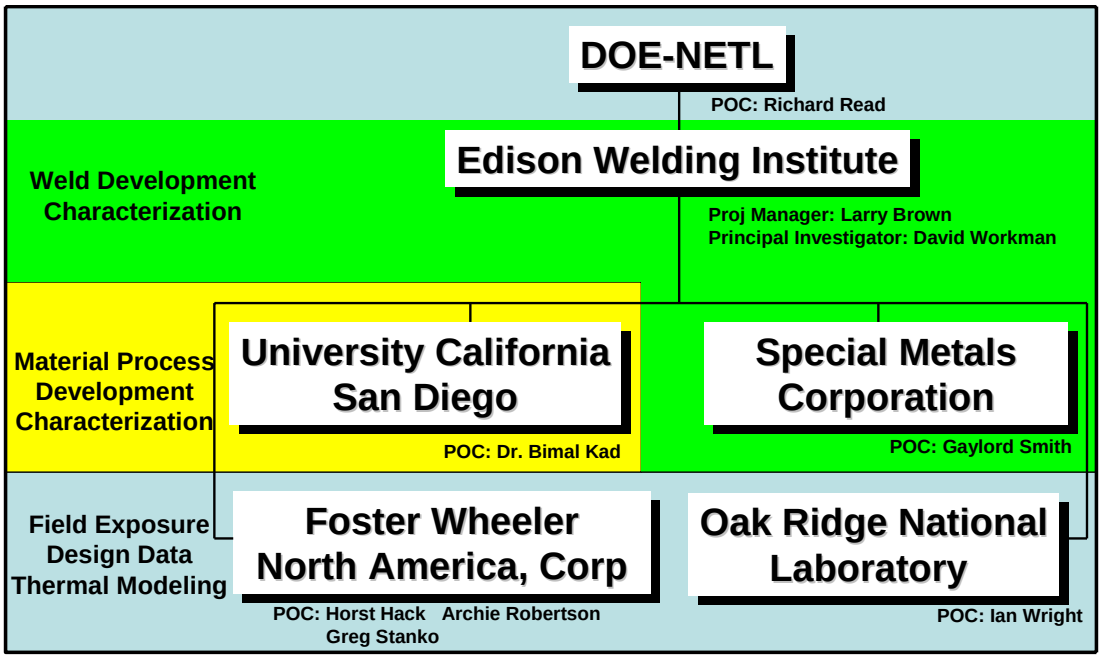

Figure 2. Project Team and Task Activity

4.2 Task 2. Improvement of Circumferential Creep Strength of MA956 Tubes

The effect of extrusion and thermomechanical (TM) processing parameters on "standard" MA956 powders (Fe-20Cr-4.5A1-0.5Ti-0.5Y2O3) was extensively studied. This was to uncover which factors played an important role in producing large "pancake"-shaped grains in the transverse direction of the tubing, and thereby, produced a dramatic increase in the circumferential creep strength. In addition, parameters that produced a Gradient Grain Morphology (GGM) microstructure were investigated. This morphology consisted of an "onion-skin" grain structure in the transverse direction in the center of the tube wall, *bounded* by a fine grain structure at the I.D. and O.D. of the tube.

Material processing and flow forming investigations were done to investigate the effect of ambient temperature MA956 material flow in an orbital/circumferential direction via flow forming techniques. A test matrix was established (Table 1) for the purpose of flow-forming tubes with the aid of an outside vendor. The material formability was evaluated via the extent of wall thickness reduction (i.e., 60-80%) possible. The variable of % reduction/pass evaluated the forming rates effect on the overall process. Material hardening characteristics were evaluated using hardness measurements. This guided the need for intermediate annealing steps to soften the worked tube. All annealing treatments were done at a temperature range of 600-800°C (1112-1472°F) to prevent any incidental recrystallization at this metalworking stage.

Table 1. Flow-Forming Test Matrix for Un-Recrystallized MA956 Tubes

Material Condition	% Reduction/Pass	Wall Thickness Reductions
MA956, un-recrystallized	5%	60%, 70%, 80%
MA956, un-recrystallized	10%	60%, 70%, 80%
MA956, un-recrystallized	20%	60%, 70%, 80%

4.3 Task 3. Joining Development

The overall project objective was to investigate manufacturing processes required to implement ODS alloy tubing in high temperature boiler service. A study was conducted to determine and understand the best method to join an ODS tube to an ODS tube, and the best method to join an ODS tube to a heat resistant alloy (Haynes Alloy 230). For the ODS tube-to-ODS tube joining, tubes that had not undergone the recrystallization treatment and tubes that had undergone the recrystallization treatment were bonded. However, for the ODS tube-to-heat resistant alloy joining, only tubes that had undergone the recrystallization treatment were used, since exposure of the heat resistant alloy to a recrystallization treatment (e.g., T=1315.5°C (2400°F)/1 hour) would cause large grain growth and possible catastrophic oxidation of the heat resistant material.

Feasibility studies were performed to investigate candidate welding processes: friction welding, magnetic pulse welding, and explosive bonding, and flash-butt welding. Each of these processes produced solid-state bonds, avoided hot cracking and other solidification defects at the bondline. In addition, each of these processes restricted its interactions at, or near, the bond surface, minimizing the impact on the engineered properties of the base material.

Weld joints produced in each alloy were evaluated by tensile test and metallographic examination. Initially, this was done to access the process robustness and identify process parameters that produce acceptable weld properties. Once a set of joining conditions for each process was identified, additional mechanical tests were performed (tensile and creep tests). The most viable joining processes were down-selected and the weld test samples were provided for laboratory and field exposure tests.

4.4 Task 4. Bending MA956 Tubes

The effect of various amounts of strain on the recrystallization behavior of tubes that had not undergone a recrystallization treatment, and tubes that had undergone a recrystallization treatment were studied.

4.5 Task 5. High Temperature Corrosion Limits of MA956

The effects of working fluid environments on MA956 were studied. Samples of MA956 were exposed to air and N_2+2%0_2 in order to determine the kinetics and future criteria of the material in these two possible working fluids. Also, the effects of the fireside gas and deposits on the MA956 alloy were studied. Samples of MA956 were exposed to various synthetic flue gas and deposits typical of those expected from the Vision 21 processes. The corrosion wastage mechanisms for the various variables were evaluated and a correlation developed.

Air-cooled test probes were created to investigate the effect of fireside corrosion on MA956 in an actual coal-fired boiler at 1093.3 and 1204.4°C (2000 and 2200°F).

4.6 Task 6. Generation of Data for Designers

Data generated in Tasks 2, 3, 4, and 5 was to be added to that available from the ORNL program, and supplied to designers.

4.7 Task 7. Implication of ODS Properties on Heat Exchanger Design

Modeling of MA956 heat exchanger tubes was to be performed to determine the effects of non-uniform mechanical properties. General-purpose finite element analysis codes, including Abaqus and Algor, were to be used for the analyses. Tubes would have been evaluated in typical heat exchanger arrangements, subjected to thermal and mechanical loads.

This work was to reveal design considerations, accounting for the axial and hoop stresses of MA956 heat exchanger tubes subjected to multi-axial loading. The resulted will be a set of design guidelines to be followed by the heat exchanger designer. These guidelines will allow designers to more readily incorporate the MA956 tubes in various designs, and accelerate commercialization of this technology. Depending upon the outcome of this task, additional future work (i.e., fatigue and creep testing) may be recommended.

5.0 Results and Discussion

5.1 Task 1. Project Management

This final report contains major portions of the project work plan and associated tasks funded by DOE-NETL under Cooperative Agreement DE-FC26-00NT40970, initially awarded to Special Metals Corporation (SMC) *(dba Huntington Alloys)*, Huntington, WV, to conduct a study entitled “Development of ODS Heat Exchanger Tubing”. Upon declaration of, and emergence from, bankruptcy in late September 2003, Huntington Alloys indicated it could not continue in its capacity as the primary sponsor and maintain overall project management oversight for this project. Thus, they informed DOE that they would not complete the remaining tasks as defined in the original statement of work (SOW). The DOE strongly believed that without the completion of the SOW, the study would not provide the critical

information necessary to determine the potential usage of ODS-type materials for high-temperature heat exchangers. Essentially, all tasks that were to be conducted by SMC were completed, but without conducting the remaining tasks, the data generated would have little value. EWI as one of the original primary subcontractors on the 40970 project, assumed responsibility as overall project lead, oversaw completion of the original study, and maintained the tasks to be completed as defined under the original project (40970).

As noted in Figure 2, some of the original proposed project tasks were removed because the work was determined – mutually by the DOE and project team – no longer to be necessary or relevant. The task activities not completed were:

- Subtask 2.2 – Powder Processing Modifications of Current MA956 Powders
- Subtask 2.3 – Modifications to Current MA956 Powders

Also, as a result of the joining activity in 40970, it was decided to investigate two additional processes as subtasks in Task 3 (Joining Development). These were:

- Friction Stir Welding
- Magnetic Pulse Welding

As project activity continued, the project SOW was modified to address Subtask 5.3 "Field Exposure Testing" under Task 5 "High Temperature Corrosion Limits of MA956". It was originally planned to install field corrosion test probes at the TVA Gallitin facility, where all of the equipment, piping, controls, and instrumentation required for probe operation were already in place. Since that site was no longer available, Foster Wheeler located a new site, Duke Energy's Gibson Station. DOE was alerted that a new design and purchase of equipment and instrumentation would be required for probe installation at the Gibson Site. A contract modification was executed to permit the design and purchase of equipment for probe installation at the new site. However, due to the potential for cost overrun of the project, it was mutually agreed upon by the project team and DOE to complete fabrication of the field test probes and remove Task 6, "Generation of Data for Designers", and Task 7, "Implications of ODS Properties on Heat Exchanger Design", from the existing SOW under Agreement DE-FC26-05NT42238. Field testing of the probes and remaining heat exchanger design activity will be performed by Oak Ridge National Laboratory under DOE Contract DE-AC05-00OR22725. The field test probes and supporting equipment were transferred to the Oak Ridge Contract.

5.2 Task 2. Improvement of Circumferential Creep Strength of MA956 Tubes

5.2.1 Subask 2.1-2.3 Extrusion and Thermomechanical (TM) Processing

(Note: Reported from Cooperative Agreement DE-FC26-00-NT40970)

The matrix of tests shown in Table 2 were completed at Special Metals Corp. The execution of this matrix resulted in 540 different combinations of extrusion + thermomechanical + annealing parameters. Table 3 shows the work that was completed with the extrusion samples.

Table 2. Matrix of Extrusion + Cold Work + Recrystallization Parameters

Extrusion Temp °C (°F)	Extrusion Ratio	Amount of Cold Work (%)	Recrystallization Temp °C (°F)	Recrystallization Time (hrs)
1000 (1832)	10:1	0	1000 (1832)	0.5
1075 (1967)	16:1	5	1150 (2102)	1
1150 (2102)	20:1	10	1300 (2372)	6
1200 (2192)		15		
		30		

Table 3. Work Completed on Extruded + Cold Work + Recrystallized Bar Samples

Operation	Number Required	Number Complete	% Complete
Extrusion	180	180	100
Decanning	540	540	100
Cold Work	540	540	100
Annealing	540	540	100
Samples Prepared	540	540	100
Microstructure Analysis	540	540	100

Note: Transverse samples were taken from each condition for evaluation.

Microstructural Analysis: Microstructural analysis of the rods that have been extruded + cold worked + annealed was completed and a variation in the grain structure was observed. Regarding the effect of recrystallization temperature, samples annealed at 1000°C (1832°F) did not exhibit any recrystallization, independent of the amount of cold work imposed on the sample. However, samples annealed at 1150°C (2102°F) did show the onset of primary recrystallization, the amount being dependent on the amount cold work. When annealed at 1300°C (2372°F), all the samples exhibited primary and secondary recrystallization, with the final recrystallized grain morphology being a function of the cold work for a given sample. Figure 3 shows the variation in microstructure morphology observed as a function of cold work for samples annealed 1300°C (2372°F) for six hours. Thus, it would appear that while up to 30% CW can initiate recrystallization – it does not guarantee a large processed grain size. It is also important to note that shear bands occur for samples subjected to relatively large amounts of cold work, thereby creating transverse grain boundaries which may restrict secondary grain growth Figure 3(c).

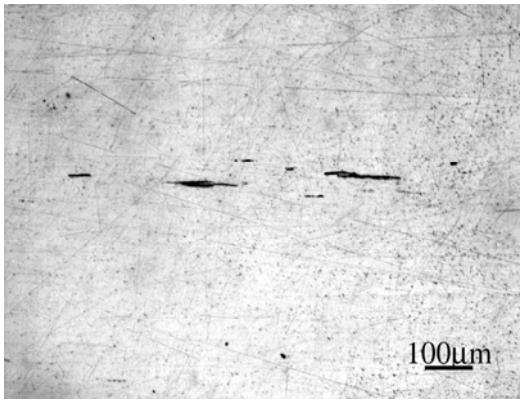

(a)

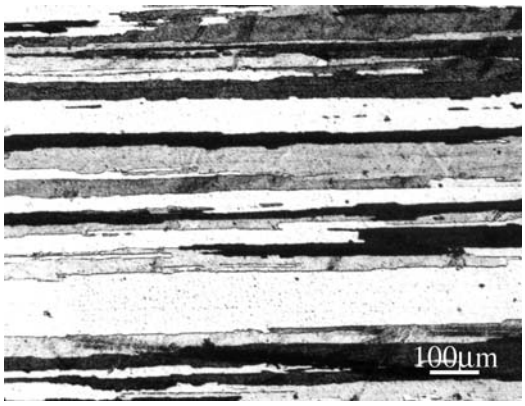

(b)

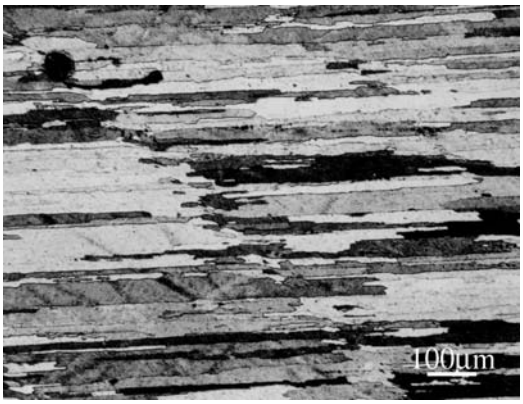

(c)

Figure 3. Variation in Microstructure for MA956 Rods Extruded at 1000°C (1832°F) using 10:1 Extrusion Ratio followed by (a) 0% CW, (b) 10% CW, and (c) 30% CW, then Annealed at 1300°C (2372°F) for 6 Hours

Tube samples flow formed greater than 85% at Dynamic Machine Works in Bellerica, MA, and annealed at 1300°C (2372°F)/one hour recrystallized to an oinion skin texture in the transverse direction. This work was funded outside of this project.

Transmission electron microscopy (TEM) studies have been the most comprehensive for samples extruded at 1075°C (1967°F) using a 20:1 extrusion ratio and annealed at 1150 or 1300°C (2102 or 2372°F). The microstructures of these samples appear to be bimodal with regions that are fully recrystallized as well as areas where no recrystallization has occurred. Also noted was that by increasing the amount of cold work resulted in an increase of the volume fraction of recrystallized material, as shown in Figure 4.

Microstructures that experienced creep at ORNL also were examined with TEM. Figure 5 is a TEM micrograph of the microstructure of a sample exposed to a high stress for a short time (68.9 MPa (10 ksi)/< ½ hour) at 900°C (1652°F). As seen in this figure, the microstructure had the ability to develop and sustain a high density of dislocation network with the dislocations suitably pinned by dispersoids as shown in Figure 6, whereas, Figure 7 shows grain boundary migration with segments pinned by large dispersoids. This gave initial evidence that the boundaries may be mobile at 900°C (1652°F) under high stress (68.9 MPa (10 ksi)).

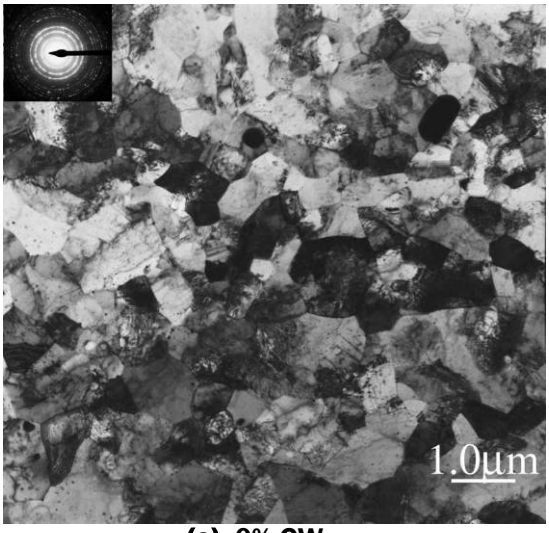

(a) 0% CW

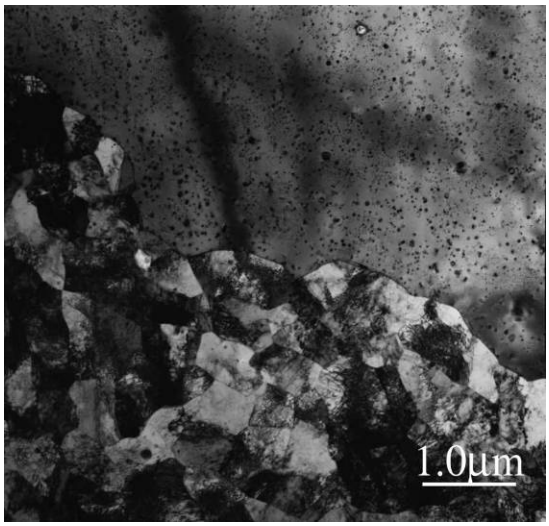

(b) 10% CW

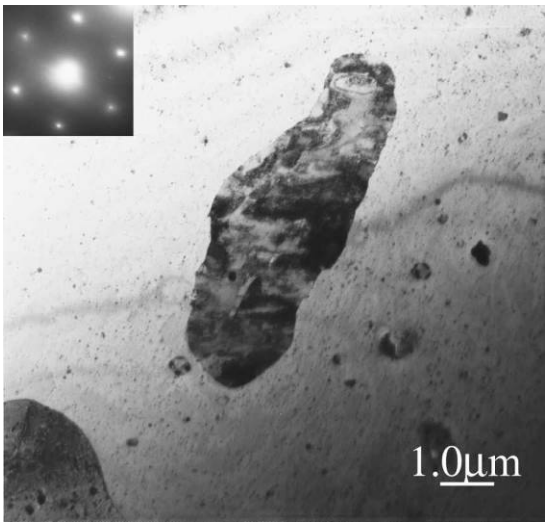

(c) 20% CW

Figure 4. Effect of Cold Work on Recrystallization for Samples Extruded at 1075°C (1967°F) using 20:1 Extrusion Ratio and Annealed at 1150°C (2102 °F) for 6 Hours

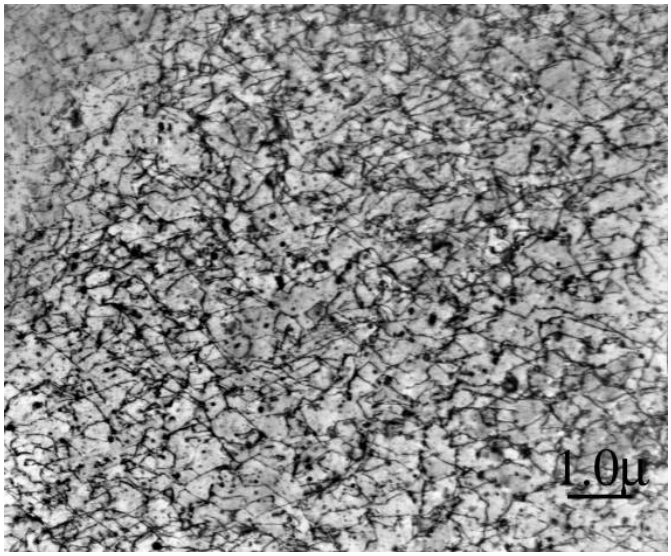

Figure 5. TEM Micrograph of Transverse Oriented Creep Sample Subjected to High Stress for Short Time (68.9 MPa (10 ksi))/< ½ hour) at 900°C (1652°F)

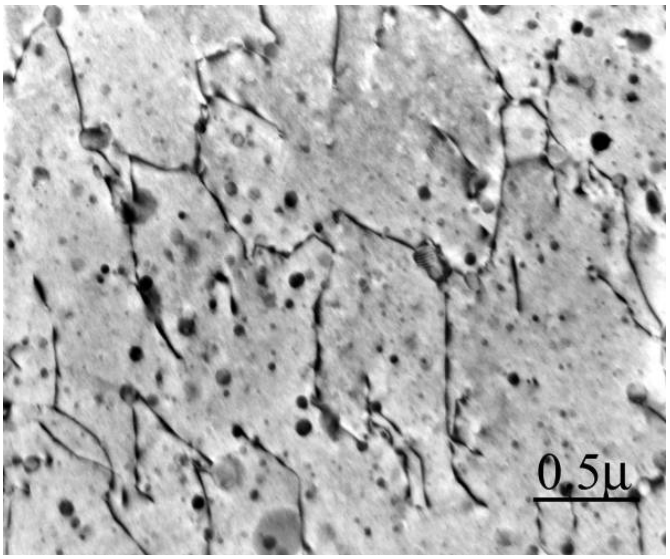

Figure 6. TEM Micrograph of Transverse Oriented Creep Sample Subjected to High Stress for Short Time (68.9 MPa (10 ksi)/ < ½ hour) at 900°C (1652°F) showing Stable Dislocation Pinning by Dispersoid Particles

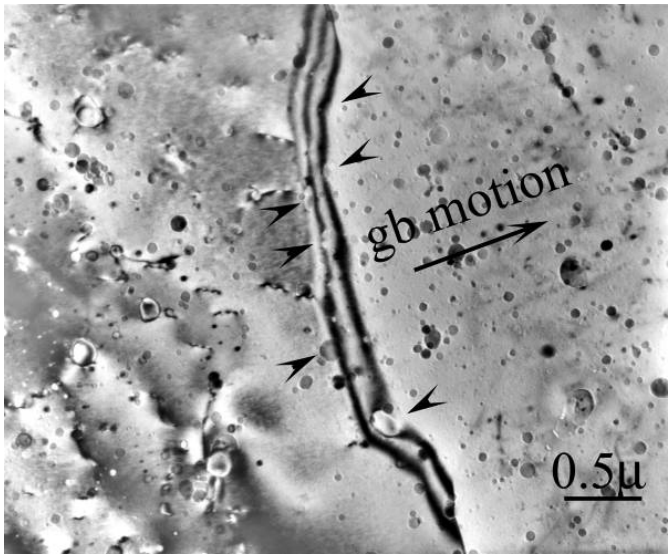

Figure 7. TEM Micrograph of Transverse Oriented Creep Sample Subjected to High Stress for Short Time (68.9 MPa (10 ksi)/< ½ hour) at 900°C (1652°F) showing Grain Boundary Migration under Applied Stress and Drag Exerted by Coarse Particles (as marked) in Microstructure

Creep Testing: Results of the creep testing of specimens cut in the axial direction from the walls of a nominal 1-in. diameter MA956 tube are shown in Table 4 with the data plotted in Figure 8. The specimens were loaded at the initial value indicated in the table, and the load was increased by 6.89 MPa (1 ksi) every 100 hours until failure. The 'life' values show the total exposure time and, in brackets, the time spent in the last load increment. It is important to note that the reason for performing this type of creep testing was that the excellent strength of this alloy at elevated temperatures resulted in a relatively "flat" stress rupture curve. Thus, extremely long times were required to cause rupture if the applied stress was below a "threshold" value where essentially no creep occured. In order to determine the approximate value of this threshold stress for a given alloy at a particular temperature, creep tests were conducted wherein the sample was incrementally loaded at 100-hour intervals.

Table 4. Results of Stress Threshold Testing for the MA956 Alloy

Temp. (°C)	Temp. (°F)	Load (MPa)	Load (ksi)	Life	El. (%)	LM Parameter
900	1652	48.3-96.5	7-14	860 (44)	0	45.7
950	1742	34.5-96.5	5-14	1224 (51)	—	47.8
1000	1832	20.7-55.2	3-8	590 (59.2)	2.4	49.4

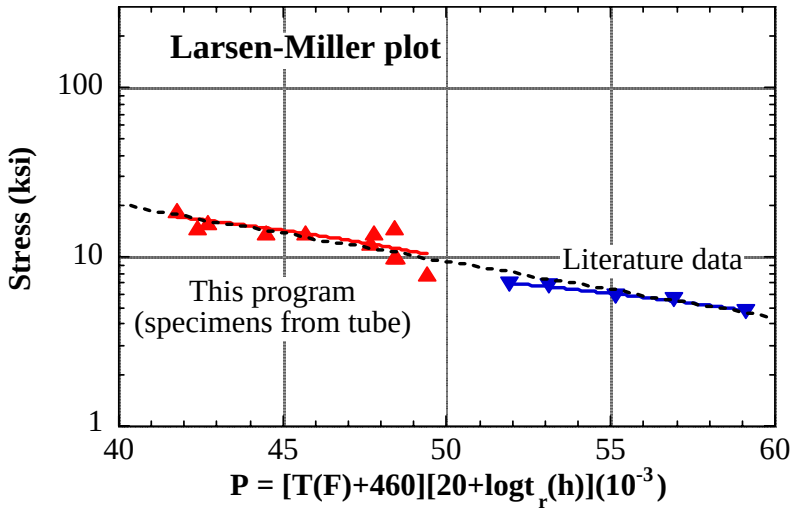

Figure 8. Larsen-Miller Plot showing Good Agreement Between the Stress Rupture Data Obtained during Project and Stress Rupture Data Obtained from Literature

In an effort to test MA956 tubing in the transverse direction, pieces of MA956 tubing were cut in half in the longitudinal direction and the half pieces hot worked into flat pieces of plate (Figure 9).

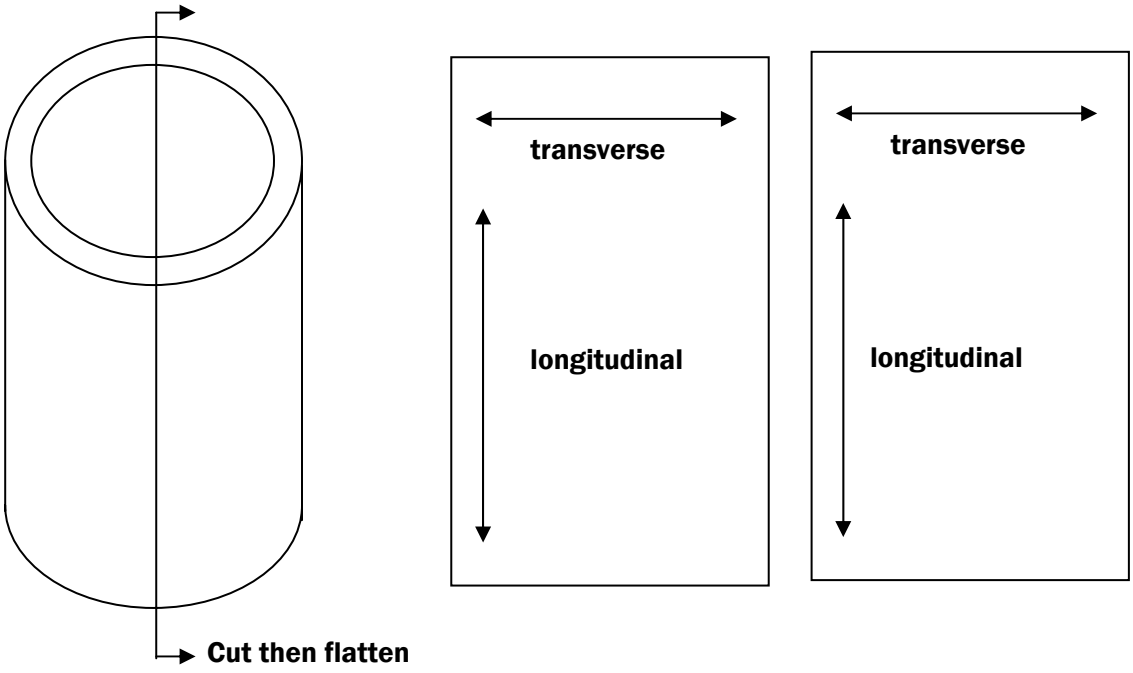

Figure 9. Schematic Drawing showing How Plate was Produced from Tube Allowing Creep samples to be Taken in Transverse Direction

The current compilation of data for the creep threshold curves for specimens cut from two tubes of different diameter, and from the flattened tube mentioned above are shown in Figure 10. The transverse direction creep threshold stresses determined for specimens cut from a flattened 60 mm OD × 5 mm (2.36 in. × 0.197 in.) wall tube are significantly lower than those determined for the longitudinal direction for specimens cut from a non-flattened tube. While this was expected – it was the basis for this project – the comparison is not straightforward since the grain sizes of the two heats of alloy are significantly different.

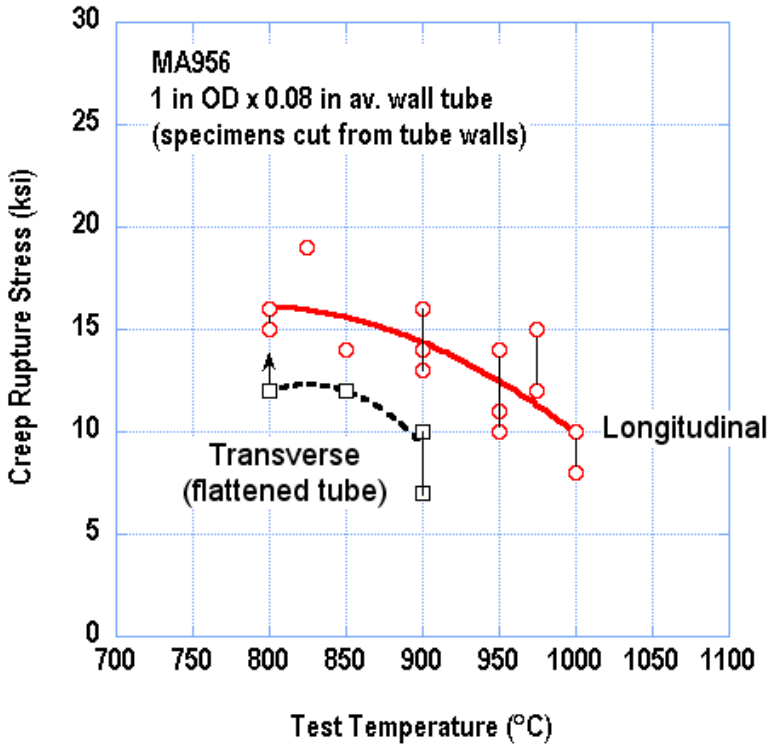

Figure 10. Longitudinal and Transverse Creep Threshold Curves for Specimens Cut from MA956 Tubes
Note: The transverse samples were taken from a flattened 6 cm OD × 5 mm (2.36 in. × 0.197 in.) wall tube.

5.2.2 Subask 2.4 Material Processing and Flow Forming of MA956 Tubes

The experimental work reported here is described in the context of the following task structure.

Task 1. Ambient Temperature Flow Forming and Flow Spinning

- Cross-roll flow forming of un-recrystallized MA956 tubes

Materials for this program were available as un-recrystallized tubes of 63.5 mm (2.5 in.) O.D. and 6.35(0.25 in.) wall thickness. Subsequent processing was performed by ambient temperature flow forming to reduce wall thickness, and tube slitting, flattening at 900°C (1652°F) and cross rolling at 900°C (1652°F). It was noted that deformations tend to be 60-80% in the former and 10-30% in the latter processing method.

Task 2. Recrystallization and Microstructure Evaluation

- Recrystallization annealing: static and gradient
- Microstructure characterization and evaluation (Optical and TEM)

Processed tubes were cut into segments for evaluating the recrystallization kinetics and the optimum conditions for developing a large processed grain structure. The flow formed tubes were slit in half by spark machining, and subsequently flattened at room temperature, and 900°C via rolling. The flow formed tubes upon slitting exhibited distinct shape distortion (shear angleϕ = 5-10°), (Figure 11), indicative of the residual elastic strain energy in the tube after flow forming at room temperature. As a corollary to this distortion – room temperature flattened tube segments are never completely flat, i.e., they retain some curvature. Tubes flattened at 900°C (1652°F) completely eliminated this problem. A low temperature recrystallization treatment at 1200°C (2192°F) failed to initiate any significant change in grain size. Further heat treatments were then performed at the recrystallization treatments prescribed by the Special Metals Corp. The flattened pieces were recrystallized in air at 1375°C (2507°F) for one hour.

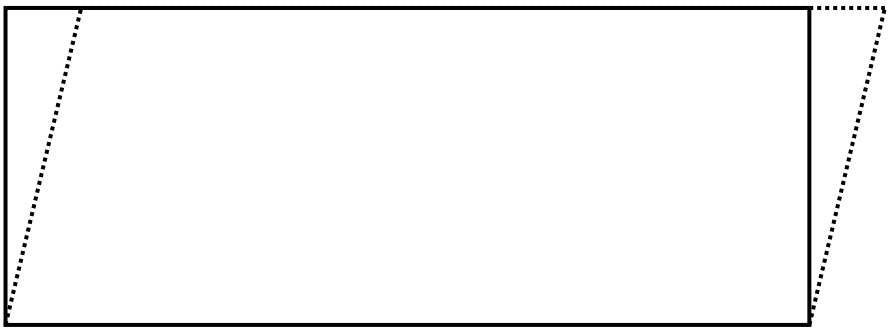

Figure 11. Shear Distortion of Flow Formed Tube Slit in Axial Direction

Task 3. Creep Performance Evaluation: Stress Rupture and Threshold Tests

- Longitudinal creep and stress-rupture response
- Transverse creep and stress-rupture response
- Processing dependent Creep anisotropy evaluation

This task was performed concurrently with Task 1 and Task 2 and evaluated the ultimate success of each task for its improved high temperature stress-rupture and creep performance. This applied to both the forming in Task 1 as well as the recrystallization performed in Task 2. In recognizing the through-thickness gradient nature of the flow forming process, creep test specimens, conforming to the ASTM E139-00 test standard, were spark machined using the entire section thickness. Transverse creep tests were done on both the cross-rolled pieces and flow formed tubes. Table 5 shows the resulting creep behavior for each processing path as compared to the base material performance of Larsen-Miller Parameter (L-M) of about 45. For, ease of future reference, the results were separated into three subsets: 1) cross-rolled (Test #2-4); 2) flow-formed and flattened at RT (Test #5-9); and 3) flow-formed and flattened at 900°C (1652°F) (Test #10-13). Note that the base materials performance was derived over a battery of tests and condensed into a single number indicating the best achievable performance.

Table 5. Transverse Creep Testing of MA956 Tube Materials Processed via Cross Rolling (CR) and Flow Forming (FF)

Test #	MA956 Processing and HT *(Note: 900 and 1375°C = 1652 and 2507°F respectively)*	Temp °C (F°)	Stress MPa (ksi)	Life (hrs)	L-M Para	Strain Rate/Day
1	MA956, As-received, 1375°C = 1hr	900 (1652)	13.8 (2)		45.00	
2	CR-20% @900°C, 1375°C = 1hr	900 (1652)	13.8 (2)	691	48.24	
3	CR-20% @900°C, 1375°C = 1hr	900 (1652)	13.8 (2)	1408	48.89	
4	CR-20% @900°C, 1375°C = 1hr	800 (1472)	13.8 (2)	3407*	45.46*	
5	Flowform, flatten@RT, HT:1375°C,1hr	900 (1652)	13.8 (2)	1447	48.91	5.0e-4
6	Flowform, flatten@RT, HT:1375°C,1hr	1000 (1832)	13.8 (2)	19	48.77	1.14e-2
7	Flowform, flatten@RT, HT:1375°C,1hr	950 (1742)	13.8 (2)	118	48.60	2.6e-2
8	Flowform, flatten@RT, HT:1375°C,1hr	950 (1742)	13.8 (2)	428	49.83	4.0e-4
9	Flowform, flatten@RT, HT:1375°C,1hr	900 (1652)	13.8 (2)	1591	49.00	4-0e-4
10	Flowform, flatten@900°C, 1375°C = 1hr	1000 (1832)	13.8 (2)	452	51.93	7.0e-4
11	Flowform, flatten@900°C, 1375°C = 1hr	950 (1742)	13.8 (2)	7329	52.55	7.0e-5
12	Flowform, flatten@900°C, 1375°C = 1hr	975 (1787)	13.8 (2)	9900*****	53.92*****	1.0e-5
13	Flowform, flatten@900°C, 1375°C = 1hr	1000 (1832)	13.8 (2)	6400*	54.56*****	1.0e-5

***** *Test suspended after fully stabilized.*

Creep test results showed sustained improvement in transverse creep response both in cross-rolled and flow formed materials over the base material. Thus, the initial premise of this research effort of creep enhancement via mechanical forming has merit. Both post-processed materials (CR and FF) exhibited stable performance at 800°C (1472°F) unlike base material. Results indicated that the measured response was sensitive to the specific heat-treatment employed to extract the flat tensile specimens. The notion that creep performance could be altered by post flow-forming recrystallization HT required that this step be repeated for the duration of the project.

Creep data for Test #10-13 showed that performance was superior to all previously reported values and highlighted the importance of severe plastic deformation, as imposed via ambient temperature flow forming, on as-processed MA956 tubes. In repeated tests it was observed that the Larsen-Miller Parameter was at about 52 and above. Test #12 and 13 indicated that

creep performance continued to improve incrementally in repeated tests. A threshold of LMP=54.56 was achieved for 975-1000°C (1787-1832°F) creep tests, i.e., better than ever recorded previously. Figure 12 shows one such creep exposure plot for Test #12 (see Table 5) operating at 975°C (1787°F) in air at a constant applied stress of 13.8 MPa (2 ksi). The plot suggests the material is in the steady state regime with an aggregate creep strain rate of 1.0e-5/day over the last 200 days of exposure.

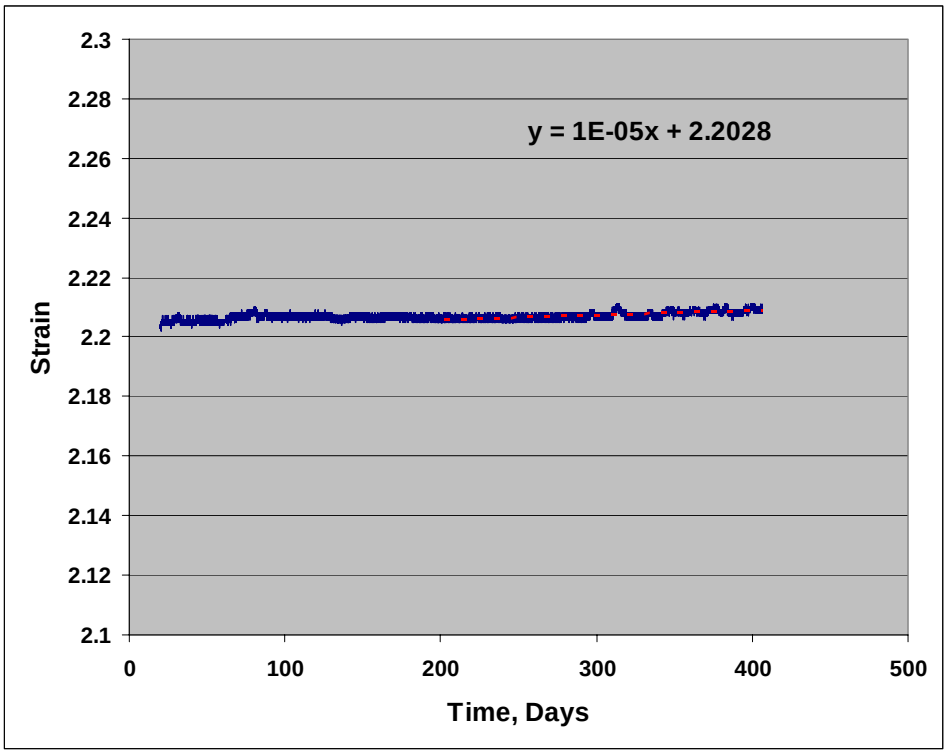

Figure 12. Creep Extension Data for Test#12 Exposed at 975°C (1787°F) in Air for 9900 hours at Constant 13.8 MPa (2 ksi) Stress

5.3 Task 3. Joining Development

The overall project goal was to investigate manufacturing processes required to implement ODS alloy tubing in high temperature boiler service. As such, joining of ODS materials became key to wide usage of the material. At least one process was to be identified as a fabrication technology for joining MA956. The joining development activity in this project investigated 6 candidate welding process to develop and demonstrate process feasibility. The candidate processes are:

- Inertia Friction Welding
- Friction Stir Welding
- Transient Liquid Phase (TLP) Bonding
- Explosive Welding
- Magnetic Pulse Welding
- Flash Butt Welding

Each of these processes produces solid state bonds that have been shown in other materials to avoiding hot cracking and other solidification defects at the bondline. In addition, each of these processes restricts its interactions at or near the bond surface, minimizing the impact on the engineered properties of the base material.

Inertia Friction Welding: Friction welding operates by spinning one of two materials, then once at speed, the two materials are forced together turning kinetic energy into heat. As the materials heat, one or both of the materials begin to extrude material out away from the bondline. This extruding of material is a result of the materials being heated enough so that plastic deformation can occur. Once the rotation has been stopped, the materials, in some cases, are further consolidated with a higher force than used while the parts were rotating (Figure 13). Friction welding is a common process used in automotive, aerospace, and other heavy and light manufacturing applications.

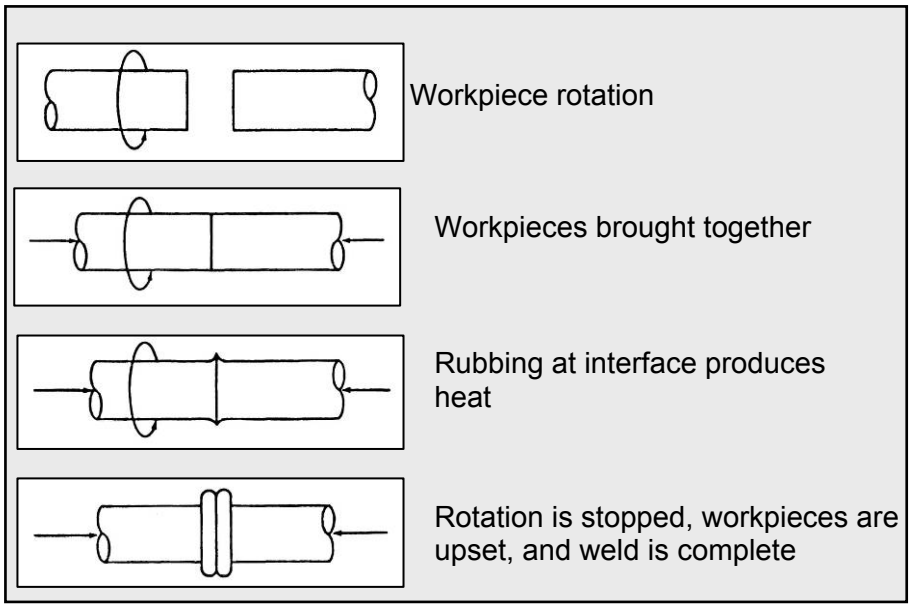

Figure 13. Depiction of Inertia Friction Welding Process

Friction Stir Welding: Friction stir welding (FSW) utilizes a non-consumable tool to create local friction heating to produce a continuous solid-state weld. T he process allows a variety of joint configurations to be created using single pass, full penetration approach without the use of filler metals (including butt, lap, corner, and T-joints). The solid-state, low distortion welds produced are achieved with relatively low cost using simple and energy-efficient mechanical equipment.

The friction stir welding process involves plasticizing the material at the joint interface using a rotating tool. The tool is comprised of two primary components: a pin and shoulder. The pin first contacts the material with a downward force and rotation. This produces frictional heating, which allows the material to plastically flow as it heats up and loses strength as a function of temperature. The pin is inserted until contact is made between the shoulder of the tool and the top surface of the material. The shoulder acts to produce additional frictional heat and provides constraint against the flow of plasticized material while applying a forging force to the top surface of the weld. The tool then continues to rotate while traveling along the joint to complete

the weld. When the desired length has been achieved, the friction stir tool is removed. A schematic of this weld process is shown in Figure 14.

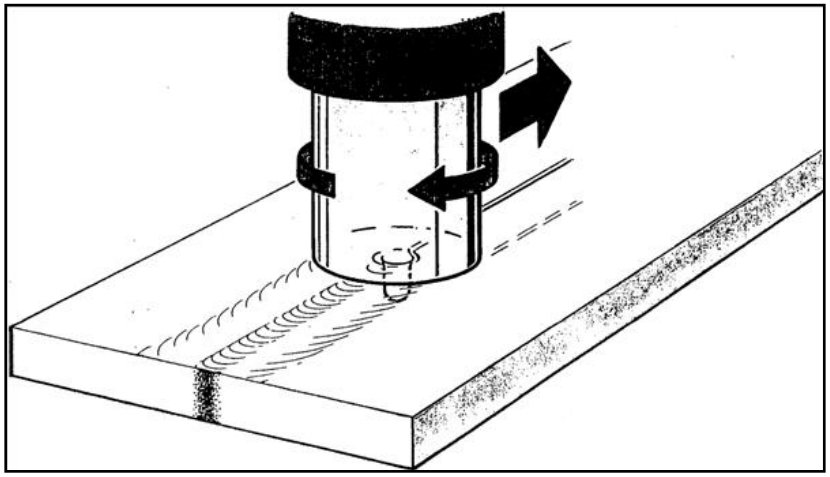

Figure 14. Friction Stir Welding Process Schematic

Explosive Welding: Explosive welding differs from friction welding in that it uses energy from the denotation of an explosive place over the two materials to be welded. This denotation causes one of the materials to accelerate into the other at very high speeds, which causes a metallic bond to form due to plastic flow of the materials. Bonding occurs at ambient temperatures, as the detonation process induces little if any heat into the materials. A representation of the process is shown in Figure 15.

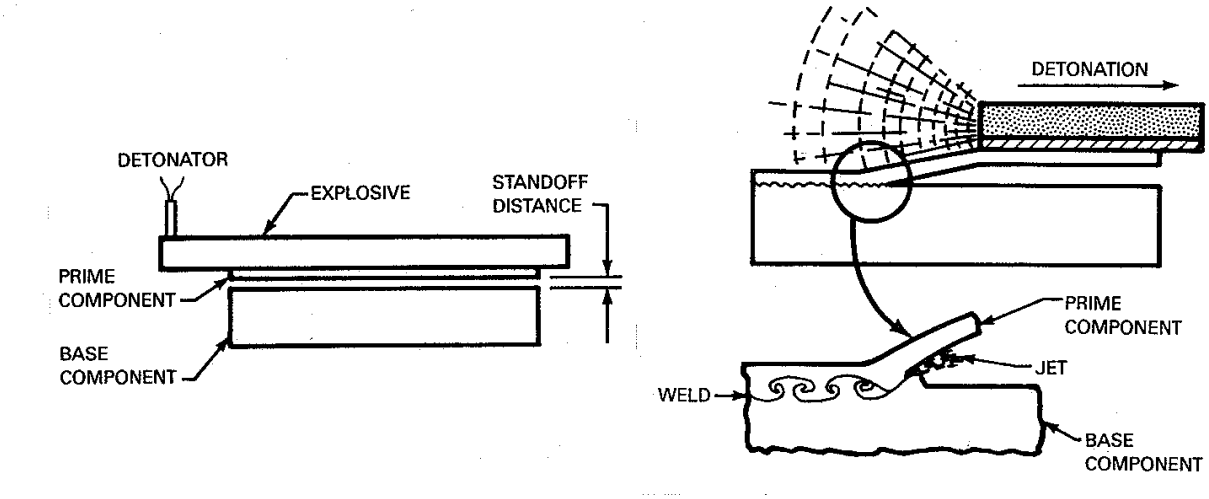

Figure 15. Depiction of Explosion Welding Process

Magnetic Pulse Welding: Magnetic pulse welding (MPW) is a high-speed joining process that uses electromagnetic force to accelerate and impact one part onto another, resulting in a solid-state weld. Magnetic pulse welding is typically used for lap joints between tubular components, or between a tube and a solid section. During magnetic pulse welding, the components are placed inside a coil in a lapped configuration. An electrical current is then sent through the coil,

generating an intense magnetic field and creating high eddy currents in the outer tube. These eddy currents create intense opposing magnetic fields, forcing the outer component onto the inner component. The resulting high velocity impact (combined with appropriate contact angles) causes formation of a pseudo solid-state bond. Thermal effects with this process are very highly localized, resulting in little macroscopic heating of the workpieces. The process can also form joints by expanding the inner (tubular) component against an outer component. MPW is a process typically used for tubular components in the automotive, aerospace, and fluid products industries.

As depicted in Figure 16 when high voltage is applied to the coil, a large magnetic force (pressure) is induced into one of the two materials to be welded, causing plastic flow of the two materials. This plastic flow results in a metallic bond very similar in appearance to explosive welding.

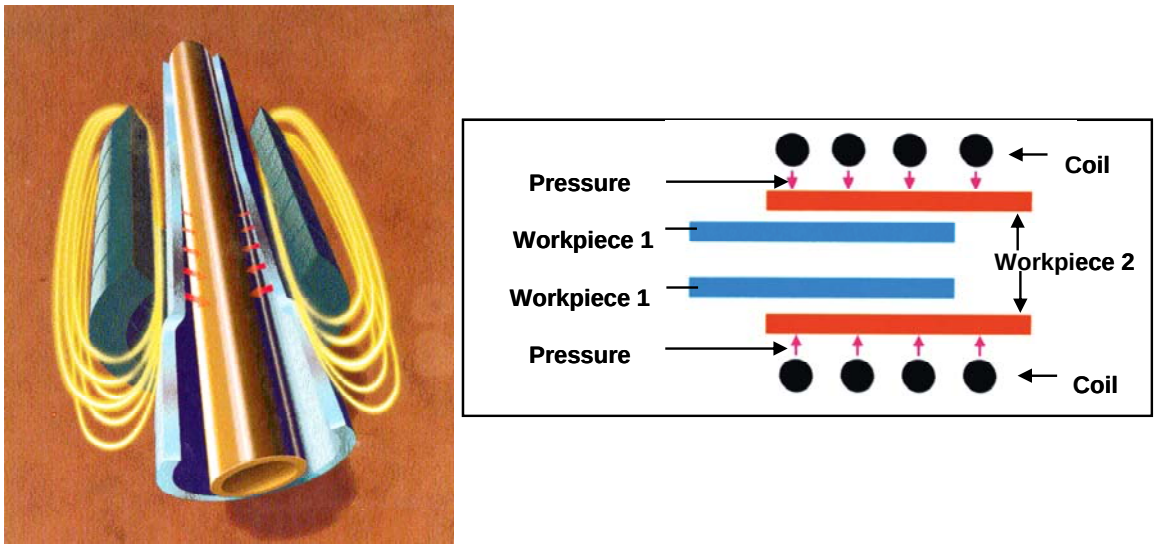

Figure 16. Magnetic Pulse Welding Process Schematic

Transient Liquid Phase Bonding: In TLP bonding an interlayer containing melting point depressants is placed between the bonding surfaces and held at a prescribed temperature and load. At the bonding temperature, which is less than the melting temperature of the parent alloy, the interlayer melts and through diffusion kinetics changes in composition of the liquid interlayer (due to the loss of melting point depressants from the joint region) results in the formation of a joint by isothermal solidification.

Flash Butt Welding: Flash butt welding is a resistance welding process which produces coalescence of materials by a flashing action and the application of pressure after heating is completed. The flashing action, created by high current densities at small contact points between faying surfaces, forcibly expels material from the joint as the surfaces are being moved slowly together. The weld is completed by rapidly upsetting the materials to create a solid state bond. Figure 17 show basic steps for flash butt welding. This process is capable of producing weld joints in metallurgically challenging alloys which MA956 is considered from a weldability standpoint. The process is capable of joining many shapes and section geometries.

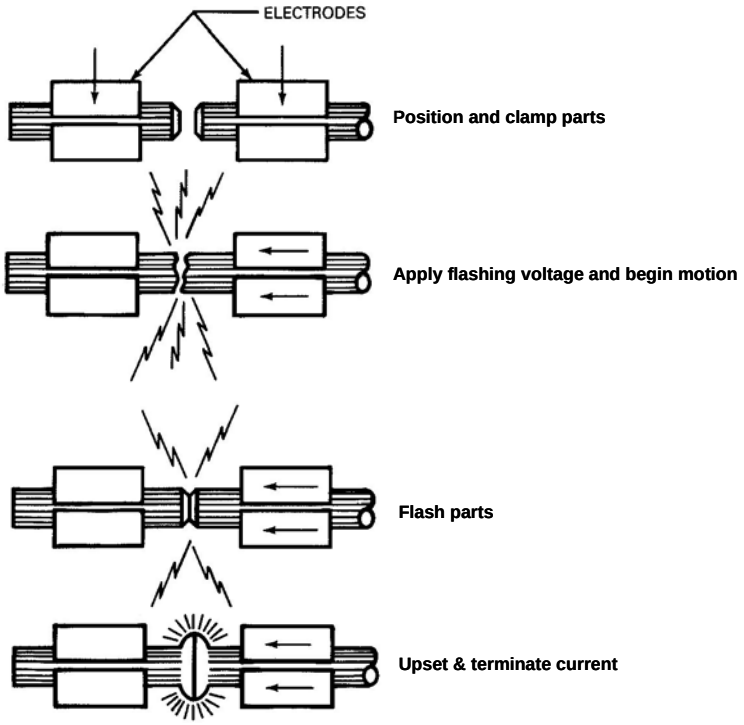

Figure 17. Basic Steps for Flash Butt Welding

The joining development efforts in this project investigated producing welds in material combinations: ODS to ODS, ODS recrystallized to ODS recrystallized, and ODS to a heat resistance alloy. Weld joints were produced in each alloy combination followed by screening tests using either tensile, bend testing, or metallographic examination. This was done initially to access the process robustness and identify process parameters, which produce acceptable weld properties.

From the joining development activity two processes were identified as being viable for manufacturing of ODS heat exchanger tubing. The processes were Inertia Friction welding and Flash Butt Welding. The results of all weld investigation activity are discussed below.

5.3.1 Subask 3.1 – Inertia Friction Welding

In order to produce the welds in this material, Inertia Friction Welding (IFW) was used as it is often the preferred process for Superalloys in turbine engine manufacturing. In order to begin welding trials, welding parameters typical of nickel base super alloy were used. Process parameters such as surface velocity, W/K2 inertia, weld force, upset force, and upset velocity were examined. Weld quality was assessed by metallographic examination, SEM analysis, and tensile testing.

A series of welds were made on the first lot of tubing supplied to the project and metallographic analysis and tensile tests were conducted on samples welded with two different sets of welding parameters (noted as #I2 and #I3). For tensile testing, a strip sample was taken from various points around the diameter of the tube (noted as A, B, and C). Mechanical property data for each of the welds tested are listed in Table 6. These results appear promising compared to the parent alloy properties shown in the table, however the variation in mechanical properties around the circumference of the joint was cause for concern.

Table 6. Mechanical Property Data for Two Inertia Welds – Room Temperature

Sample Identification	Ultimate Tensile Strength MPa (ksi)	Yield Strength MPa (ksi)	Elongation (%)
I2-A	682.6 (99.0)	591.6 (85.8)	4.4
I2-B	505.4 (73.3)	N/A	0.2
I2-C	669.5 (97.1)	643.3 (93.3)	2.2
I3-A	551.6 (80.0)	N/A	3.4
I3-B	685.3 (99.4)	552.3 (80.1)	7.7
I3-C	461.9 (67.0)	N/A	2.0
MA956*	644.7 (93.5)	552.9 (80.2)	10

***** *Typical properties of parent material*

Friction welds between MA956 tubing and 601 tubing were also conducted with the mechanical properties of such a weld shown in Table 7 below. As shown in this table, the joint strength approached that of the 601 alloy, and thus, showed promise that friction welding could serve as a suitable technique for joining MA956 to a traditional wrought heat resistant alloy.

Table 7. Mechanical Property Data for the MA956 Tubing Joined to 601 Tubing Using Friction Welding – Room Temperature

Sample Identification	Ultimate Tensile Strength MPa (ksi)	Yield Strength MPa (ksi)	Elongation (%)
MA956/601-1	273.0 (39.6)	259.2 (37.6)	< 1
MA956/601-2	182.0 (26.4)	136.5 (19.8)	< 1
MA956/601-3	297.9 (43.2)	292.3 (42.4)	< 1
MA956/601-4	279.2 (40.5)	277.9 (40.3)	< 1
601*	741.2 (107.5)	290.3 (42.1)	47

***** *Typical properties of 601 hot finished bar solution annealed at 1093°C (2000°F).*

In an effort to determine how robust a processing window was required to make an acceptable joint a small Design of Experiments (DOE) task was initiated to evaluate the effect of different process parameters on the elevated temperature performance of inertia friction welded (IFW) joints in MA956 alloy. Variables under investigation in the DOE study included initial surface velocity, or speed, and the welding force in the IFW process. Aluminum welds were made for the MA956/MA956 non-recrystallized couple. The process parameters of the current testing as well as weld features are indicated in Table 8 and photomicrographs of each sample are shown in Figure 18 through Figure 21 below.

Table 8. Process Parameters for Design of Experiments being Conducted for Inertia Friction Welding of MA956 Alloy

Sample No.	Speed (RPM)	Force MPa (ksi)	Mechanically Mixed Zone width mm (inch)	Plasticized Zone width mm (inch)	HAZ Width thermal mm (inch)	Burnoff mm (inch)
5	425	172.4 (25)	0.0425 (0.0017)	0.50 (0.0197)	1.10 (0.043)	1.77 (0.070)
6	625	172.4 (25)	0.0825 (0.0032)	0.54 (0.0213)	1.45 (0.0571)	6.35 (0.250)
7	625	241.3 (35)	0.1125 (0.0044)	0.48 (0.0189)	1.80 (0.071)	8.63 (0.340)
8	425	241.3 (35)	0.0150 (0.0006)	0.40 (0.0157)	1.10 (0.043)	2.80 (0.110)

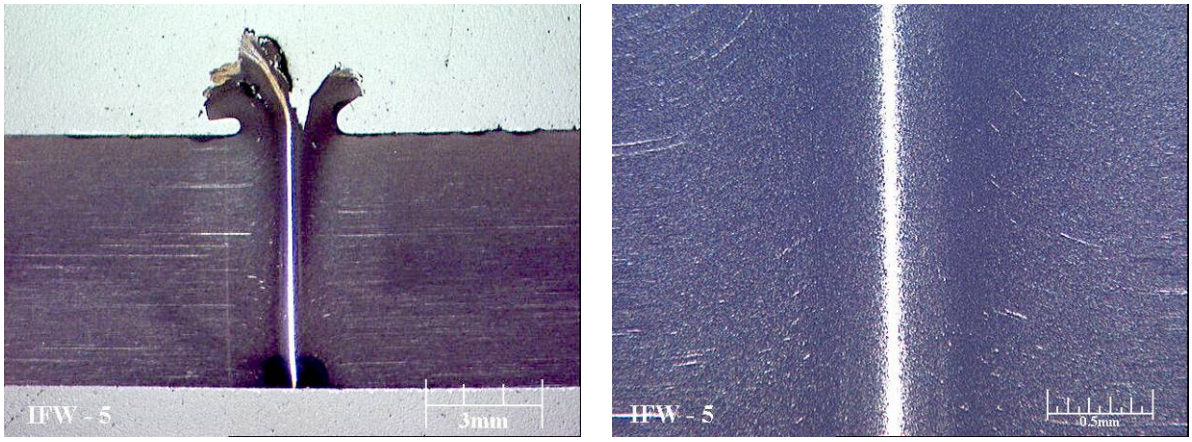

Figure 18. Photomicrographs of Inertia Weld Trial #5

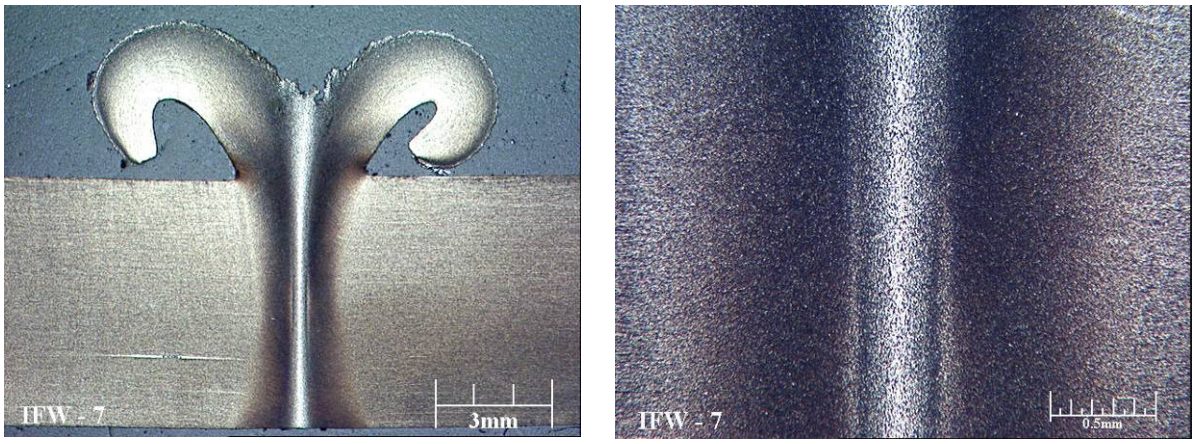

Figure 19. Photomicrographs of Inertia Weld Trial #6

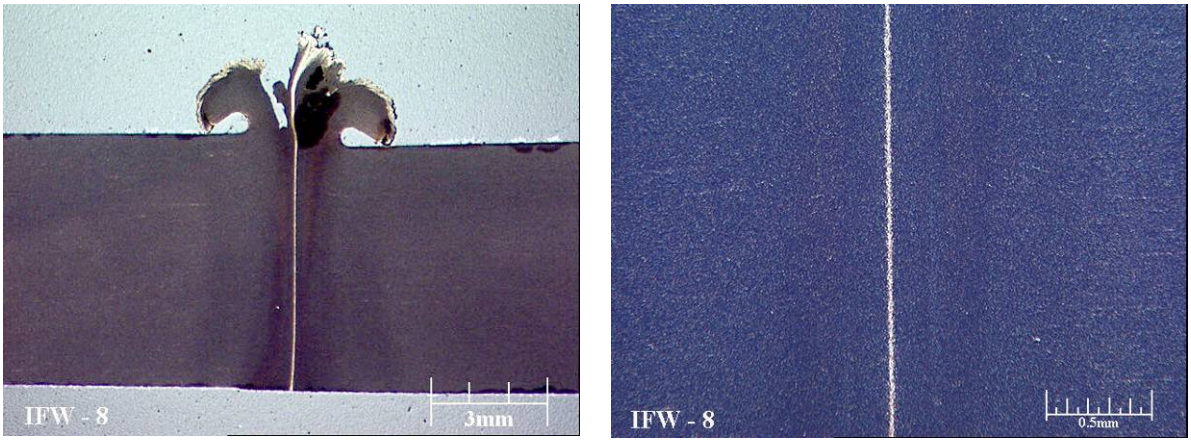

Figure 20. Photomicrographs of Inertia Weld Trial #7

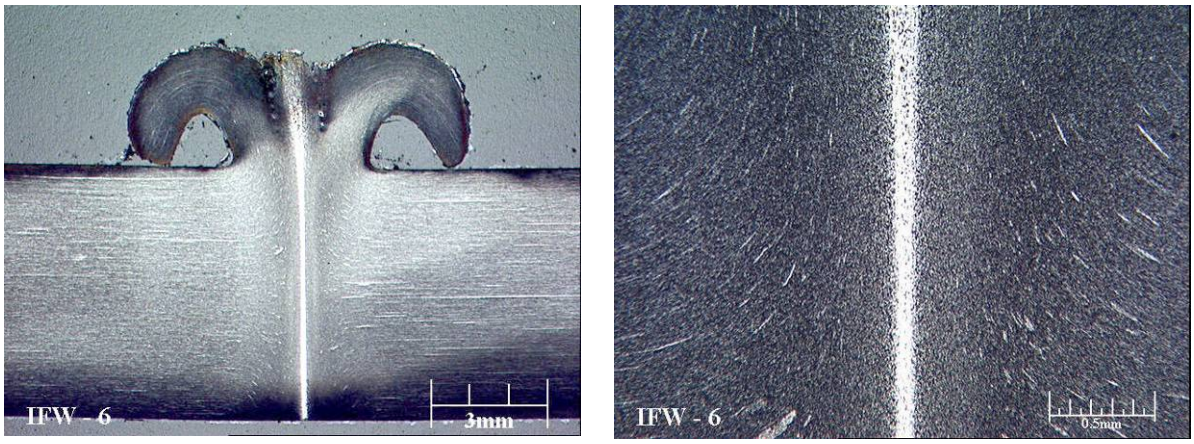

Figure 21. Photomicrographs of Inertia Weld Trial #8

It was observed that lower force levels and higher surface velocities in the friction and upset phases of the inertia welding process resulted in larger grains than at higher forces and lower surface velocities. Lower force weld trials also tended to exhibit flash characteristics typical of liquid formation during the weld process as shown in Figure 22. In a friction weld, that produced a rough surface finish with small particles at the surface of the flash (as indicated in Figure 22), the temperature in the process created liquation at some level. This was typically eliminated or reduced by modifications to the friction welding process. The flash was associated with large grains in the worked area of the weld joint as shown in Figure 23. It is unclear, but it appears that incipient melting may have been present in welds made with lower thrust loads and high surface velocities. This would undoubtedly lead to the formation of deleterious phases or discontinuities in the weld joint.

In order to eliminate these features in the weld joint, the weld force was incrementally increased and the surface velocity of the weld was reduced to suppress the peak temperature in the welding process. Increased force weld trials were conducted using a two-stage weld and forge approach for heating the material at low joint stress and forging the material out of the joint at higher stress. This approach worked well in maintaining low joint stress at higher surface velocity. In the higher force welding trials cracking was observed as shown in Figure 24.

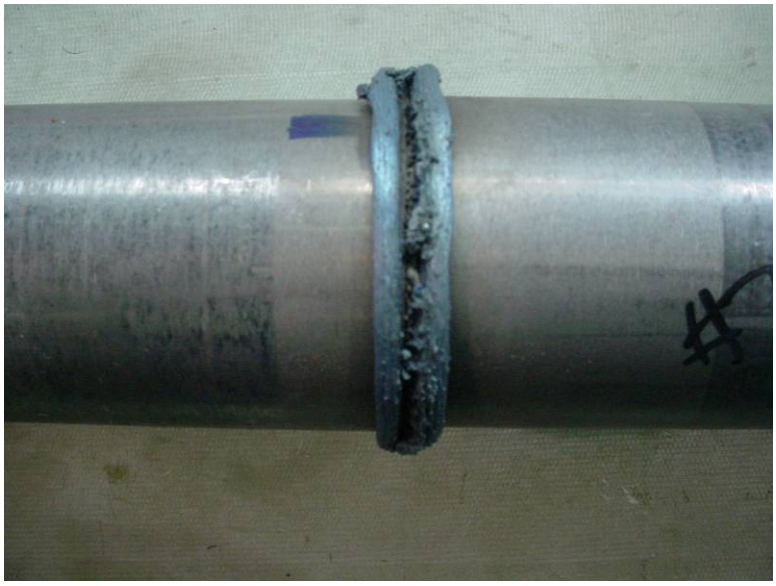

Figure 22. Flash Curl Typical of Thrust Load Inertia Friction Welds

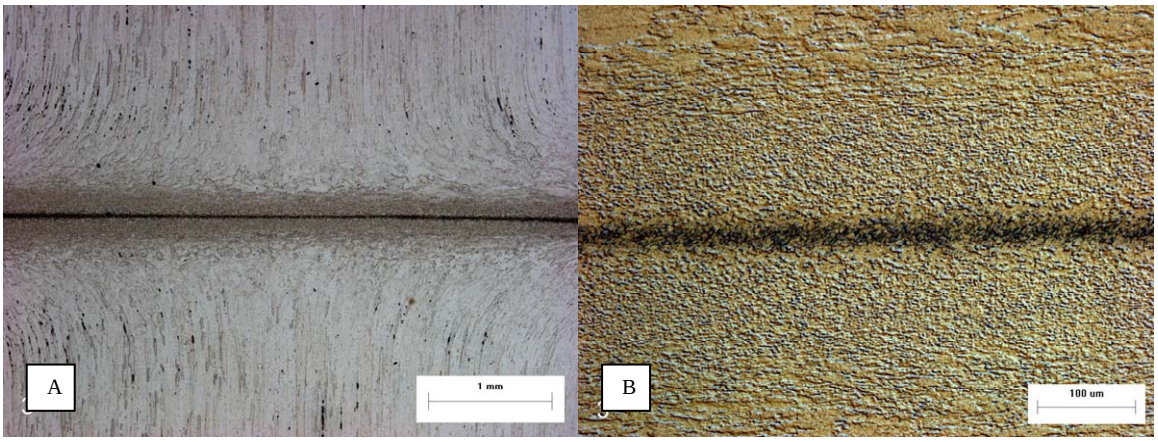

Figure 23. Macroscopic (A) and Microscopic (B) View of Weld Joint Produced with Low Thrust Force during Inertia Welding

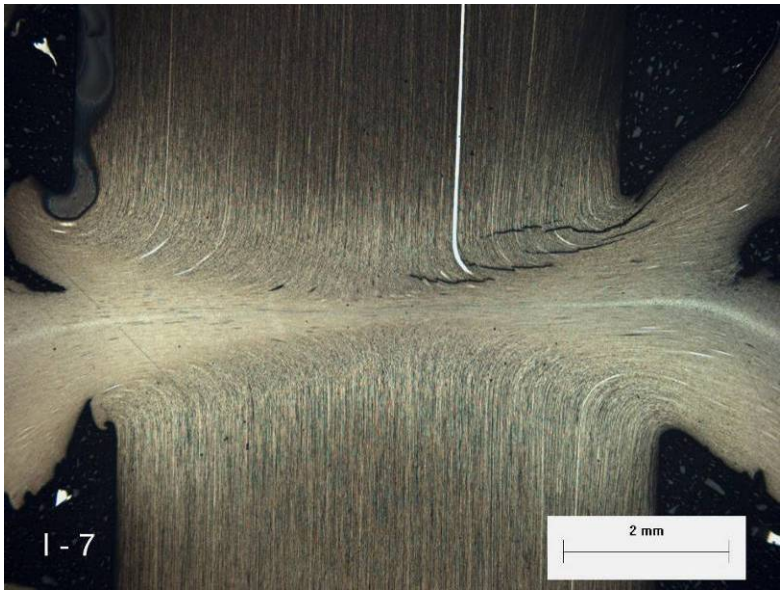

Figure 24. Weld Produced with Typical Two-stage Force showing Cracking in Far Heat Affected Zone

In order to eliminate this cracking, a single stage high force approach was used. Welds made with a single high thrust load thoughout the process, approaching the yield strength of the material at 871°C (1600°F) and lower surface velocities produced a much different flash curl displaying no characteristics associated with the formation of liquid during welding as shown in Figure 25. The resultant microstructure appeared with a much finer grain size with no indication of liquid formation during the welding process (see Figure 26A). The inertia weld bondline, shown in Figure 26B, shows that grain growth has been suppressed in the weld joint with grain elongation retained in the weld joint centerline.

Figure 25. Flash Curl Typical of High Thrust Load Inertia Friction Welds

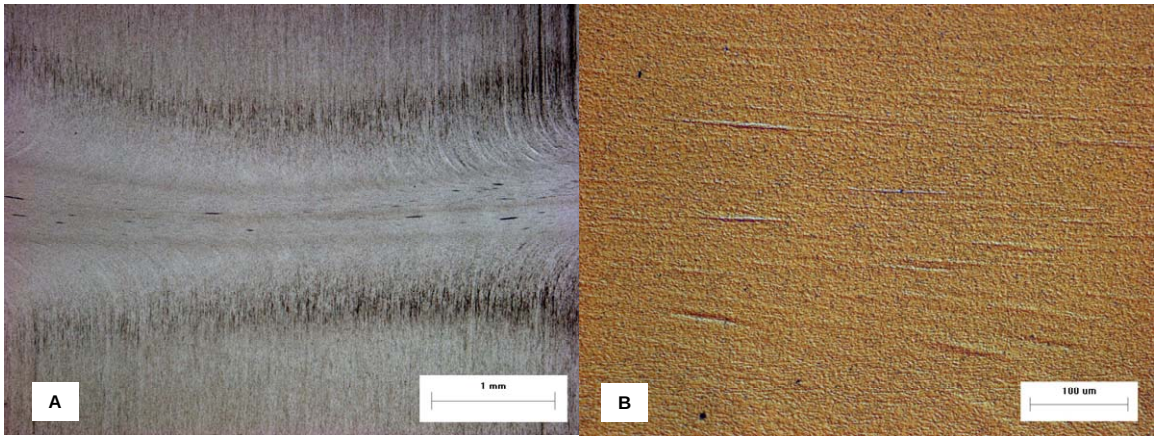

Figure 26. Macroscopic (A) and Microscopic (B) Bondline View of Inertia Weld Produced with High Thrust Loads and Reduced Surface Velocities

Observed in the friction welds were three distinct regions, 1) the coarsened grain region in the center, 2) the recrystallized fine grain region , 3) and the forged area where grain direction changes and transitions into base metal. Use of the lower surface velocities and higher thrust loads appeared to minimize grain growth and produced a different aspect ratio grain in the center region while reducing the size of these regions significantly. One important note is that low upset or weld force appeared to result in the formation, and possible retention, of liquid in the weld joints. This apparent formation of liquid during welding could lead to agglomeration of dispersoids and appeared to be associated with large grains with heavy grain boundaries. These features may have been detrimental to joint performance at elevated temperatures.

The fine elongated grains in the high thrust load/lower surface velocity weld joints most likely retained a high level of cold work or strain upon completion of the weld. This cold work would respond to any subsequent post weld heat treatment in the form of recrystallization which was reportedly beneficial for alloy performance at elevated temperatures.

Friction welds between MA956 tubing and 601 tubing were also conducted. A reduction in thrust load in comparison to welding MA956 to itself was required to prevent bending of the Inconel 601 during the inertia friction welding process (see Table 9). A section of a joint produced with inertia friction welding is shown in Figure 27. The summary table shows the optimized welding parameters used in all evaluation and fabrication trials conducted in the program.

5.3.2 Subask 3.2 – Transient Liquid Phase (TLP) Bonding

(Task activity removed from project. Process not applicable for production manufacture of heat exchanger tubes. Process is still being explored independently by ORNL.)

Transient Liquid Phase Bonding: Past boriding work had resulted in the successful production of samples with uniform borided layers 3 to 5 microns thick. Three sets of bonding trials were processed in a hot isostatic press (HIP) furnace. The bond trial samples included recrystallized/recrystallized, non-recrystallized/recrystallized, and non-recrystallized/non-recrystallized samples of the MA956 alloy, where both pieces in the bonding couple had been borided, as well as three bonding couples with only one borided piece. The joining of the non-recrystallized to recrystallized material was performed in order to cause grain growth across the interface during the joining process. Initial joining trials resulted in joints that appeared void-free with a few residual particles and limited grain growth across the interface (see Figure 28).

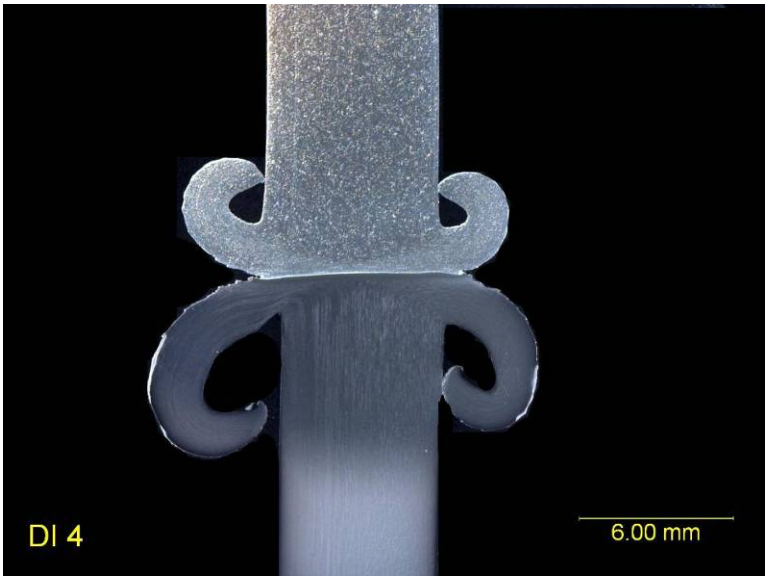

Figure 27. Inertia Friction Weld Joint Inconel 601 to Rx'd MA 956

Table 9. Welding Parameters for Inertia Friction Welds

Materials	Inertia (wK2)	Spool Speed (RPM)	Thrust Load kg (lbs)	Loss of Length mm (in.)	Flash Curl
MA 956 (non-Rx)	900	605	34,019 (75,000)	12.2 (.482)	Smooth thin
MA 956 (Rx)	900	600	34,019 (75,000)	12.1 (.475)	Smooth thin
Rx MA 956 (Rx) to IN 601	900	570	30,390 (67,000)	10.7 (.420)	Smooth med thickness

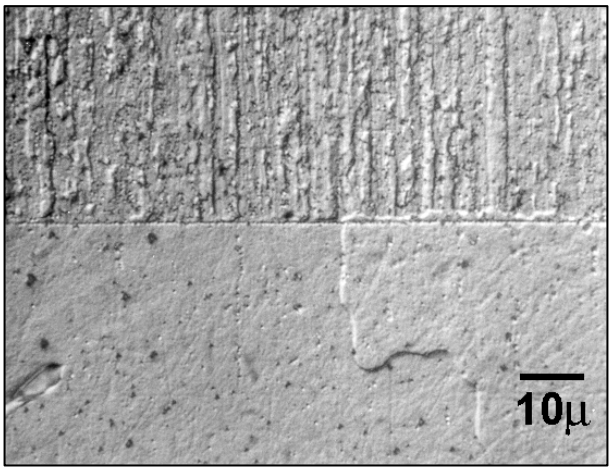

Figure 28. Joint Produced using Transient Liquid Phase Bonding

Work continued on the MA956 diffusion bonding trials using a vacuum hot press furnace. This included six exploratory bonding trials on 12.7 mm (0.5-in.) diameter bar, and initiation of an eight-run parametric study designed to identify the most important process variables in diffusion bonding of the MA 956 alloy. The six bonding trials included joining borided recrystallized rod to unrecrystallized rod, borided unrecrystallized rod to recrystallized rod, and recrystallized rod to unrecrystallized rod using a thin interlayer of elemental boron. Several of these samples showed significantly stronger evidence of grain growth across the prior joint interface than observed in prior trials. Figure 29 shows the bondline of the fifth bonding trial.

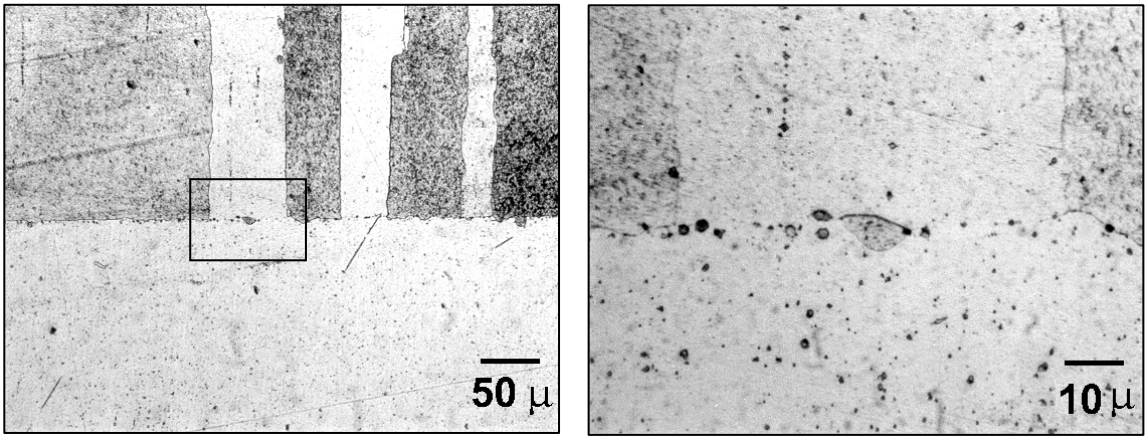

Figure 29. (a) Micrograph of Borided, Recrystallized MA956 (top) Bonded to Non-borided, Non-recrystallized MA956. Box in (a) shows Approximate Region shown in (b). Samples Etched with HCl.

As work continued on determining the most appropriate hot pressing parameters for joining the MA956 alloy, results showed there may be little benefit to boriding one or both of the mating MA956 surfaces prior to bonding. Even with the low levels of boron added using the protocols developed earlier in the program, nearly all of the borided joints continued to exhibit residual borides at the joint interface, which may inhibit grain growth across the interface after bonding. Workpieces bonded with out boron, however, showed a relatively clean interface and evidence of grain growth across this interface. Figure 30, for example, shows a ring of recrystallized MA956 tube bonded to a ring of unrecrystallized MA956 tube 63.5 mm OD × 6.35 mm wall (2.5-in. × 0.25-in.). The two pieces were bonded by hot pressing at 1200°C (2192°F) for two hours, followed by four hours at 1340°C (2444°F). Note that there is very little difference in the microstructure between the two pieces or between the joint and the surrounding matrix. Perhaps even more importantly, a number of grains clearly appear to have grown across the interface during bonding. Such a microstructure is likely to exhibit good elevated temperature tensile performance.

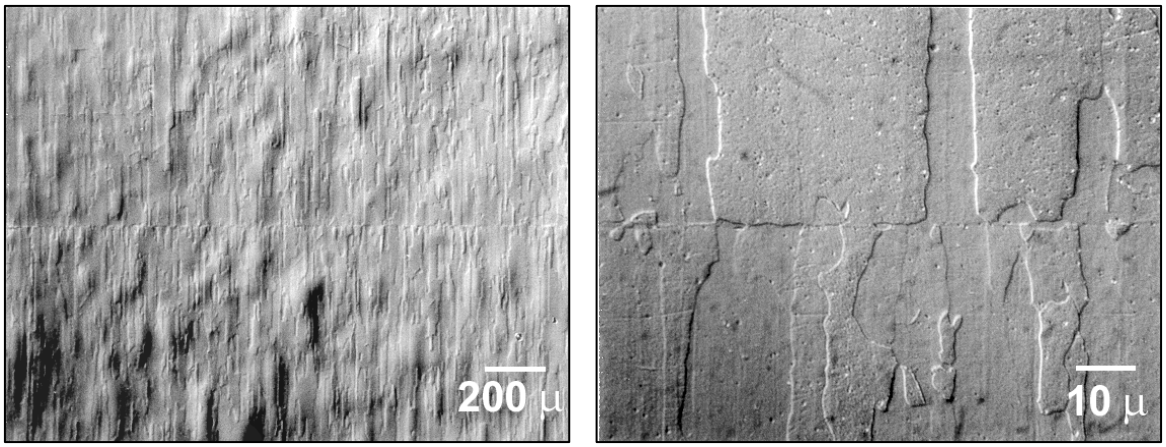

Figure 30. Micrograph of Bondline Microstructure Produced by Hot Pressing Recrystallized and Unrecrystallized MA956 Tubing

In order to join MA956 tubes using the diffusion bonding process, it is believed that this will require joining two recrystallized tubes using an intermediate tapered ring of unrecrystallized material. This "3-body" joint would consist of two sections of recrystallized MA956 tubing machined at a 45° angle which fit into a surrounding "collar" of non-recrystallized MA956 containing two mating 45° angles. Figure 31 shows a diffusion bonded joint observed in the one of these 3-body coupons. This joint was produced using a modified pressing schedule incorporating an initial high-pressure, low-temperature deformation segment prior to diffusion bonding. This modified schedule improved the alignment of the three joint sections, although slight bulging did still occur in the mid-section of the sample. Metallographic examination of the cross-section of this sample revealed that joint bonding was much improved over prior samples. Micrographs of the joint are shown in Figure 32.

This task activity was eliminated from the project for further development. The process is not amendable for wide-scale manufacture of heat exchanger tubes. The process is still being explored independently by ORNL.

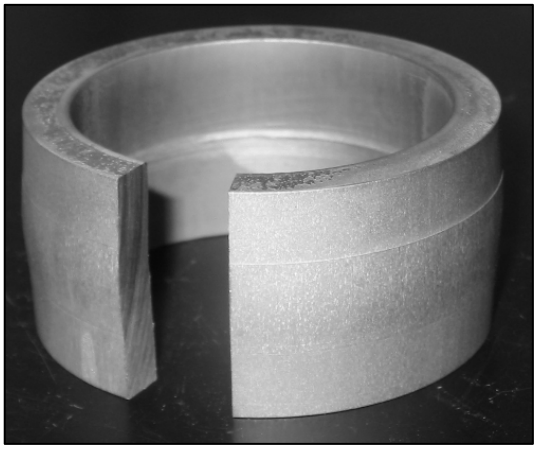

Figure 31. Diffusion Bonded Joint in 3-body Coupon

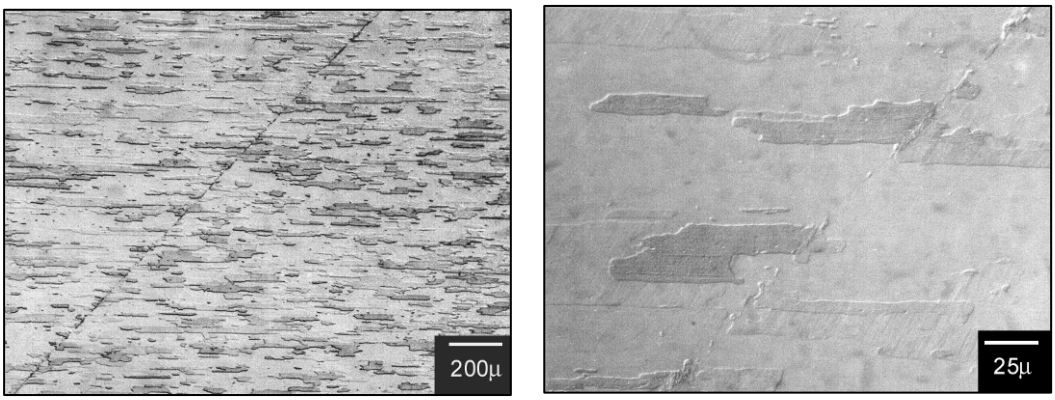

Figure 32. Micrograph of Hot Press "3-body" Joint of MA956
Note bondline running diagonally through image. Etched with HCl.

5.3.3 Subtask 3.3 – Explosive Bonding (Modified to Friction Stir Welding – FSW)

Explosive Bonding: Initial explosion weld trials began with the MA956/IN 601 dissimilar joint. Parametric calculations for the explosion welding of an 9.5 mm (0.375-in.) thick MA956 plate, with an estimated room temperature yield strength of 551.6 MPa (80 ksi), indicated the potential for successful welding of a102 mm × 152 mm (4-in. × 6-in.) plate samples would be marginal. Therefore, an initial setup for an MA956-to-601 weld trial was disassembled and the MA956 plate was milled down to 6.35 mm (0.25-in.) thickness to match the thickness of the 601 plate. The setup was then shot (explosion welded) with the MA956 plate accelerated down onto the stationary 601 plate. Ultrasonic inspection of the sample indicated a non-bond at the start-up of the joint 25-38 mm (1-1.5-in.) long with the remaining 114-127 mm (4.5-5-in.) of the joint being bonded. This preliminary examination indicated a successful weld between the material couple.

Setup for explosion welding the first sample of MA956-to-MA956 was also prepared and welded. Initially, the cladding or accelerated plate was milled down to 0.25-inch thickness, the same as had been done for the MA956-to-601 weld trial. The base or stationary MA956 plate, however, was not reduced in thickness, as its thickness does not effect the explosion welding collision conditions. The explosion welding parameters used to weld this sample were the same as those used on the MA956-to-601 weld trial with a minor change in the setup to reduce the amount of non-bond experienced on the initial sample shot. Following this explosion welding trial, preliminary ultrasonic inspection revealed the sample to be completely bonded over the entire 102 mm × 152 mm (4-in. × 6-in.) surface area.

Two samples from the MA956 plate explosion welded to MA956 plate, and two samples from the MA956 plate joined to 601 plate were extracted for metallographic analysis and shear testing. Figure 33 shows the interface of the MA956/MA956 and MA956/601 welds after a post explosion weld heat treatment at 1000°C (1832°F) for 1 hour. As shown in these micrographs, the wave-shaped interface characteristic of a successful explosion weld was present. Table 10 shows the results of the shear testing performed on the as-welded samples and the post weld heat-treated samples. The heat-treated MA956/MA956 sample showed a slight decrease in bond strength as a result of the heat treatment whereas the MA956/601 sample showed an increase in shear bond strength after the heat treatment. However, the measured shear strength for the heat treated MA956/601 sample may have been artificially high due to the relatively high ductility of the annealed 601 material.

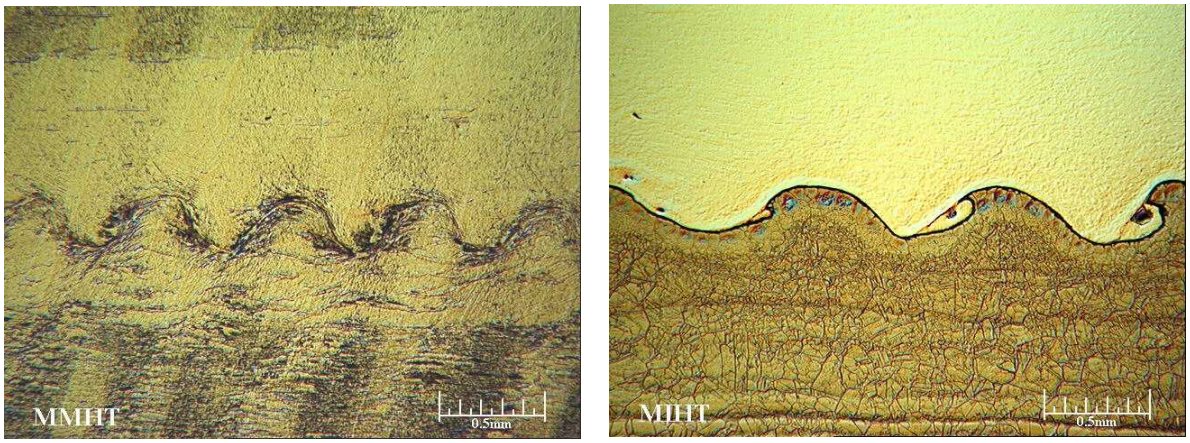

(a) MA956/MA956 **(b) MA956/601**

Figure 33. Optical Micrographs of Interface of Explosion Weld between (a) MA956 and MA956 Plate and (b) MA956 and 601 Plate

Table 10. Shear Test Results of Explosion Welds Made on MA956 Plate to MA956 Plate and MA956 Plate to 601 Plate

Sample	Shear Strength MPa (ksi)
MA956/MA956	565.4 (82.0)
MA956/MA956 + Heat Treatment*	532.3 (77.2)
MA956/601	548.1 (79.5)
MA956/601 + Heat Treatment*	611.6 (88.7)**

* *Heat treatment performed at 1000°C (1832°F) for 1 hour*

** *Value may be artificially high due to ductility of the 601 alloy*

5.3.4 Subtask 3.4 – Friction Stir Welding

Circumferential friction stir welding was conducted on MA 956 tube. The diameter of MA 956 tube is 63.5mm (2.50-in.), and the wall thickness was 6.35mm (0.25-in.). The pin tool material used for welding MA 956 is proprietary alloy specifically developed for welding high temperature materials. No inert gas shielding was used during FSW.

The tube welding fixture shown in Figure 34 was used for the circumferential weld of MA 956 tube. Figure 35 is a close-up photo of the setup. Total of 13 weld trials were conducted to develop the weld schedule and make a full 360° circumferential weld. Table 11 lists the details of weld conditions of all 13 trials.

Weld trials 1-5 were made using tools with 19mm (0.750-inch) shoulder diameter and 6.1mm (0.240-in.) pin length. The tool's shoulder diameter was reduced to 13.3mm (0.525-in.) for future weld trials in order to keep the ratio of tool's shoulder diameter to the tube diameter low. The pin length was reduced to 3.2mm (0.125-in.) with intent of making partial penetration welds.

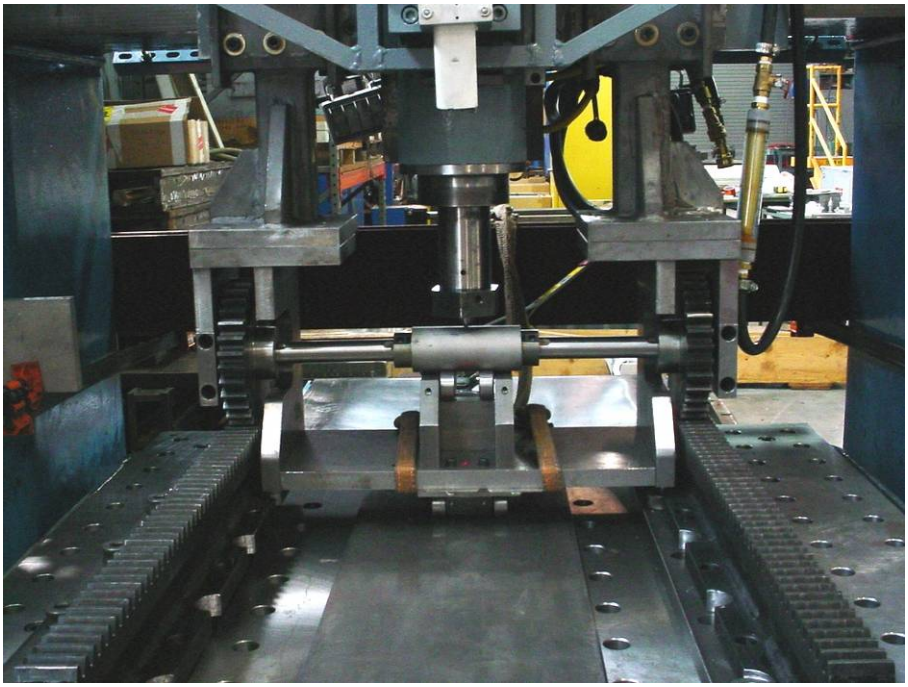

Figure 34. Tube Weld Fixture Setup for Welding MA 956 Tube

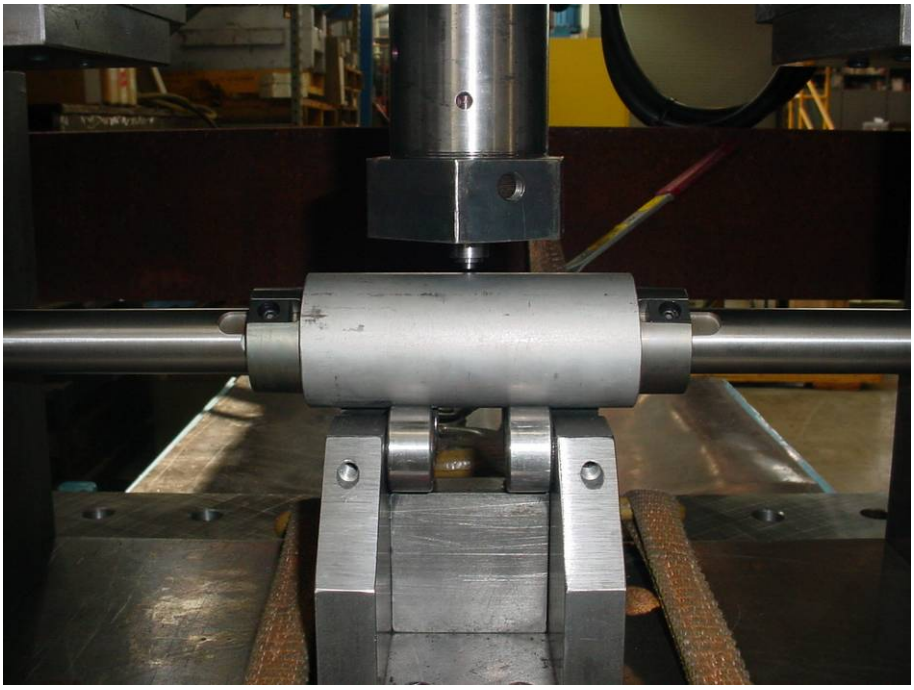

Figure 35. Close-up Photo of Tube Weld Fixture Setup for Welding MA956 Tube

Table 11. Weld Trial Matrix

Weld ID	Pin Length mm (inch)	Pin Diameter mm (inch)	Shoulder Diameter mm (inch)	Plunge Depth mm (inch)	Spindle Speed rpm	Travel Speed mmpm (ipm)	Weld Quality
Trial-1	6.096 (0.24)	14.7 taper to 7.6 (0.58 taper to 0.3)	19.05 (0.75)	6.35 (0.250)	150	101.6 (4.0)	surface defect
Trial-2	6.096 (0.24)	14.7 taper to 7.6 (0.58 taper to 0.3)	19.05 (0.75)	6.35 (0.250)	90~150	101.6 (4.0)	surface defect
Trial-3	6.096 (0.24)	14.7 taper to 7.6 (0.58 taper to 0.3)	19.05 (0.75)	6.35 (0.250)	150	101.6 (4.0)	surface defect
Trial-4	6.096 (0.24)	14.7 taper to 7.6 (0.58 taper to 0.3)	19.05 (0.75)	6.35 (0.250)	120	101.6 (4.0)	surface defect
Trial-5	6.096 (0.24)	14.7 taper to 7.6 (0.58 taper to 0.3)	19.05 (0.75)	5.97 (0.235)	120	101.6 (4.0)	surface defect
Trial-6	3.175 (0.125)	6.553 (0.258)	13.34 (0.525)	3.05 (0.120)	170	101.6 (4.0)	surface defect
Trial-7	3.175 (0.125)	6.553 (0.258)	13.34 (0.525)	3.429 (0.135)	150	101.6 (4.0)	surface defect
Trial-8	3.175 (0.125)	6.553 (0.258)	13.34 (0.525)	4.06 (0.160)	150	101.6 (4.0)	surface defect
Trial-9	3.175 (0.125)	6.553 (0.258)	13.34 (0.525)	4.83 (0.190)	200	101.6 (4.0)	smooth surface weld, no void
Trial-10	3.175 (0.125)	6.553 (0.258)	13.34 (0.525)	4.318 (0.170)	200	101.6 (4.0)	surface defect
Trial-11	3.175 (0.125)	6.553 (0.258)	13.34 (0.525)	4.318 (0.170)	250	101.6 (4.0)	surface defect
Trial-12	3.175 (0.125)	6.553 (0.258)	13.34 (0.525)	4.83 (0.190)	200	101.6 (4.0)	smooth surface weld, no void
Trial-13	3.175 (0.125)	6.553 (0.258)	13.34 (0.525)	4.83 (0.190)	200	101.6 (4.0)	smooth surface weld, no void

During weld schedule development, spindle speed varied between 90 to 250 rpm while travel speed was kept at 1mpm (4 ipm). Decent circumferential weld as shown in Figure 3 was producde at 200 rpm and 1mpm (4 ipm) with 4.8mm (0.190–inch) plunge depth. The weld was void free as shown in the macrograph (Figure 4).

Figure 36. Circumferential Friction Stir Weld of MA956 Tube

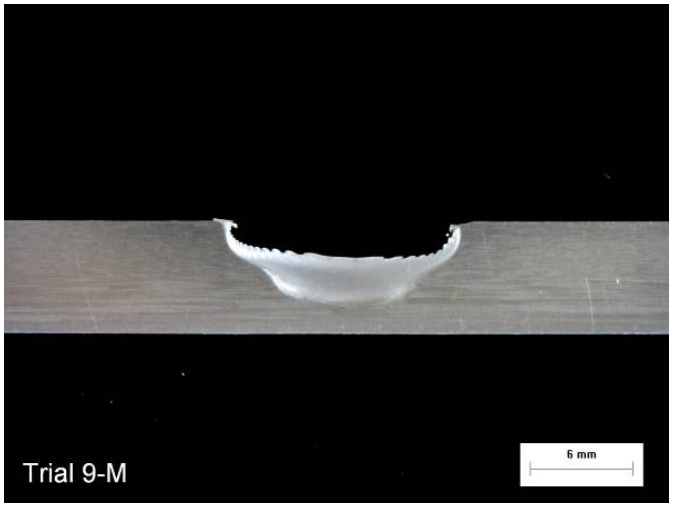

Figure 37. Macrograph of MA956 Circumferential Weld

It was evident that there was undercut on the circumferential FSW, although the weld was void free. Additional development work was required to reduce/eliminate the undercut including redesign of pin tool and fine-tune of weld schedule. It was decided not to continue development of the process within this project due to the associated cost to complete the activity.

5.3.5 Subtask 3.5 – Magnetic Pulse Welding

Initial magnetic pulse welding trials were done upon a small unit that had the capacity of 20kj. Weld trials were done using 12.7mm (0.5-inch) diameter tubes. A lap joint configuration was used in the weld trials. An aluminum alloy sleeve detail is used to aid in coupling the pulse energy to the joint between the MA 956 details (Figure 38 and Figure 39). A photomicrograph of a bondline is shown in Figure 40. Marginal bonding was achieved. It was felt that success could be obtained with a system that is capable of more energy. With that in mind a new system was acquired by EWI that possessed the energy capacity of 90kj. A photograph of the unit is showed in Figure 41.

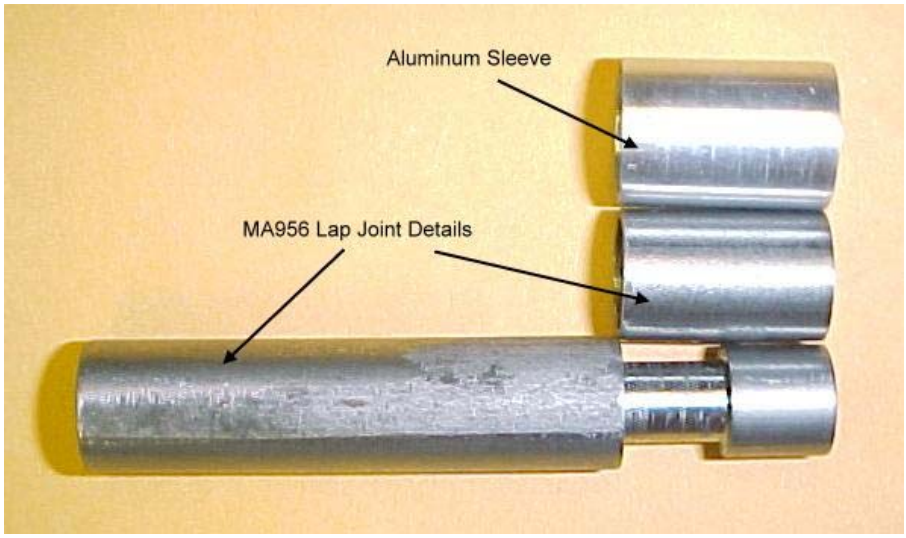

Figure 38. Weld Details for Magnetic Impulse Welding

Figure 39. Initial Weld Trial After Magnetic Impulse Welding (aluminum sleeve removed)

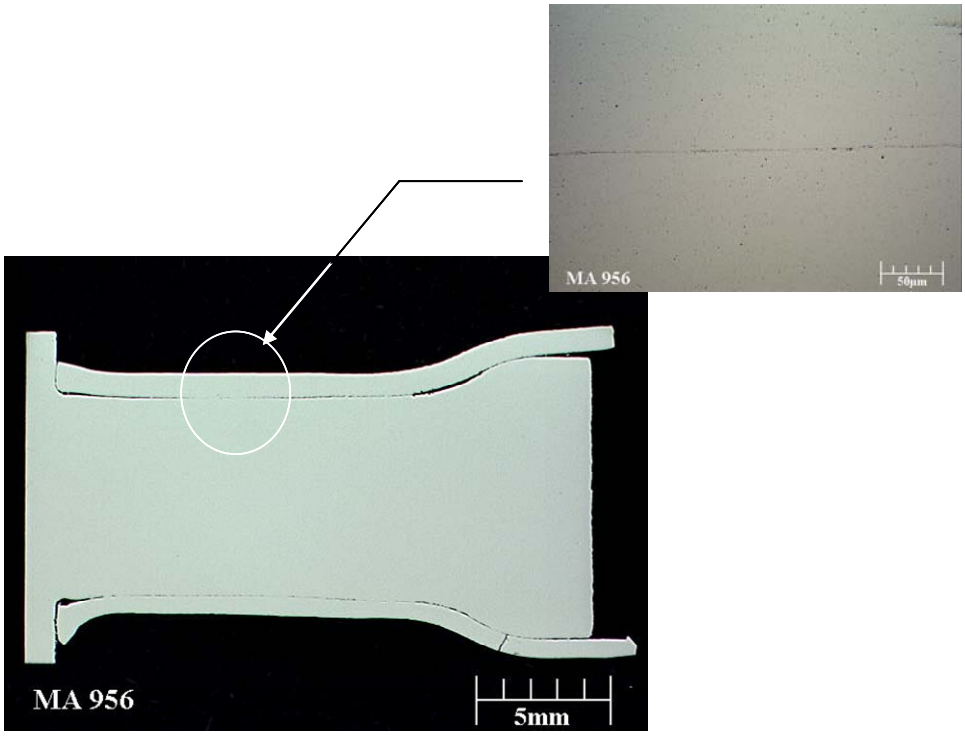

Figure 40. Photomicrograph of Magnetic Pulse Weld

Figure 41. 90kj Magnetic Impulse Weld System Installed at EWI

MA956 tube material was prepared for welding by producing a lap joint configuration. The tubes were prepared by machining the ID of one tube and the OD of the mating tube so that the 2 tubes will fit together for welding with appropriate standoff distance for magnetic pulse welding. A sketch of the tube joint geometry is shown below in Figure 42. Initial weld trials were performed with 1/4t wall thickness (joint thickness 1/2t). A conservative approach was used initially with this wall thickness to validate the process. For initial weld trials with the MA956/601 couple, the 601 tube was placed outside of the mating MA956 tube. Photographs in Figure 43 show equipment setup for welding the MA956 tubes.

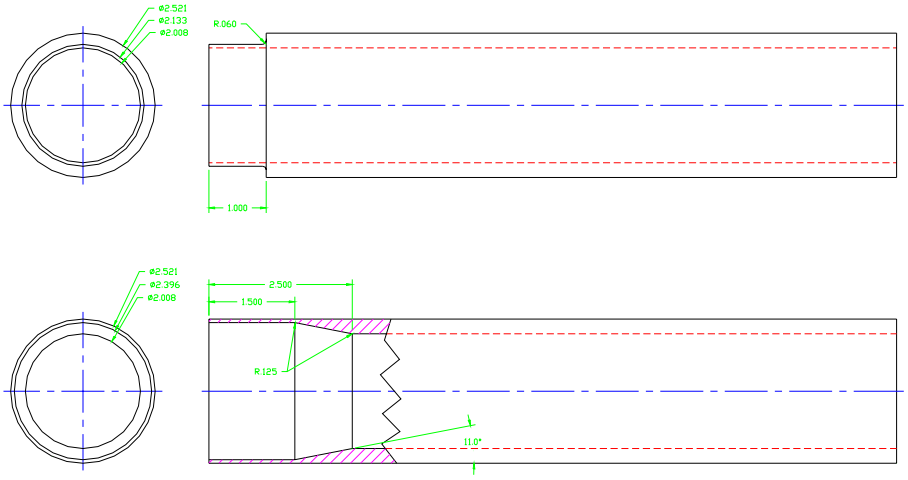

Figure 42. Sketch of Lap Joint Configuration for Magnetic Impulse Welding

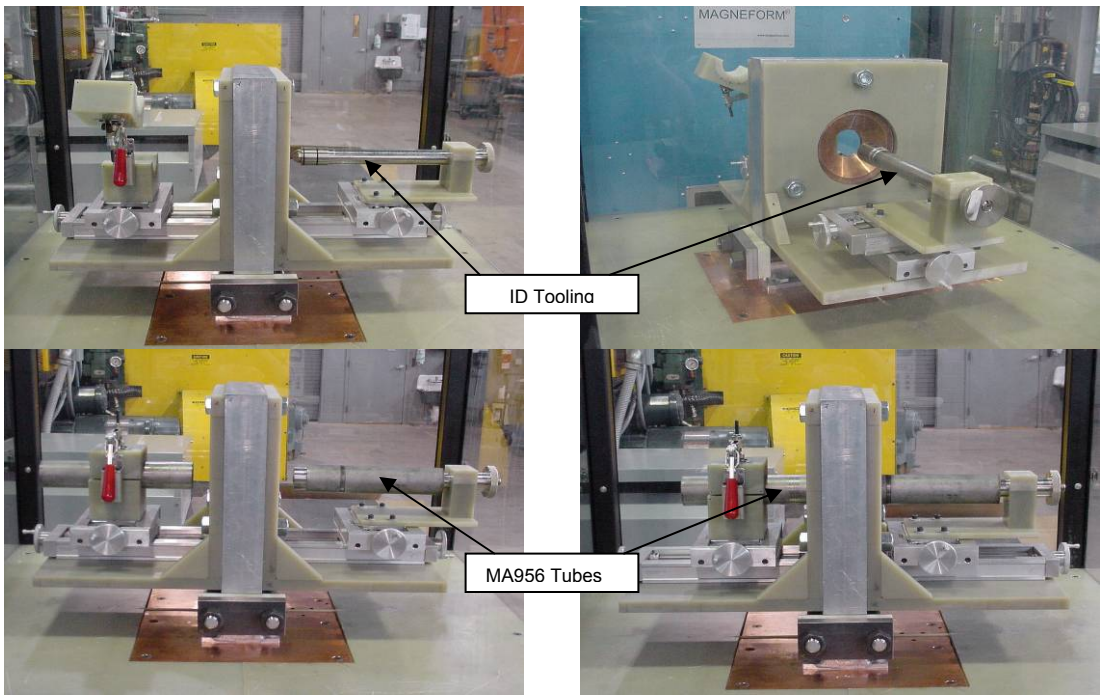

Figure 43. Tooling/fixture Setup for Magnetic Impulse Welding of Tube Test Specimens

Eight trials were performed. The aluminum coupling sleeve was changed to copper to facilitate energy transfer to the joint. Figure 44 shows assembly and completed weld of the MA956/MA956 tubes. Figure 45 shows photomicrographs of the weld joint. It was observed that the MPW joint has a similar appearance as that of the explosion weld trials.

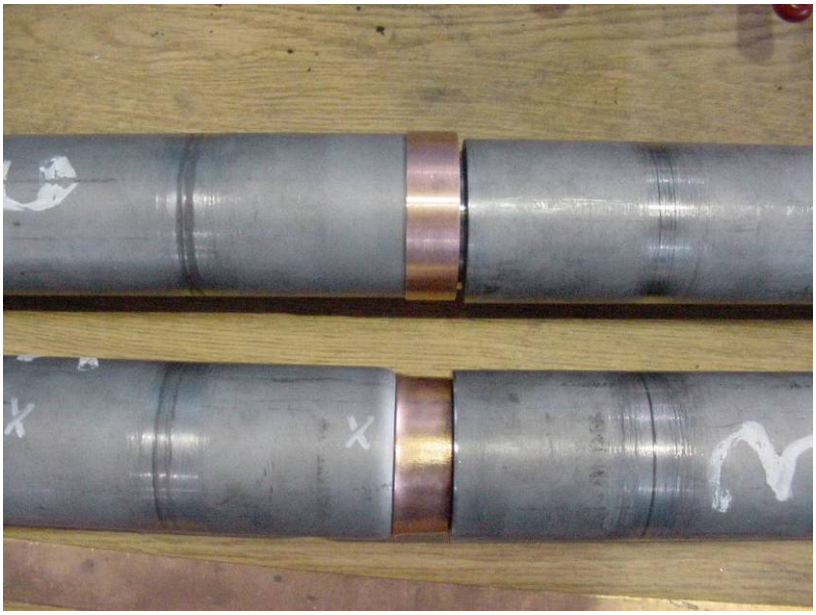

Figure 44. MA956/MA956 Assembly for Magnetic Pulse Welding with Copper Coupling Sleeve. Before and after weld showed upper and lower, respectively.

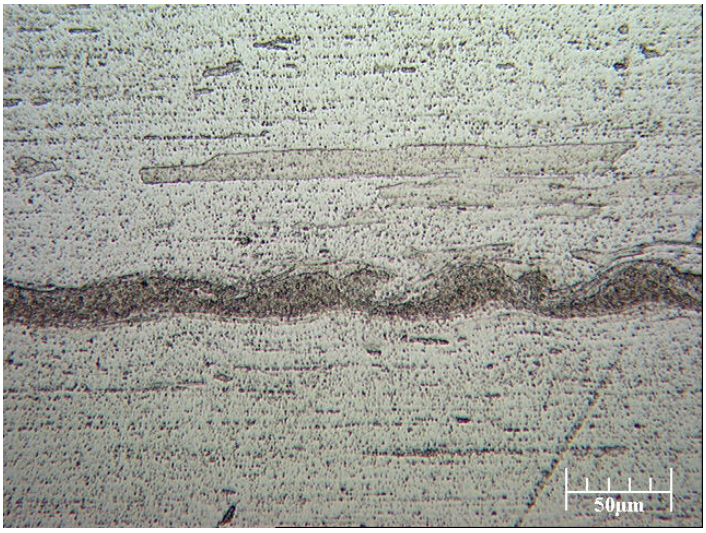

Figure 45. MA956/MA956 MPW Cross Section of Joint

The initial MPW processing trails with reduced wall thickness showed that MA956 tubes could be joined successfully. It was determined through process modeling that a larger capacity machine would be required to perform full thickness welds for the tube application to support the Vision-21 program. As such, MPW was not pursued for further development in this project.

5.3.6 Subtask 3.6 – Flash Butt Upset Welding

Welding Trials were conducted on a system containing a 600KVA AC transformer with a 16-volt secondary and a rapid upset air over oil system that is capable of generating 86,183 kg (190,000 lb) of thrust load. Dies were cut to match the OD of the pipe and backstops were used to prevent slippage of the short pipe section in the welder jaws during upset. Welding trials were started using welding parameters typical of Inconel 718 and through iterative trials, welding parameters and processing conditions were developed to produce a solid-state weld joint. Weld quality was assessed by metallographic examination, SEM analysis, and high temperature tensile testing.

Initial trials were conducted where weld joints were produced under a variety of conditions. The photomicrograph in Figure 46 shows initial results that confirmed the ability of using the process to join MA956 to itself. Although the bondline was evident, the weld remained intact upon cooling and destructive testing. One obstacle identified in the process was the ability to flash as the material itself is somewhat electrically resistive. This resistance resulted in a significant voltage drop through the material to get the voltage to the flashing area to initiate and maintain flashing. The flashing issue was minimized by using a pre-machined profile in a V-shape to initiate the flashing. Without the profile, flashing start-up was often unstable in the as-received material. The flashing issue was eventually traced back to heavy oxides and oils coating the surface of the tubes resulting in a voltage drop at the die to tube contact surface. Note that MA956 is designed to form heavy stable oxides in service. Once the surface were eliminated as a voltage drop source, flash welding trials were successful at initiating and maintaining constant flashing profiles through a variety of flashing acceleration rates

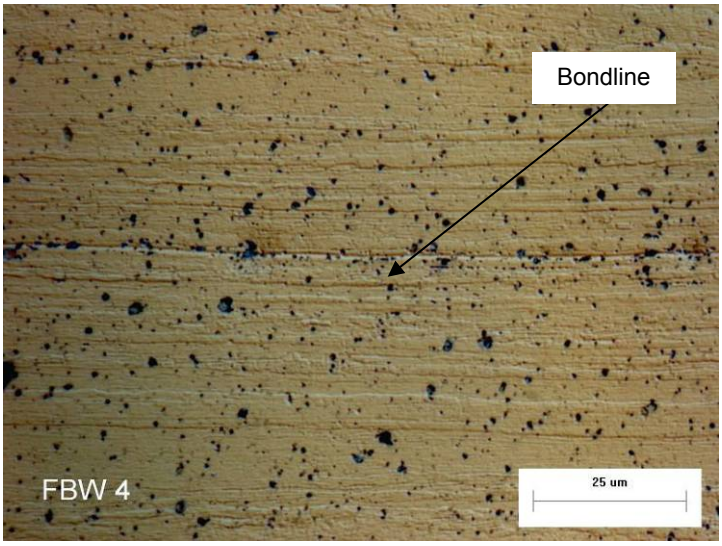

Figure 46. Initial Success with Flash Butt Welding Process

Flashing times and accelerations were examined in order to develop an even flash profile and produce a desirable thermal profile. Typical steel flashing accelerations of approximately 0.51mm per second (0.020 in. per second) squared resulted in stalling of the flashing process and butting prior to upset. The minimum flashing acceleration examined was .051 mm/s2 (0.002-in/s2) which produced and erratic flash. The best flashing acceleration examined which produced stable flashing over the entire stage of the process was .0127 mm/s2 (0.005- in/s2). Once this flashing profile was determined, the upset conditions were examined.

The upset at the end of the flash welding cycle was critical in obtaining a defect free weld joint. Weldments made with less than 6.35-mm (0.25-in.) of upset per side or with elevated levels of upset current displayed bondline voids, heavy grain boundaries (decorated), and significant grain growth. A section of such a weld is shown in Figure 47. A scanning electron microscope (SEM) image of the bondline from this weld joint revealed the defects at the bondline as shown in Figure 48. In summary, all defects on the bondline in these welds were believed to be related to retained liquid in the weld joint or oxidation of alloy additions during the flashing process.

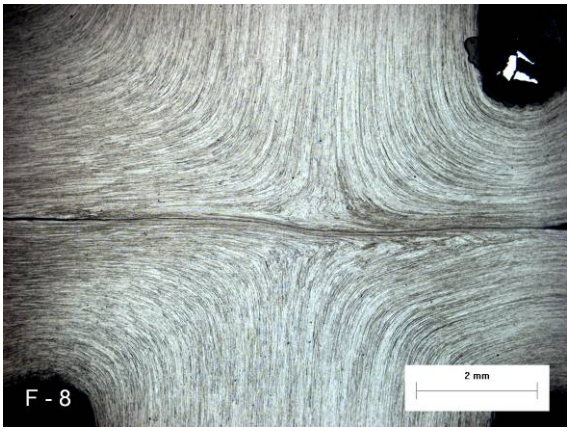

Figure 47. Flash Butt Weld of MA956 to Itself with Inadequate Upset

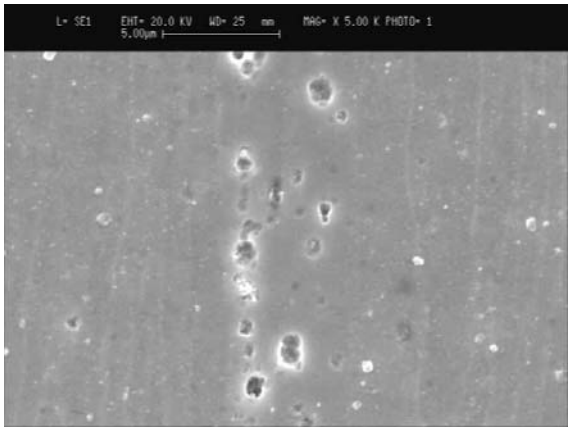

Figure 48. SEM Image of Bondline from Flash Butt Weld from Sample in Figure 47 (rotated 90°)

Early trials conducted used upset currents typical of other superalloys. However the metallographic sections showed some evidence of retained liquid in the bondline area. Stepping the upset current down progressively resulted in bondlines with decreasing amounts of liquation evidence. A working range for the upset current was established between 35% conduction minimum and 45% conduction maximum.

Achieving upset in the MA956 material required adjustments to the typical flash butt welding controls. Typically, an upset operation was set up to continue either until a fixed distance was obtained, or for a fixed amount of time. For the MA956, a slightly different approach was used in order to eliminate the retained liquid. The upset distance was set at a minimum number to be achieved; in the final welds produced this was 14.7 mm (0.580-in.). Additionally, a time constraint of 10 cycles, which was arrived at experimentally, was set to prevent overheating the weld joint area. The force was not released nor was movement stopped once the upset was achieved; rather, the best results were obtained when the upset force was left on for approximately 10 seconds after the target upset distance was achieved. This approach essentially forged all material which has been heated and weakened out of the joint to a fixed joint stress level, in this case is was 34,473 kg (76,000 psi) upset force. The upset continued for several seconds after the upset current was turned off. This approach ha been used in other alloys effectively when they conduct heat poorly, or are sluggish to move or forge, which is precisely what MA956 was designed to achieve – resist creep. Once these lessons learned were applied to the flash welding process, clean weld joints were produced with little or no evidence of retained liquated material in the weld joint as shown in Figure 49 and Figure 50.

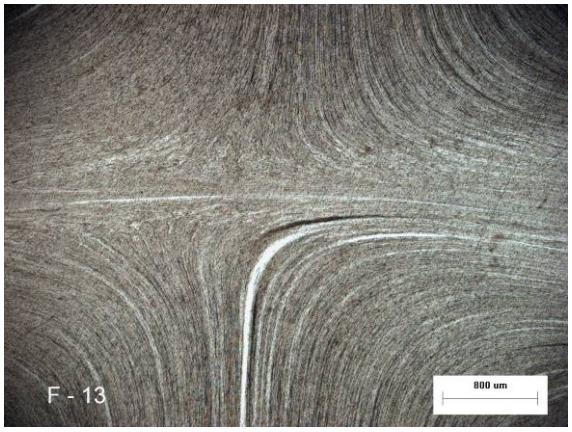

Figure 49. Flash Butt Weld Joint Produced with Increased Flashing Acceleration and Reduced Upset Current

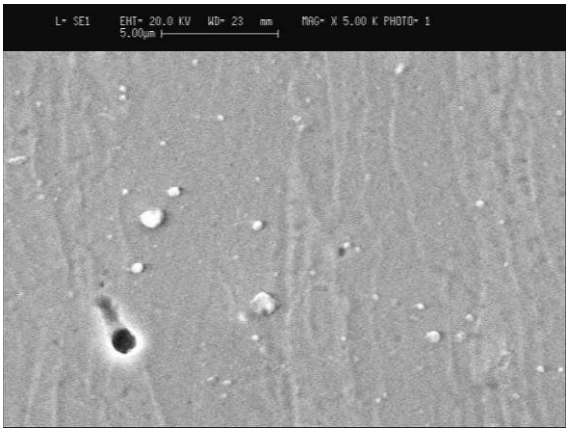

Figure 50. SEM Image of Bondline from Flash Butt Weld with Increased Flashing Rate and Reduced Upset Current (rotated 90° from Figure 49)

With shorter flashing times and greatly reduced upset currents, as compared to other iron and nickel based alloys, a clean bondline can be attained. Further experiments were conducted which examined reduction of flashing time. However, no further improvements were observed.

Also studied in the program were the benefits of using a reducing gas to aid in the protection of the parent material during the flashing cycle. Bottled natural gas was passed underneath the flash weld joint during the process to consume oxygen in the surrounding atmosphere during the flashing cycle. Literature notes that MA956 contains oxygen which can react during heating cycles with the oxide formers in the alloy, such as titanium, aluminum, chromium and form a scale.

Although not thoroughly evaluated, welds made without the reducing gas environment typically failed on cooling. With welds made under the same parameters, and the addition of a reducing gas atmosphere during the welding process, a weld joint was produced that did not fail during the cooling process. It should be noted that this comparison was made with non-ideal flashing and upset conditions which would leave some inherent discontinuities in the weld joint.

The flash butt weld joints produced with the developed parameters displayed coherent bondlines with negligible anomalies typical of the base metal. Control of heat input and maximizing upset rate appeared to be essential in developing a good quality weld joint. Grain direction changes appeared to be similar to those observed in the inertia friction welds. However, grain growth appeared to increase in the flash butt welds. Figure 51 shows the typical weld joint and heat affected zone in a MA956 flash butt weld.

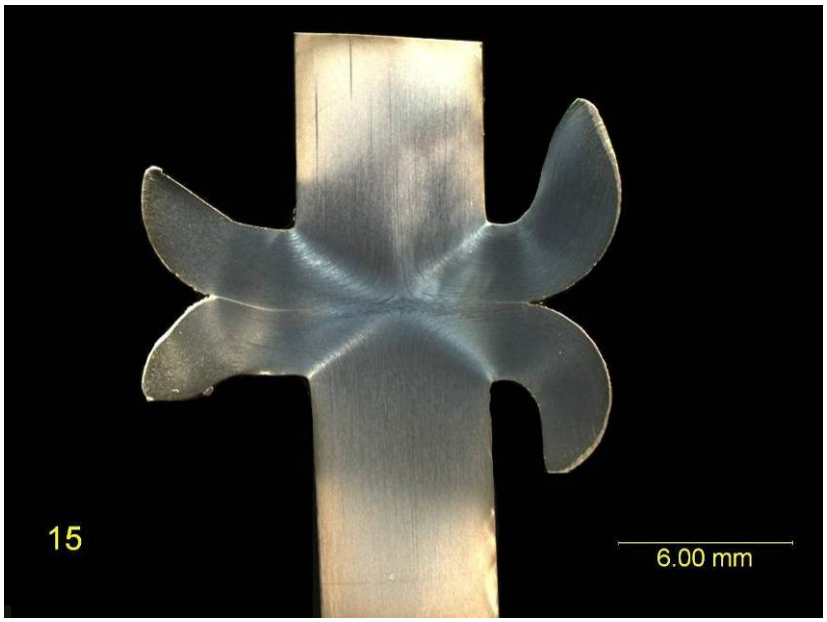

Figure 51. Macroscopic View of Typical Flash Butt Weld Joint

Of interest in the development of the welding process for the different materials combination was that the non-recrystallized, recrystallized, and Inconel 601. In any combination studied, good weld joints were produced with the same flash welding process set-up and parameters. Figure 52 shows a high magnification metallographic section of a flash butt weld between Inconel 601 and MA956. In this photo there was a step transition from one material to the next across the weld joint due to differential hardness between the materials. However, the joint showed no evidence of cracking or liquation type phenomena that are known to create weld joint strength loss in MA956 material.

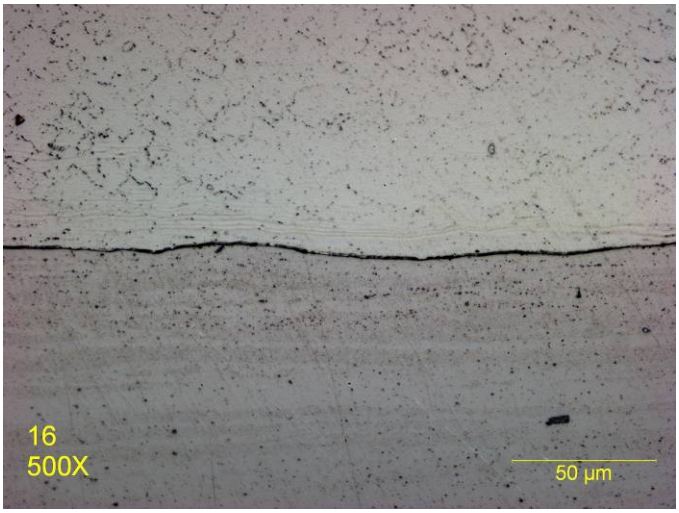

Figure 52. Flash Butt Welded Joint between MA956 and Inconel 601

5.3.7 Subtask 3.7 – Analysis and Elevated Temperature Mechanical Testing

From the joining development activity discussed above inertia friction welding and flash butt welding were the candidate processes selected for ODS heat exchanger tubing fabrication for further characterization of the joints.

Metallurgical Analysis: Optical and SEM analyses of the weld joints were conducted to characterize the joint microstructure. The primary goal of the SEM analysis was to identify any evidence of agglomeration of dispersoids in the joint or heat affected zone in both the IFW and FBW joints. The second goal of the analysis was to characterize the bondline to insure that any formed liquid or recast metal was removed from the joint in the upset stage of both processes. It was observed that the SEM was able to resolve to a higher degree the presence of liquid in the joints due to its higher magnification capability and ability to identify various particulates.

An SEM image of the base metal is shown in Figure 53. In this photo the dispersoid or particulate population and size can be observed as a point of reference. In base metal, the particulates visible were the aluminum/titanium rich, which appeared mostly round and white in color. Smaller particulates were also detectable which contained Yittria, and appeared a light shade of gray. The grains appeared to be high aspect ratio grains aligned with the axis of the tube, (right to left in the image).

The inertia welded joints showed somewhat larger aluminum/titanium particulates as can be seen in Figure 54. The grain aspect ratio was also reduced and the narrow section of the grains changed direction 90 degrees. The grains were then slightly broader and elongated normal to the axis of the tube.

The flash butt welds also showed aluminum/titanium particulates but they compared with the size of those found in the base metal. Figure 55 shows a section of a flash butt weld taken under similar conditions to the base metal and inertia welded joint. The most notable difference between the flash butt weld and the inertia weld was the aspect ratio of the grain. In the flash butt weld, the grains were more highly elongated normal to the axis of the tube suggesting that they may have undergone upset at a lower temperature. Figure 56 and Figure 57 show SEM chemistry analysis of the particulates found in the bondline of an inertia welded joint.

Two sets of MA956 Butt joints were provided to UCSD by EWI for further microstructural examination and TEM studies. The details of the samples are:

A1: Flash Upset Butt Joint – Unrecrystallized
A2: Flash Upset Butt Joint – Recrystallized 1375°C – 1 hour (2507°F)
B1: Inertia Weld Butt Joint – Unrecrystallized
B2: Inertia Weld Butt Joint – Recrystallized 1375° C – 1 hour (2507°F)

In Figure 58, a composite view of the inertia welded and flash-upset joint sections is shown. The joints (situated horizontally in the micrographs) appeared robust with no evidence of flaws or cracking though the tube wall thickness. The heat-affected zone (HAZ) in the inertia-weld is smaller than the corresponding HAZ in flash-upset joint. The inertia joint with its compact HAZ showed a remarkably sharp transition from the base microstructure to the joint region, which appeared to be dominated by a relatively small number of grains oriented normal to the long axis of the tube. Such a feature was indicative of large normal force imposed during joining which resulted in forge-extruding the hot metal at the joint interface. The flash upset joint showed the base microstructure undergoing large grain growth in the vicinity of the joint interface and the outward flow of the grains is clearly evident. However, the joint region itself was again comprised of small grains forge-extruded in the radial directions.

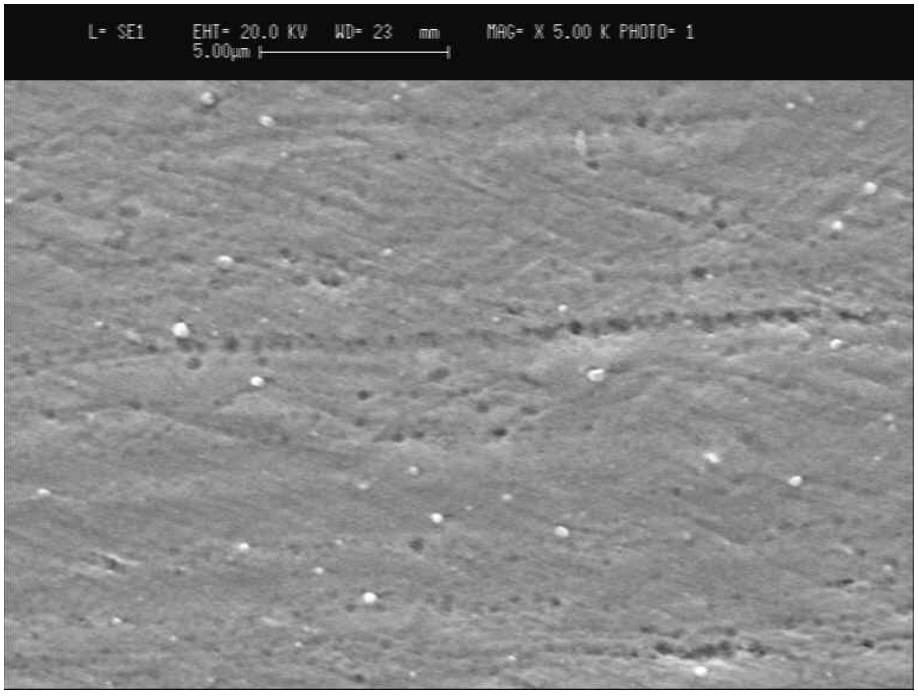

Figure 53. SEM Image of Base Metal MA956

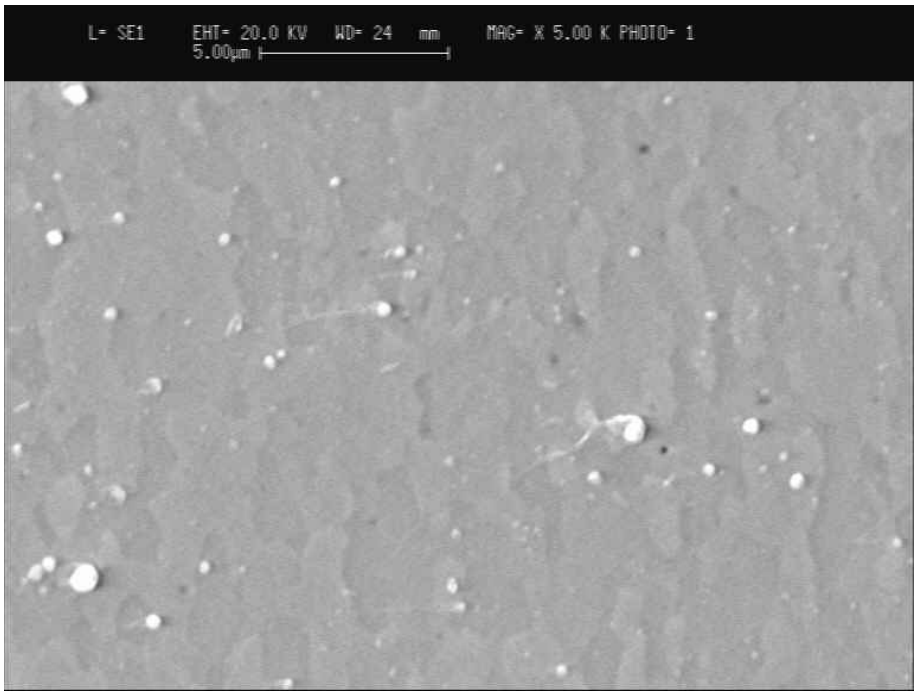

Figure 54. SEM Image of Inertia Friction Welded Joint with Low Surface Velocity and High Upset Force

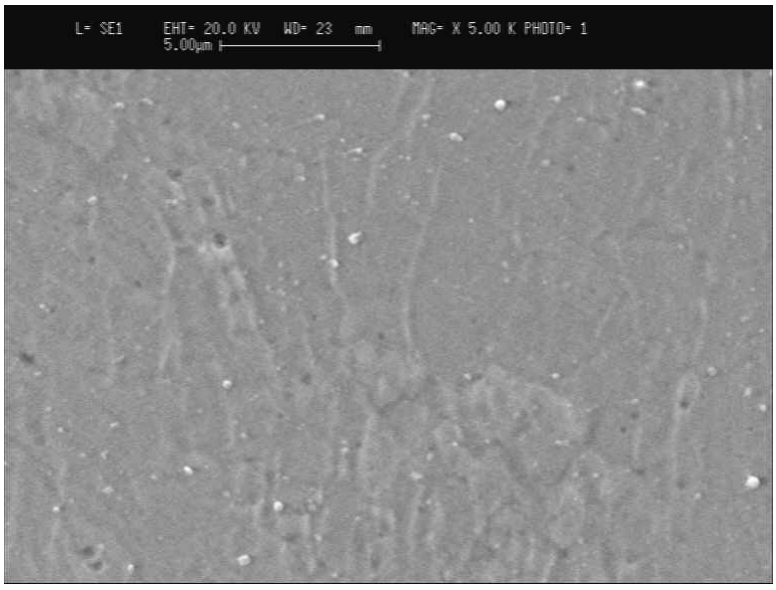

Figure 55. SEM Image of Flash Butt Welded Joint as Developed to Eliminate Bondline Defects

Element	Weight%	Atomic%
C K	2.38	8.67
O K	5.21	14.26
Al K	5.76	9.34
Ti K	0.24	0.22
Cr K	18.35	15.45
Fe K	63.67	49.90
Y L	4.40	2.16
Totals	100.00	

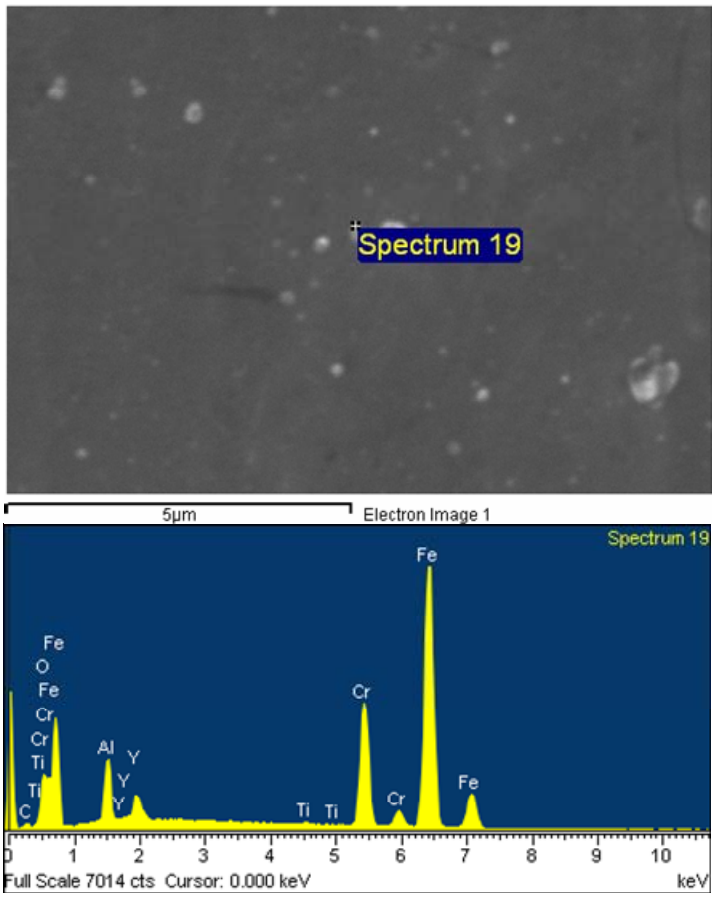

Figure 56. SEM Semi-quantitative Chemistry Analysis of Inertia Weld of Yittria Particulate

Element	Weight%	Atomic%
C K	2.60	7.01
O K	21.90	44.36
Mg K	0.52	0.69
Al K	8.07	9.70
Cl K	0.19	0.17
Ti K	13.64	9.23
Cr K	10.72	6.68
Fe K	31.17	18.09
Y L	11.20	4.08
Totals	100.00	

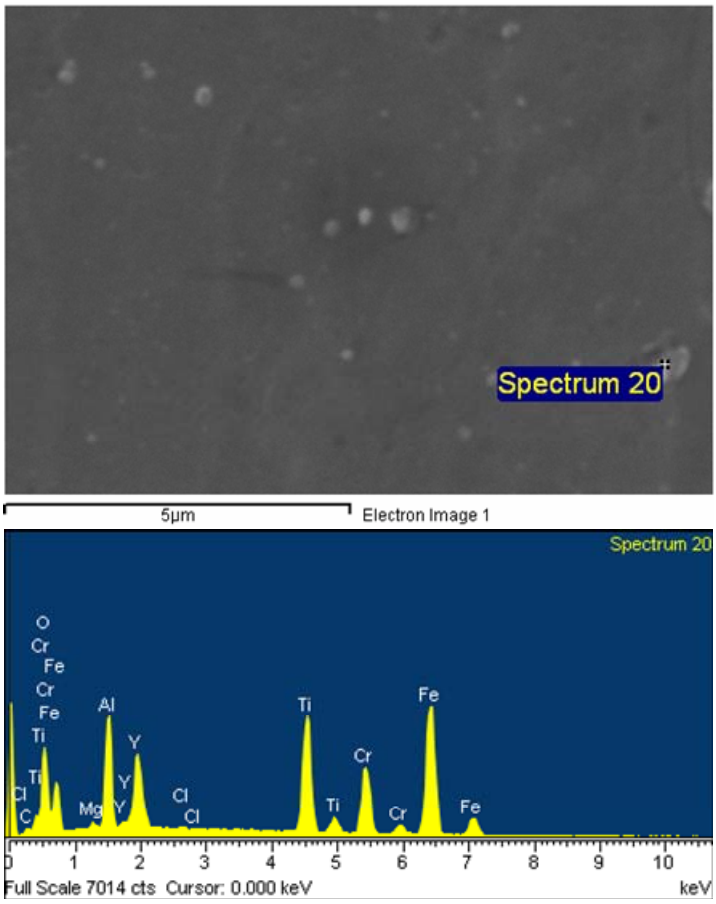

Figure 57. SEM Semi-quantitative Chemistry Analysis of Inertia Weld of Aluminum / Titanium Particulate

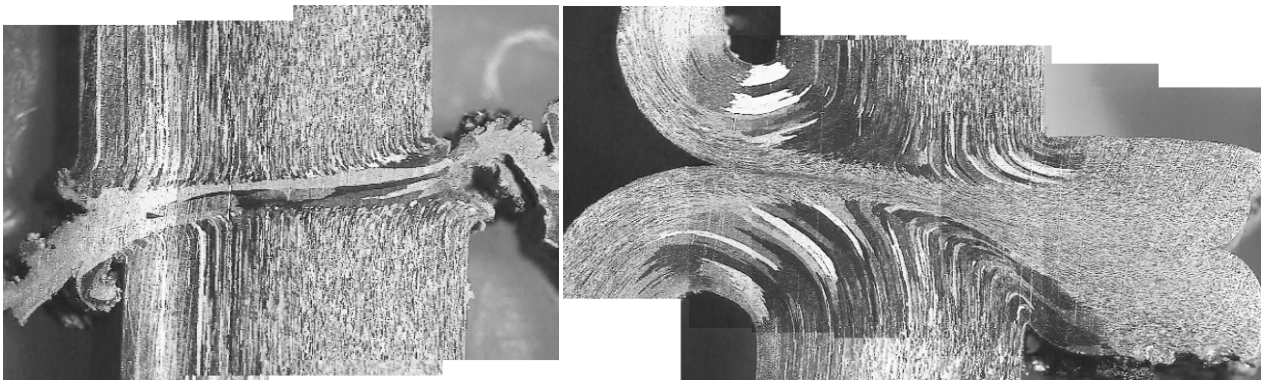

Figure 58. Optical Micrograph of Inertia Welded (left) and , Flash Upset Welded (right) on Recrystallized MA956 alloy

The significant difference in the joint section microstructure prompted the need to quickly ascertain the merit of each technique from the mechanical and creep performance perspective. Samples for mechanical testing were spark machined from the recrystallized coupons.

Figure 59 shows the procedure of extracting tensile/creep specimens with the joint interface in the middle of the gage length. The entire 6mm wall thickness was cut out and additional samples of about 1mm thickness each were sliced from these initial coupons. An initial set of results for creep tests at 850°C range are presented in Table 12. A baseline hoop creep test for the as-received MA956 tube (see Table 5) is also reproduced for easy reference.

Figure 59. Tensile/Creep Specimens Cut from MA956 Joints

Table 12. Screening Tensile tests of Non-Recrystallized MA956 to MA956 Tested at 982°C (1800°F) with Strain Rate of .127mm/min (0.005-in / min)

Metcut Test Number	Specimen Identification	U.T.S. MPa (ksi)	0.2% Y.S. MPa (ksi)	Elong. (%)(a)	RA (%)
T-158250	BASE-1	108.2 (15.7)	94.5 (13.7)	8.5	15
T-158251	BASE-2	108.9 (15.8)	92.4 (13.4)	8.5	24
T-158252	BASE-3	106.2 (15.4)	88.9 (12.9)	8	23
T-158253	FBW 12-1	38.6 (5.6)	19.3 (2.8)	(b)	38
T-158254	FBW 12-2	28.3 (4.1)	22.1 (3.2)	(c)	29
T-158255	FBW 12-3	29.0 (4.2)	21.4 (3.1)	5.0	25
T-158256	FBW 13-1	28.3 (4.1)	19.3 (2.8)	(c)	28
T-158257	FBW 13-2	29.0 (4.2)	19.3 (2.8)	(c)	27
T-158258	FBW 13-3	29.0 (4.2)	21.4 (3.1)	(c)	29
T-158259 non Rx mat'l	IFW 8-1	35.9 (5.2)	31.7 (4.6)	(c)	20
T-158260 non Rx mat'l	IFW 8-2	34.5 (5.0)	31.0 (4.5)	2.3	23
T-158261 non Rx mat'l	IFW 8-3	34.5 (5.0)	31.0 (4.5)	2.7	26
T-158262 Rx mat'l	IFW 9-1	39.3 (5.7)	37.9 (5.5)	3.6	12
T-158263 Rx mat'l	IFW 9-2	37.9 (5.5)	37.9 (5.5)	(c)	19
T-158264 Rx mat'l	IFW 9-3	37.9 (5.5)	37.2 (5.4)	(c)	17

Mechanical Testing of IFW and FBW Weld Joints:

Screening Evaluation As-Welded Condition. Mechanical screening tests upon weld joints that were processed with IFW and FBW processes. Previously conducted high temperature

tests 983°C (1800°F) of post weld non-recrystallized MA956 joints were examined to determine if any notable features could be identified. Review of the test data showed that the inertia friction welds which produced the highest high temperature strengths failed in the bondline region with welds produced from recrystallized material. Table 12 shows the results of these tests. This possibly supports the idea that the grain orientation in the high temperature tests is critical as suggested in literature.

The flash butt welds failed at lower stress levels and produced lower yield strengths. However, it was noted that the failures occurred in the heat affected zones and not on the bondline of the flash butt welds. There were two areas of necking observed in the failed samples on each side of the bondline as shown in Figure 60. Failure location appears to coincide with the location of maximum grain orientation change and growth in the as welded cross sections shown in previous activity summaries. These results again suggest that the orientation of the grains in the weld and heat affected zone are critical as the flash butt welds showed the greatest degree of grain direction change in the heat affected zone. This feature is most likely driven by the fact that in an inertia friction weld, the area of grain direction change undergoes some straining via the torsional stress applied during the friction welding process resulting in an increased level of cold work in this area of grain direction change. The flash butt weld heat affected zone is simply upset with material being forged out of the joint.

Figure 60. Failure of Samples Produced using Flash Butt Welding showing Necking in HAZ Regions

The other notable observation is that the Inertia welds produced with recrystallized material appeared to have slightly higher strength than the weld joint produced form non-recrystallized material.

Screening Evaluation Post Weld Recrystallization. Based on the observations and discussions with team partners, a second group of welded joints were produced from non-recrystallized MA956 using both Inertia Friction welding and Flash Butt Welding. However, after welding, these samples were given the recommended recrystallization heat treatment of 1375°C (2507°F) for one hour to determine if there was an effect of post weld recrystallization on the joint strength at 983°C (1800°F). Figure 61 show a cross section of the weld joint produce using Inertia Friction welding after the recrystallization treatment. Figure 62 shows the results of the post weld recrystallization treatment on the welds produced using flash butt welding. The data from these tests is shown in Table 13. The joints were subjected to the same high temperature testing conditions, 983°C (1800°F). There was a notable improvement in the properties of the joint when post weld recrystallization was completed after welding as compared to previously tested non-recrystallized material that was not recrystallized after welding.

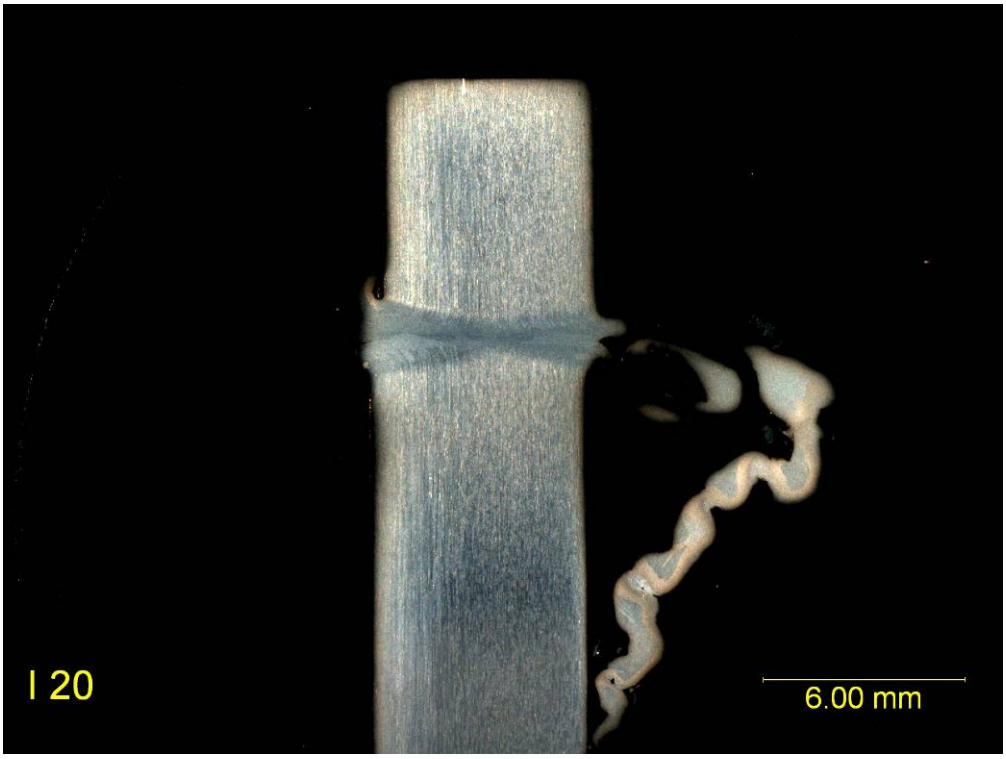

Figure 61. Post Weld Recrystallized Inertia Friction Welded Non Recrystallized MA956 Joint

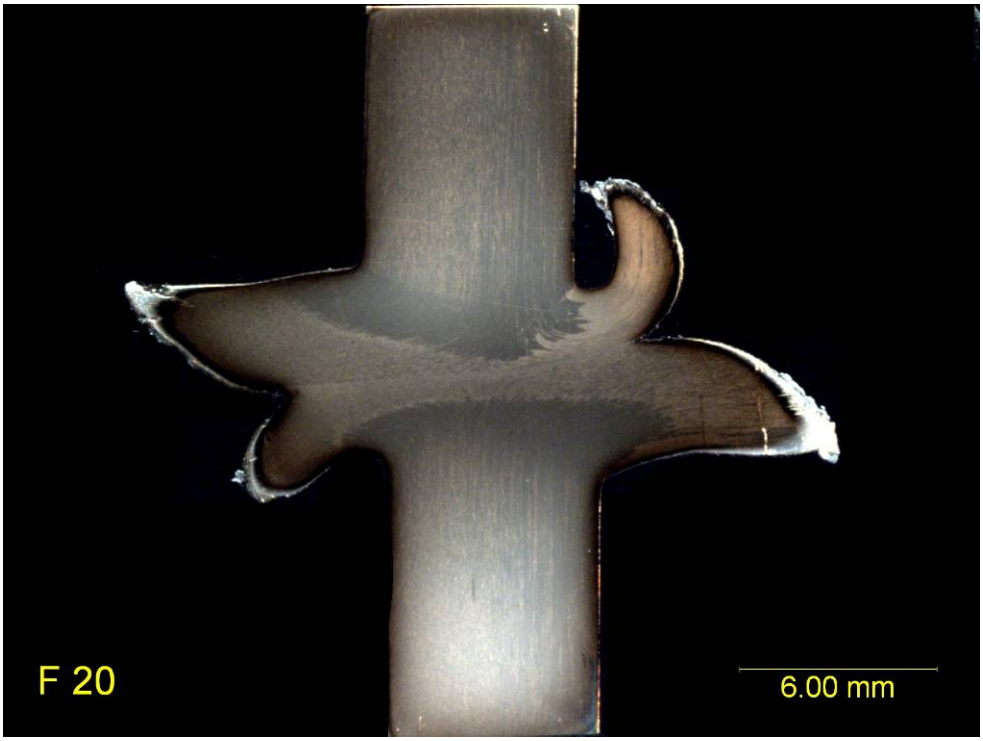

Figure 62. Post Weld Recrystallized Flash Butt Welded Non Recrystallized MA956 Joint

Table 13. Tensile Tests of Non-Recrystallized and Recrystallized MA956 to MA956 Tested at 982°C (1800°F) with Strain Rate of 0.127mm (0.005-in.)/min

Sample	UTS (ksi)	Y.S. (ksi)	Elong. %	RA (%)	Sample	UTS (ksi)	Y.S. (ksi)	Elong. %	RA (%)
FBW 1 *(Rx -2507 deg F)*	6.4	6.4	1	7	IFW 1 *(Rx -2507 deg F)*	9.7	8.4	*	0.7
FBW 2 *(Rx -2507 deg F)*	6.6	6.6	1.5	7.5	IFW 2 *(Rx -2507 deg F)*	9.7	8.2	*	0.1
FBW 3 *(Rx -2507 deg F)*	6.5	6.5	2	1.9	IFW 3 *(Rx -2507 deg F)*	9.7	8.8	*	0.1
Avg	**6.5**	**6.5**	**1.5**	**5.5**	**Avg**	**9.7**	**8.5**	**---**	**0.3**
FBW 1 *(As- Welded)*	5.6	2.8	(b)	38	IFW 1 *(As- Welded)*	5.2	4.6	(c)	20
FBW 2 *(As- Welded)*	4.1	3.2	(c)	29	IFW 2 *(As- Welded)*	5	4.5	2.3	23
FBW 3 *(As- Welded)*	4.2	3.1	5	25	IFW 3 *(As- Welded)*	5	4.5	2.7	26
FBW 4 *(As- Welded)*	4.1	2.8	(c)	28	IFW 4 (d) *(As- Welded)*	5.7	5.5	3.6	12
FBW 5 *(As- Welded)*	4.2	2.8	(c)	27	IFW 5 (d) *(As- Welded)*	5.5	5.5	(c)	19
FBW 6 *(As- Welded)*	4.2	3.1	(c)	29	IFW 6 (d) *(As- Welded)*	5.5	5.4	(c)	17
Avg	**4.4**	**3.0**	**---**	**29.3**	**Avg**	**5.3**	**5.0**	**---**	**19.5**

NOTES:
(a) Value reported is an approximation based on crosshead displacement.
(b) Value based on overall length measurements.
(c) Unable to measure due to fracture surface.
(d) Material in Rx condition prior to welding

The final step in quantifying the strength of the welds was to test the joints at several other test temperatures. Table 14 summarizes the results of these tests. These welds were produced using the optimal conditions developed in this project and the weld joints were recrystallized after welding as this was shown to substantially increase the weld joint strength. In the testing, the Inertia friction welds produced the highest loads to failure with the Flash Butt welds showing slightly lower strength. The dissimilar combination Inconel 601 to MA956 was tested only at 871°C (1600°F) as this is approaching the alloys maximum operating temperature, however the weld strengths were still quite high at this temperature.

Table 14. Final High Temperature Test Results at Various Temperatures

Data Summary						
Metcut Test No.	**Specimen Identification**	**Temp °C (°F)**	**U.T.S. MPa (ksi)**	**0.2%YS MPa (ksi)**	**Elong. (%)**	**RA (%)**
T-170148	FBW-1	871 (1600)	80.0 (11.6)	77.9 (11.3)	2.4	2.1
T-170149	FBW-2	871 (1600)	87.6 (12.7)	86.9 (12.6)	(b)	1.7
T-170150	FBW-3	871 (1600)	84.1 (12.2)	82.7 (12.0)	(b)	3.5
T-170151	IFW-7	871 (1600)	91.7 (13.3)	91.7 (13.3)	(b)	3.0
T-170152	IFW-8	871 (1600)	93.1 (13.5)	90.3 (13.1)	1.9	0.5
T-170153	IFW-9	871 (1600)	93.8 (13.6)	91.7 (13.3)	(b)	1.7
T-170154	IFW MA956 to IN601	871 (1600)	108.2 (15.7)	104.8 (15.2)	1.0	3.0
T-170155	IFW MA956 to IN601	871 (1600)	111.0 (16.1)	107.6 (15.6)	0.9	2.5
T-170156	IFW MA956 to IN601	871 (1600)	113.8 (16.5)	112.4 (16.3)	(b)	1.9
T-170157	FBW-4	1093 (2000)	26.9 (3.9)	26.9 (3.9)(c)	(b)	0
T-170158	FBW-5	1093 (2000)	27.6 (4.0)	26.9 (3.9)(c)	(b)	0
T-170159	FBW-6	1093 (2000)	33.8 (4.9)	(d)	(b)	0
T-170160	IFW-10	1093 (2000)	44.8 (6.5)	39.3 (5.7)(c)	(b)	0
T-170161	IFW-11	1093 (2000)	42.1 (6.1)	37.2 (5.4)(c)	(b)	0
T-170162	IFW-12	1093 (2000)	40.0 (5.8)	34.5 (5.0)(c)	(b)	0

Notes: (a) Value based on overall length measurements.
(b) Unable to measure due to fracture surface
(c) Value reported is an approximation based on crosshead displacement.
(d) Specimen failed before 0.2% offset yield was obtained.

Creep Testing: The geometrical considerations for creep testing of joints were an important issue as illustrated here. The baseline hoop creep data was extracted from 63.5mm (2.5-inch) O.D. tubes that were subsequently flattened and samples cut in the transverse orientation. However, for the joint sections, transverse samples are not feasible as the processed joint width is considerably narrower than the 3.18mm (0.125-inch) specimen width and any sample cross-section will contain the base material as well. The issue was further exacerbated as the tube joint needed to be flattened to extract the transverse specimen. Thus, an alternate strategy of

extracting longitudinal specimens (see Figure 60) was employed to ensure that the joint section was comprised of the entire gage cross-section. It should be noted that the sample orientation was a particular issue in MA956 tubes on account of the grain shape anisotropy where grains are extended along the longitudinal direction. Prior work at UCSD on non-fusion joints revealed that the recrystallized grain microstructure in the joint region was fairly isotropic (Figure 63), and the particular orientation of the volume of material comprising the joint region during testing was not critical. Therefore, the joint creep performance could be evaluated in the longitudinal sample geometry.. The outcome of this geometry was that the base material in the gage length was loaded elastically, and the bulk of the creep occurred in the small volume of the joint region in the gage length.

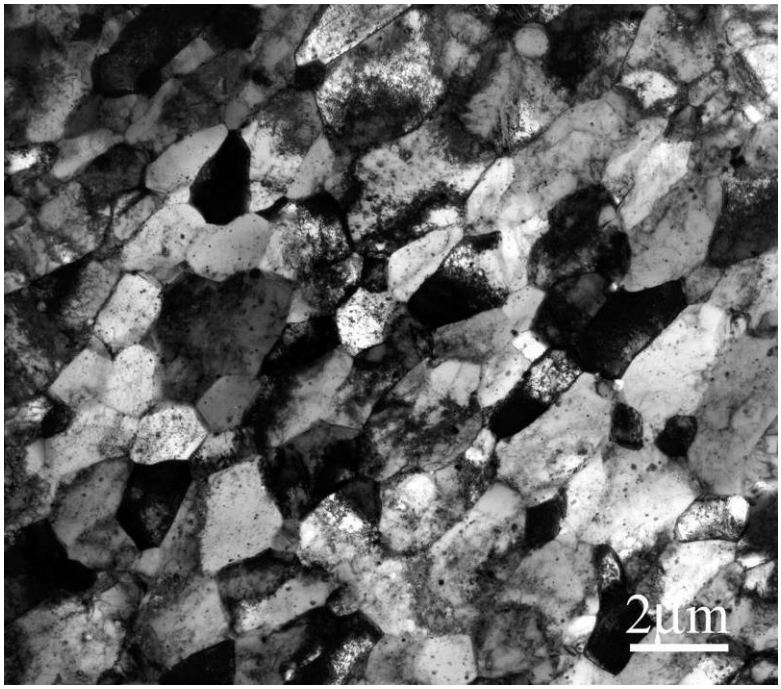

Figure 63. TEM Micrograph of Recrystallized Inertia-welded MA956 Joint
Note: The isotropic grain structure precludes any orientation specific effects.

Table 15 shows the flash upset and inertia welded joint performance tested at 13.8 MPa (2 ksi) stress in the 850-1000°C (1562-1832°F) temperature range. Both joints performed well with little loss in creep performance. The inertia-welded joint was superior to the flash-upset joint and performed better than the baseline MA956 hoop-creep results. (*Note: The actual creep strain rates were underestimated as they were normalized over the entire gage length rather than the actual joint length over which creep actually occurred).* Multiple creep tests (Tests # 3-9 in Table 15) for inertia-welded joints detailed the spectrum of performance over the anticipated 850-1000°C (1562-1832°F) temperature range. The nominal creep strain rate/day increased from a low value of 1.0e-4 at 850°C (1562°F) to the upper range value of 9.0e-4 at 975°C (1787°F). The L-M parameter exhibited a maxima at 925-950°C (1697-1742°F) with the value falling slightly as the temperature was raised further, consistent with the observation made for the flow formed material found in Section 5.5.2.

Within the context of creep performance, some comparisons between the flash upset and inertia welded samples are elucidated here. Looking back to the microstructure of the joints in Figure 58 (a),(b) note the significantly larger heat affected zone (HAZ) in the flash-upset joint.

This enlarged HAZ in flash-upset weld (Test #2) was responsible for the accelerated creep strain rate/day observed in such tests. F or example, observed in Test #2 is a strain rate of 6.0e-4 at 850°C (1562°F) while such a high creep rate is observed in inertia-welded samples in the 950-975°C (1742-1787°F) temperature range (see Test #5 and 6 in Table 15).

Table 15. Creep Testing of Non-Fusion Joints in MA956 Tube Materials

Test #	MA956 Joint Processing and HT	Temp °C (°F)	Stress, MPa (ksi)	Life (hrs)	L-M Parameter	Strain Rate/Day
1	MA956, As-received, 1375oC (2507°F), 12hr, Air	900 (1652)	13.8 (2)		45.00	
2	EWI Flash Upset, HT:1375oC (2507°F), 12hr, Air	850 (1562)	13.8 (2)	144	44.80	6.0e-4
3	EWI Inertia Weld, HT 1375oC (2507°F), 12hr, Air	850 (1562)	13.8 (2)	2196	47.20	1.0e-4
4	EWI Inertia Weld, HT 1375oC (2507°F), 12hr, Air	900 (1652)	13.8 (2)	390	47.71	2.0e-4
5	EWI Inertia Weld, HT 1375oC (2507°F), 12hr, Air	950 (1742)	13.8 (2)	102.6	48.47	4.0e-4
6	EWI Inertia Weld, HT 1375oC (2507°F), 12hr, Air	975 (1787)	13.8 (2)	19	47.81	9.0e-4
7	EWI Inertia Weld, HT 1375oC (2507°F), 12hr, Air	975 (1787)	13.8 (2)	25	48.08	4.6e-4
8	EWI Inertia Weld, HT 1375oC (2507°F), 12hr, Air	925 (1697)	13.8 (2)	478	48.92	2.4e-4
9	EWI Inertia Weld, HT 1375oC (2507°F), 12hr, Air	900 (1652)	13.8 (2)	1021*****	48.59*	1.4e-4

***** *Test #9 terminated by vibration accident and result not indicative of true L-M response.*

5.4 Task 4. Bending of MA956 Tubes

The primary goal of this task was to evaluate the effect, if any, of bending-induced strain on the microstructure of MA956 tubing materials; i.e., to determine if strain induced recrystallization occurred. In addition, the forming capabilities of the materials, or lack thereof, were to be ascertained/evaluated during the bending process.

In this task bends of various radii were made in MA956 tubes that had been supplied in two different conditions:

- cold drawn condition – which was also designated as material that had not undergone a commercial recrystallization treatment.
- commercially annealed condition – which is cold drawn material that had undergone a recrystallization treatment (e.g., 1293.3°C (2360°F) for six hours).

The bend radii were selected to yield maximum outer fiber strain levels 5, 10, 15, 20 and 25 percent. Since two bends were needed for each material condition at each strain level, a total of 20 bends were required.

One bend of each material condition and each strain level was characterized with regard to microstructure and hardness in the as-bent condition, whereas, the second bend was subjected to a thermal exposure of 1204.4°C (2200°F) for 100 hours before it was similarly characterized.

By comparing the bends the effect of the bending-induced strain on recrystallization caused by thermal exposure was evaluated. In addition to evaluating the recrystallization tendency of the material, a dimensional analysis was performed on cross sections from the center of the bends to provide some basic information on the formability of the material.

5.4.1 Initial Material Characterization

Straight lengths of MA956 tubing were supplied in the cold drawn (CD) and commercially annealed (CA) conditions. A dimensional survey of the tubes revealed the outside diameter varied from 62.7 to 63.75 mm (2.508 to 2.510 in.). and the wall thickness ranged from 6.27 to 6.55 mm (0.247 to 0.258 in.). The microstructure and hardness in sections removed from tubes in each supplied condition were also evaluated. Figure 64 illustrates the macrostructure of the CA and CD tubes in both transverse- and longitudinally-oriented sections, while the microstructures are displayed in Figure 65 (cold-drawn) and Figure 66 (commercially annealed). It is evident from a comparison of the structures that the commercially annealed material has a significantly coarser grain structure than the cold drawn material. The anisotropy of the structure in both conditions is also apparent when comparing the microstructure of the transverse sections to the longitudinally oriented sections. Hardness measurements indicated a value of 35 HRC (327 BHN) for the cold drawn material and 25 HRC (253 BHN) for the commercially annealed material.

Since bending of the tubes was required to study the recrystallization behavior, an assessment of the material ductility was necessary. The assessment was made, in a rudimentary way, by performing flattening tests on approximately 9.53 mm (3/8 in.). wide transverse cross sections. In tests performed at ambient temperature (e.g., 25°C (77°F), the cold drawn material cracked immediately upon loading, while the commercially annealed material flattened 38 percent before cracking. Tests performed at 204.4°C (400°F) again revealed no ductility in the cold drawn material and the commercially annealed material continued to show higher ductility by flattening to 54 percent before cracking.

Because the cold drawn material exhibited essentially no ductility at temperatures up to 204.4°C (400°F), the viability of bending tubes in this condition was seriously doubted. After consulting with Special Metals Corporation, a series of laboratory tests were performed whereby sections of the cold drawn material were heated to temperatures ranging from 926.6 to 1176.6°C (1700°F to 2150°F) for 1 or 24 hours in an attempt to improve the ductility of the material. After the heat treatments were performed, the microstructure, hardness, and flattening capability of the sections were evaluated. The heat treatment parameters and the results of the hardness and flattening tests are reported in Table 16, while selected photomacrographs of the macrostructure are shown in Figure 67. The results of the flattening tests indicated a dramatic improvement in ductility of the cold drawn material for heat treatment temperatures ranging from 1037.7°C to 1176.6°C (1900°F and 2150°F) at a time of one hour. As shown in Figure 67, the heat treatments at 1037.7°C, 1093.3°C and 1176.61093.3°C (1900°F, 2000°F, and 2150°F) successively increased the grain size of the material, approaching that which was noted in the commercially annealed material. In addition, the hardness survey indicated the hardness of the material decreased with increasing heat treatment temperature, dropping from 35 HRC in the original cold drawn material to 22-25 HRC in the section heat treated at 1176.6°C (2150°F).

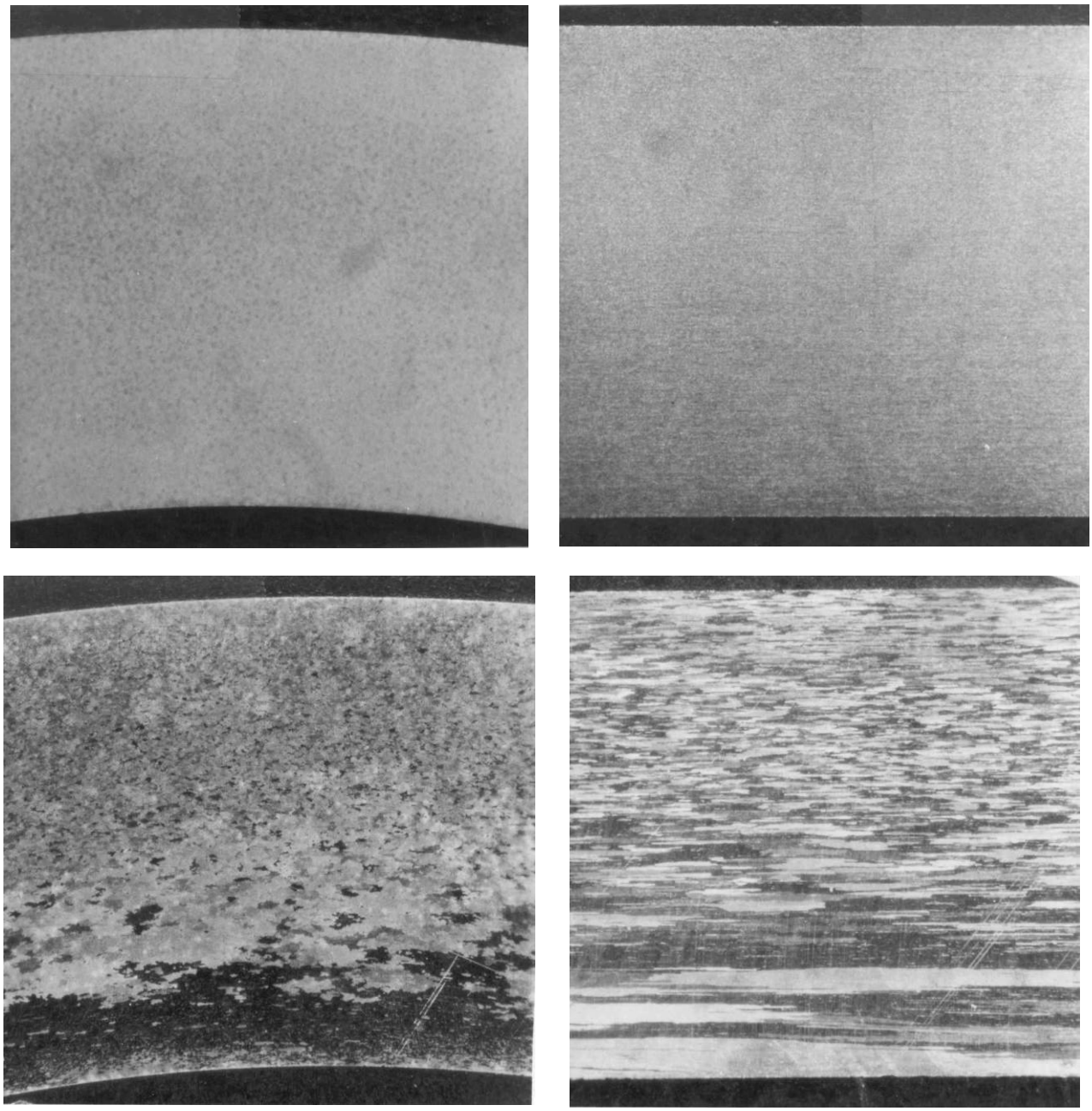

Photomacrographs 12× Magnification Etched

Figure 64. Macrostructure of Cold-drawn (top) and Commercially-annealed (bottom) Tubes Illustrated in Circumferential (left photomacrograph) and Longitudinal (right photomacrograph) Sections
Note: The structure of the commercially-annealed material has a significantly coarser grain size than the cold-drawn material.

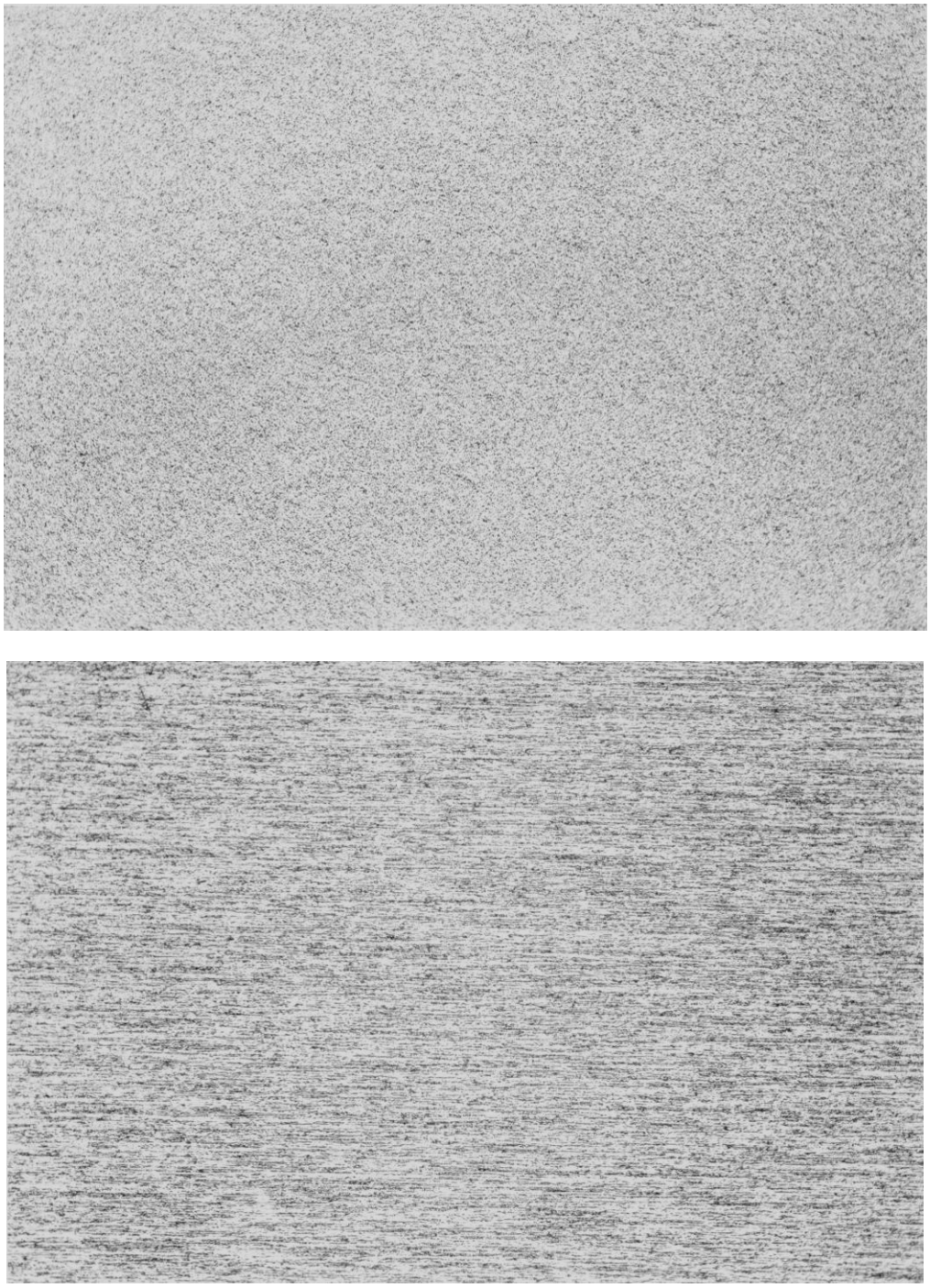

Photomicrographs 100× Magnification Etched

Figure 65. Microstructure of Cold-drawn Tube shown in Circumferential (top) and Longitudinal (bottom) Sections
Note: Anisotropy of the structure is evident.

Photomicrographs 100× Magnification Etched

Figure 66. Microstructure of Commercially-annealed Tube Displayed in Circumferential (top) **and Longitudinal** (bottom) **Sections**
Note: The anisotropy of the structure is evident.

Table 16. Parameters and Test Results

Condition	Annealing Parameters				Flattening Results (%)	
	Temperature (°F)	Temperature (°C)	Time (Hrs.)	Hardness (HRC)	Ambient	204.4°C (400°F)
CD	NA	NA	NA	35	0	0
CD / ANN [1]	2360	1293.3	6	25	37.6	54
CD / ANN [2]	1700	926.6	1	26-28	5.9	6.5
CD / ANN [2]	1700	926.6	24	26.28	4.4	8.2
CD / ANN [2]	1800	982.2	1	26-28	4	5.3
CD / ANN [2]	1800	982.2	24	25	6.2	9
CD / ANN [2]	1900	1037.7	1	27-29	——	40
CD / ANN [2]	2000	1093.3	1	26-27	——	52
CD / ANN [2]	2150	1176.6	1	22.25	——	62.8

CD – *Cold drawn* / ANN – *Annealed*

[1] *Annealed by Special Metals Corp.*

[2] *Annealed at FWDC*

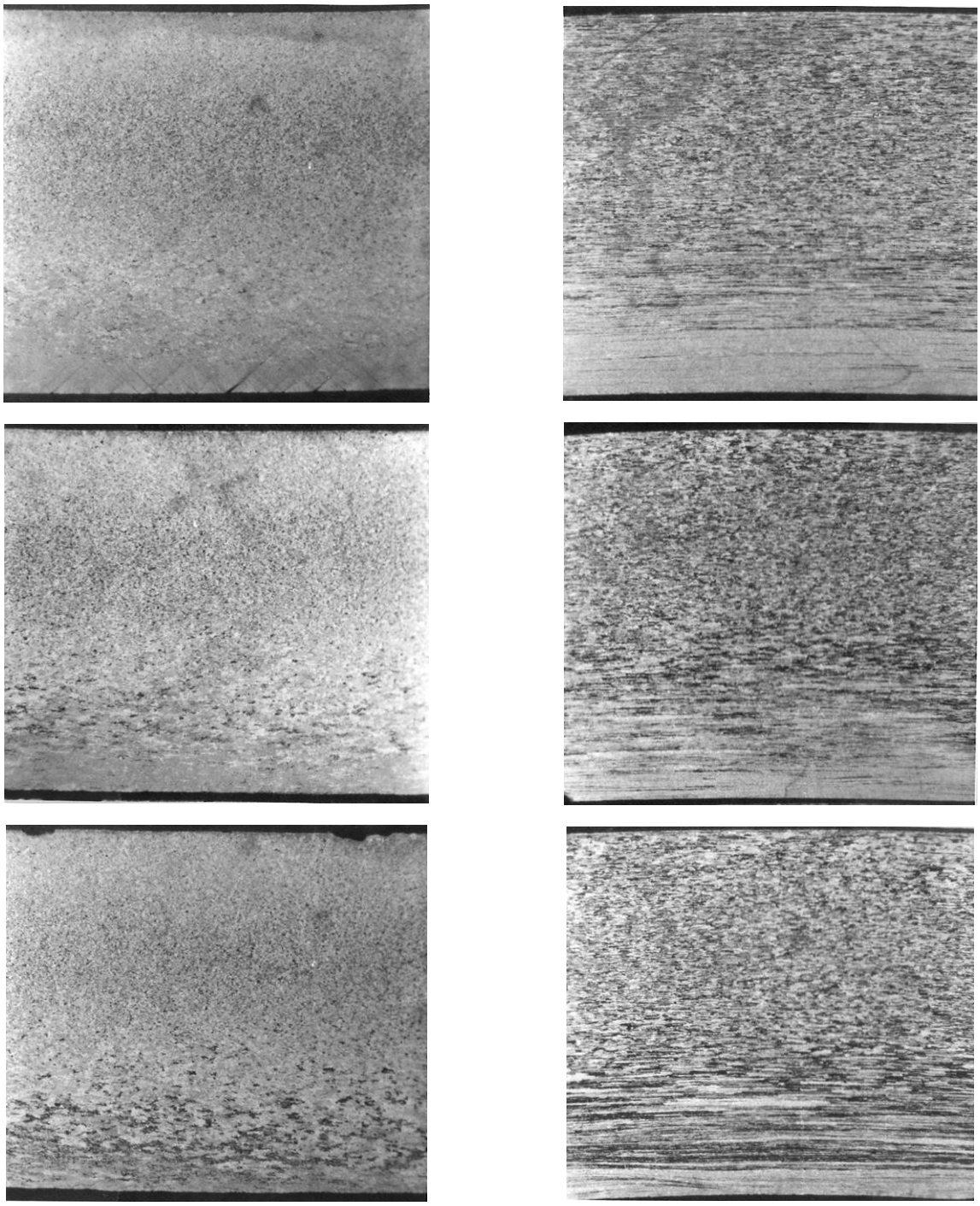

Photomacrographs 12× Magnification Etched

Figure 67. Macrostructure of Cold-drawn Material Illustrated in Circumferential (left) and Longitudinal (right) Sections after Annealing Treatments of 1037.7°C (1900°F) (top), 1093.3°C (2000°F) (middle), and 1176.6°C (2150°F) (bottom) for One Hour
Note: The grain size increased with increasing temperature.

Based on the results of the heat treatment study, the four lengths of cold drawn tubing material available to the program were subjected to a thermal treatment of 1121.1°C ± 14°C (2050°F ± 25°F) for one hour and were thereafter referred to as modified annealed (MA) material. Subsequent to the thermal treatment, samples of each length were evaluated for microstructure and hardness. As shown in Figure 68 and Figure 69, the results of the evaluation were consistent with the heat treatment study, e.g. the heat treated material developed a coarser grain size with a decrease in hardness compared to the original cold drawn material. In comparing the microstructures of the MA tubing, it is evident that not all four developed a similar grain size. Two of the lengths exhibited a similar grain size (Figure 68), while the third had a slightly coarser grain size (Figure 69 top), and the fourth even coarser yet (Figure 69 bottom).

5.4.2 Fabrication of Bends

Tube lengths of both the commercially annealed and modified annealed material were released for bending. Calculations indicated that the released 2.5 in. OD tubing would require bend radii of 635, 317.5, 211.58, 158.75 and 127 mm (25, 12.5, 8.33, 6.25, and 5 in.) to produce maximum outer fiber strain levels of 5, 10, 15, 20, and 25 percent respectively. Since those specific radius-size dye wheels were not all available to the program, those closest to the desired values were used, e.g., 304.8 , 190.5, 152.4, 127 and 107.95 mm (12, 7.5, 6, 5, and 4.25 in.) and resulted in the size bends and strain values shown in Table 17:

Table 17. Bends and Strain Values

Bend Radius (mm)	Bend Radius (in)	Bend Size	Outer Fiber Strain (%)
304.8	12	4.8D	10.4
190.5	7.5	3D	16.6
152.4	6	2.4D	20.8
127	5	2D	25
107.95	4.25	1.7D	29.4

Four of the five bend radii produced outer fiber strains that were close to their desired values. The fifth bend, which used a 107.95 mm (4.25 in.) rather than a 635 mm (25 in.) bend radius bend, resulted in 29.4 percent rather than 25 percent outer fiber strain. The 107.95 mm (4.25 in.) bend radius was used because:

- The 635 mm (25 in.) radius bend would have consumed a large amount of material (which was limited in quantity).
- The 107.95 mm (4.25 in.) radius bend is a more severe bend and would test the material from both its recrystallization tendency and forming capability.

The 304.8, 190.5 and 152.4 mm (12, 7.5, and 6 in.) radii bends were made on a Pines bender, whereas the tighter radius bends – the 127 mm (5 in.) and 107.95 mm (4.25 in.) ones – were made on a Schwarze-Wirtz bender, which applies a push-up load on the trailing leg to minimize wall thinning at the extrados. All bends were made to an approximately 175 degree angle. Since the flattening tests performed during the initial characterization study of the material indicated an increase in ductility at 204.4°C (400°F) versus ambient temperature, the tubing was warmed to 400°F prior to bending.

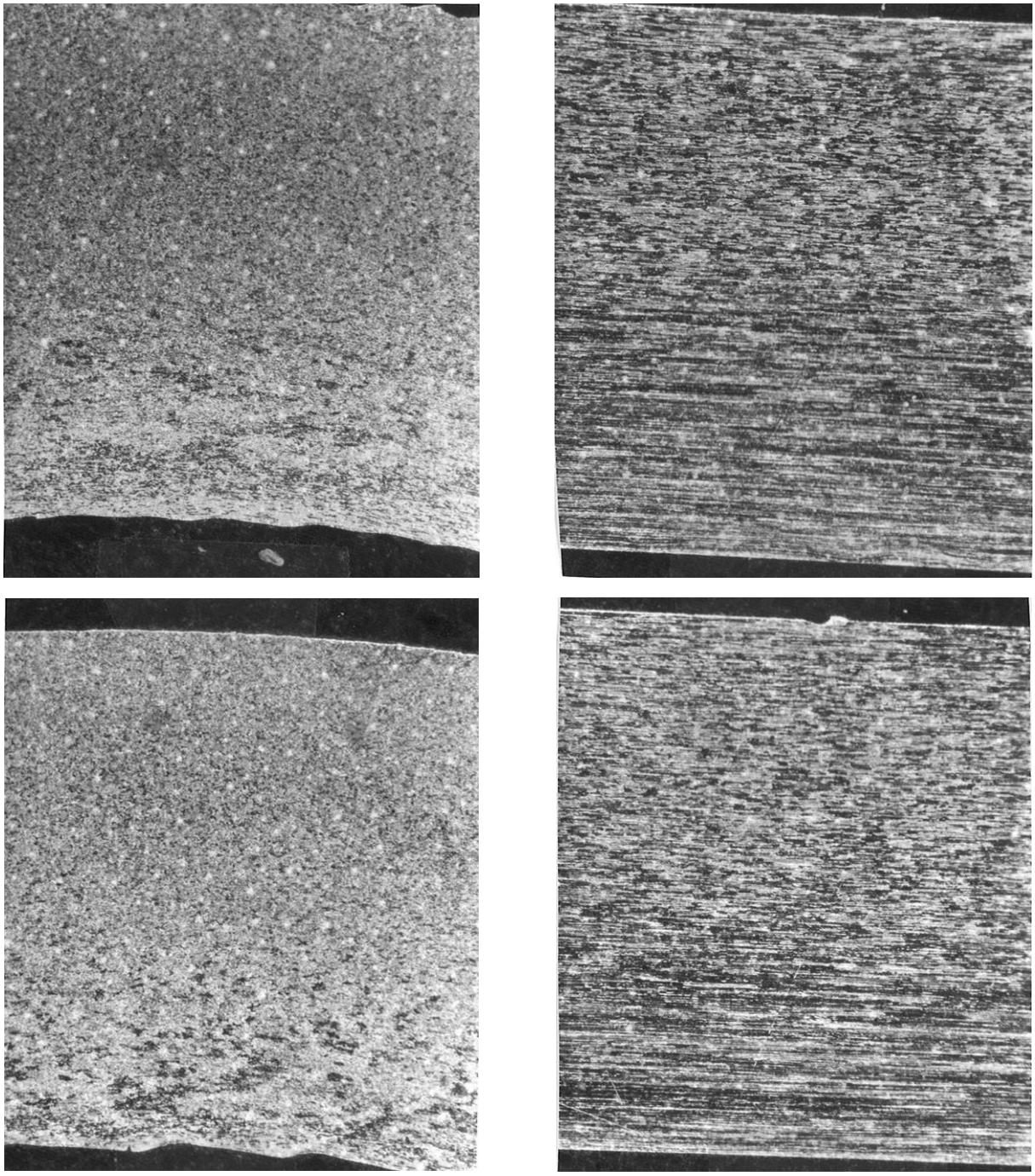

Photomacrographs 16× Magnification Etched

Figure 68. Macrostructure of Two Lengths of Cold-drawn Material Annealed at 1121.1°C (2050°F) for One Hour Displayed in Circumferential (left) and Longitudinal (right) Sections
Note: The grain size in the two was similar.

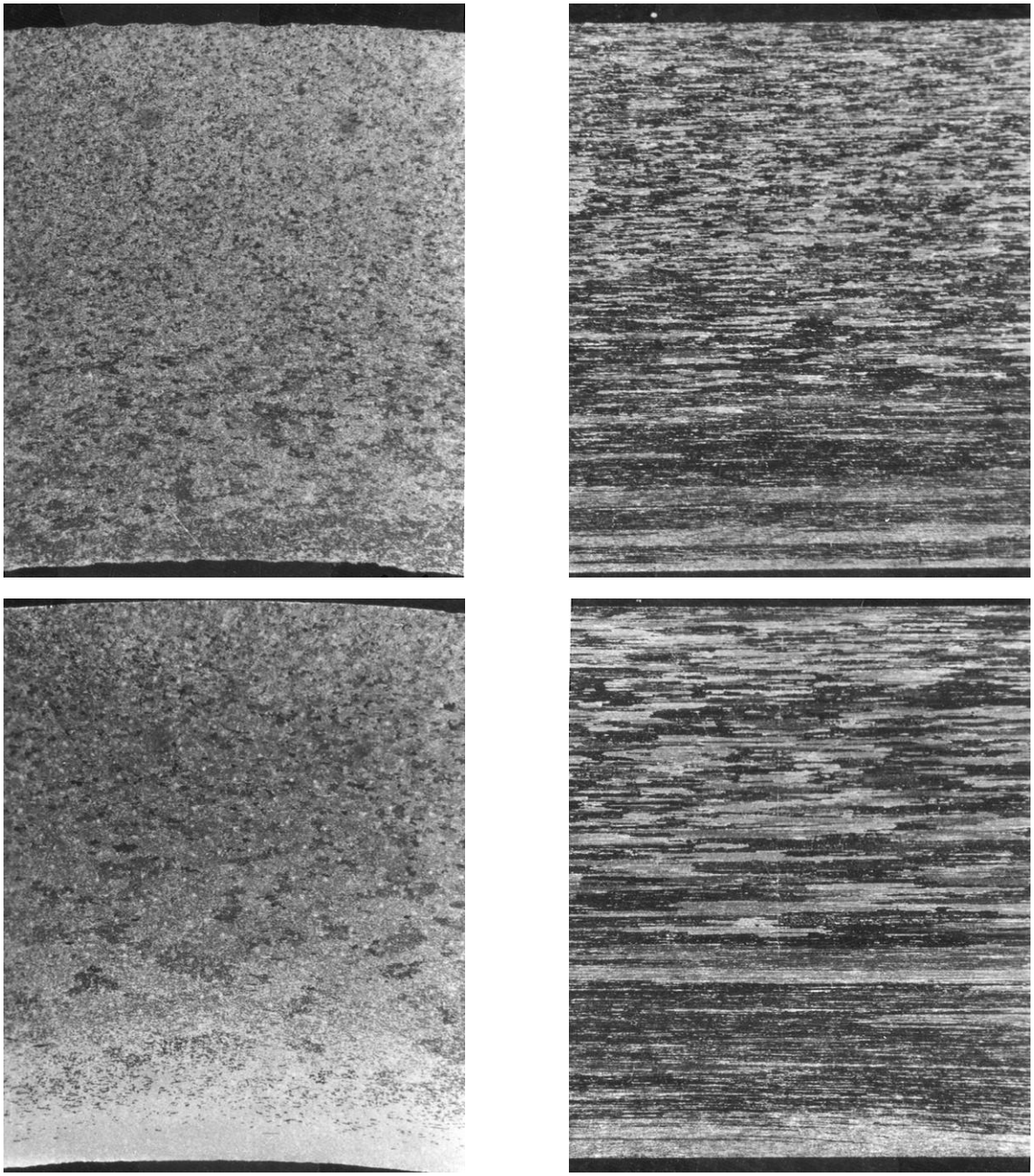

Photomacrographs 16× Magnification Etched

Figure 69. Macrostructure of Other Two Lengths of Cold-drawn Material Annealed at 1121.1°C (2050°F) for One Hour shown in Circumferential (left) and Longitudinal (right) Sections

Note: The grain sizes were coarser than that in the two lengths illustrated in Figure 68. Of these two, the grain size in the length represented by the bottom photomacrographs was slightly coarser than that represented by the top photomacrographs.

The 304.8, 190.5 and 152.4 mm (12, 7.5, and 6 in.) radii bends (using the Pines bender) were made first. Two bends of each of the differently annealed materials were made at each bend radius without any problems. The representative appearance of the bends is illustrated in Figure 70 through Figure 72.

Photomacrograph × Magnification As-bent

Figure 70. Appearance of 304.8 mm (12-in.) Radius (4.8D) Bend Displayed

Photomacrograph × Magnification As-bent

Figure 71. Appearance of 190.5 mm (7.5-in.) Radius (3D) Bend Shown

Photomacrograph × Magnification As-bent

Figure 72. Appearance of 152.4 mm (6-in.) Radius (2.4D) Bend Illustrated

When the required number of bends was completed, an attempt was made to make a 6 in. radius bend without first heating the tube to 204.4°C (400°F). In this trial, the bend failed circumferentially in a brittle manner at a bend angle of approximately 135 degrees. A second attempt was tried, and the bend failed circumferentially at an angle of approximately 90 degrees. Thus, their failures validated the decision to heat the tubing to 204.4°C (400°F) prior to bending.

With regard to the 127 mm (5 in.) radius bends, the first attempt was made (on the Schwarze-Wirtz bender) using the modified annealed material. The tube failed circumferentially shortly after the bending process was initiated even though the tube had been heated to 204.4°C (400°F). A switch was made to the commercially annealed material, and the bend was made without problems using the same procedure. After a second bend was successfully made with the commercially annealed material, the process was tried again on the modified annealed material. This second attempt also failed as the tube cracked circumferentially at the onset of the bending process. Before attempting to make another bend with the modified annealed material, a strip approximately 25.4 mm (1 in.) wide, that was subsequently going to coincide with the intrados side of the bend, was heated to a "red-hot" condition. This additional heating was done at the suggestion of a bending machine operator who said it (heat striping) was employed when difficulties were experienced in making bends. With the application of this additional heat, the bend was made without a problem. A second successful bend was made on the modified annealed material with this new procedure and one of the 127 mm (5 in.) radius bends is shown in Figure 73.

The first attempt to make the 107.95 mm (4.25 in.) radius bends was tried on the commercially annealed material after just heating the tube to 204.4°C (400°F). The tube failed circumferentially at the start of the bend. When a narrow strip was heated to a red hot condition on the side of the tube that was to become the intrados of the bend, similar to that done on the modified annealed material for the 127 mm (5 in.) radius bends, the bend was made without a problem. A second bend on the commercially annealed material and two bends on the modified annealed material were made using this procedure. The representative appearance of the 107.95 mm (4.25 in..) radius bends is displayed in Figure 74.

Photomacrograph × Magnification As-bent

Figure 73. Appearance of 127 mm (5-in.) Radius (2D) Bend Presented

Photomacrograph × Magnification As-bent

Figure 74. Appearance of 107.95 mm (4.25-in.) Radius (1.7D) Bend Illustrated

In summary, the 304.8, 190.5 and 152.4 mm (12, 7.5, and 6 in.) radius bends were successfully made on a Pines bending machine after heating the tube to 204.4°C (400°F) prior to bending. Attempts to make a 6 in. radius bend at ambient temperature resulted in brittle circumferential failures in the tubes, thereby validating the need to preheat the tubes prior to bending. The 5 and 107.95 mm (4.25 in.) radius bends were made on a Schwarze-Wirtz bender, but required an additional procedural step which consisted of heating a strip of material (approximately

25.4 mm (1 in.) wide) on what was to become the intrados side of the bend to a red hot condition prior to bending. Although the 127 mm (5 in.) radius bends on the commercially annealed material did not require this additional heating step, it is recommended that it still be performed, since it does not require much time and helps to ensure the fabrication of the bend.

5.4.3 Laboratory Examinations

One bend of each material condition and each strain level was set aside for evaluation in the as-bent condition. The other bend of each material condition and each strain level was subjected to a thermal exposure of 1204°C (2200°F) for 100 hours. The evaluation of the as-bent samples consisted of a dimensional analysis, microstructural characterization, and hardness survey at the center of the bend. The evaluation of the thermally exposed samples consisted of a microstructural characterization and hardness survey at the center of the bend.

5.4.4 Dimensional Analysis

The results of the dimensional analysis are reported in Table 18. The analysis consisted of measuring the maximum and minimum outside diameter and the wall thickness at four locations 90 degrees apart at the center of the bends (on transverse cross sections). The 0 degree location represents the center of the extrados side of the bend, while the 180 degree location is the center of the intrados side.

Using the results of dimensional analysis, the bends were further characterized with regard to percent flattening, percent ovality, percent wall thinning at the extrados, and percent wall thickening at the intrados. The results of this characterization are shown in Table 19. Typical acceptance criteria for flattening and ovality are:

Flattening:	Less than 2.5D Bend Radius $\leq$ 12%
	2.5D Bend Radius and above $\leq$ 10%
Ovality:	$\leq$ 8%

As can be noted from the results in Table 19, the flattening and ovality of all of the bends satisfied the acceptance criteria.

With regard to wall thinning at the extrados, the maximum thinning was 13 percent and it occurred in two of the bends. In these cases, the wall thickness was reduced from 6.43 mm (0.253 in) to 5.58 mm (0.220 in.) Also evident is the fact that the wall thinning at the extrados in the tighter radius bends (e.g. the 127 mm and 107.97 mm (5 and 4.25 in.) radius bends) was comparable to that in the 6 in. radius bends. The lower than expected thinning in the tighter bends is believed, to a large extent, to have been caused by the push-up capability of the Schwarze-Wirtz bender.

The wall thickening percentage at the intrados increased as the bends became tighter, which was expected. The push-up capability of the Schwarze-Wirtz bender did not appear to have an effect on the thickening of the wall on the intrados side of the tight radius bends, however.

5.4.5 Microstructural Examination

The microstructural examination for recrystallization was conducted by evaluating transverse and longitudinally oriented cross sections removed from the extrados and intrados at the center of the bends. The cross sections were evaluated in the polished/ etched condition using both a stereomicroscope and a metallograph. In the evaluation, consideration was given to the fact that the various lengths of material used to make the bends, for both material conditions, did not necessarily possess the same starting grain size. (Recall that starting differences were seen in the modified annealed material in Figure 68 and Figure 69 and in the commercially annealed material; in the latter, one tube had a much coarser grain size than the other four.)

Table 18. Dimensional Survey of Bends (English units)

Bend Radius	Bend Size	Outer Fiber Strain (%)	Material	Outside Diameter (in.)		Wall Thickness (in.)			
				Maximum	Minimum	0	90	180	270
12	4.8D	10.4	CA	2.507	2.485	0.234	0.256	0.271	0.262
12	4.8D	10.4	MA	2.510	2.497	0.239	0.259	0.274	0.262
7.5	3D	16.6	CA	2.540	2.428	0.226	0.256	0.280	0.253
7.5	3D	16.6	MA	2.538	2.423	0.229	0.259	0.277	0.245
6	2.4D	20.8	CA	2.521	2.392	0.220	0.247	0.293	0.247
6	2.4D	20.8	MA	2.523	2.400	0.223	0.257	0.282	0.242
5	2D	25	CA	2.528	2.375	0.225	0.257	0.288	0.251
5	2D	25	MA	2.515	2.400	0.220	0.258	0.318	0.262
4.25	1.7D	29.4	CA	2.520	2.495	0.229	0.263	0.331	0.276
4.25	1.7D	29.4	MA	2.520	2.510	0.233	0.259	0.326	0.263

Table 18. Dimensional Survey of Bends (Metric units) – Continued

Bend Radius (mm)	Bend Size	Outer Fiber Strain (%)	Material	Outside Diameter (mm)		Wall Thickness (mm)			
				Maximum	Minimum	0	90	180	270
304.8	4.8D	10.4	CA	63.67	63.12	5.94	6.50	6.88	6.65
304.8	4.8D	10.4	MA	63.75	63.42	6.07	6.57	6.95	6.65
190.5	3D	16.6	CA	64.51	61.67	5.74	6.50	7.112	6.42
190.5	3D	16.6	MA	64.46	61.54	5.81	6.57	7.03	6.22
152.4	2.4D	20.8	CA	64.03	60.75	5.58	6.27	7.44	6.27
152.4	2.4D	20.8	MA	64.08	60.96	5.664	6.52	7.16	6.14
127	2D	25	CA	64.21	60.32	5.71	6.52	7.31	6.37
127	2D	25	MA	63.88	60.96	5.58	6.55	8.07	6.65
107.95	1.7D	29.4	CA	64.01	63.37	5.81	6.68	8.41	7.01
107.95	1.7D	29.4	MA	64.008	63.754	5.9182	6.5786	8.2804	6.6802

CA – commercially annealed
MA – modified annealed
0 – center of extrados side of bend
180 – center of intrados side of bend

Table 19. Characterization of Bends

Bend Radius (mm)	Bend Radius (in.)	Bend Size	Flattening (%)	Ovality (%)	Thinning at Extrados (%)	Thickening at Intrados (%)
304.8	12	4.8D	1	0.9	7.5	7.1
304.8	12	4.8D	0.5	0.5	5.5	8.3
190.5	7.5	3D	3.2	4.5	10.7	10.7
190.5	7.5	3D	3.4	4.6	9.5	9.5
152.4	6	2.4D	4.6	5.1	13.0	15.8
152.4	6	2.4D	4.3	4.9	11.9	11.4
127	5	2D	5.3	6.1	11.1	13.9
127	5	2D	2.0	2.2	13.0	25.7
107.95	4.25	1.7D	0.6	1	9.5	30.8
107.95	4.25	1.7D	0	0.2	7.9	28.9

Since differences in starting grain sizes could carry over into and lead to misleading recrystallization results, the starting grain sizes of all bent materials were evaluated. It was found that in two cases, (e.g. the 127 mm (5 in.) radius bends in the modified annealed material and the 114.3 mm (4.5 in.) radius bends in the commercially annealed material) different grain size materials were used to make the two bends for that particular bend radius.

Taking into account the grain size difference in the two aforementioned bend pairs, the recrystallization evaluation was performed to determine if there was any grain morphology differences between the as-bent and the thermally-exposed samples for a given bend radius. The results of the evaluation indicated that in no case was a grain size difference or change in grain morphology noted for either the commercially annealed or modified annealed material. Representative photomacrographs/photomicrographs of the microstructure/microstructure illustrating the absence of any notable change in structure between the as-bent and the thermally-treated bends are shown in Figure 4.2.12 through 4.2.23. The figures contain the following:

While there were no notable differences in microstructure between the as-bent and thermally-exposed samples for a given bend radius, there was a subtle difference in microstructure in the bend area compared to the straight leg. The difference was a small reduction in grain size in the bend area, which is probably the result of grain deformation caused by the strain produced from the bending process. The induced strain did result in an increase in hardness as discussed in the following section.

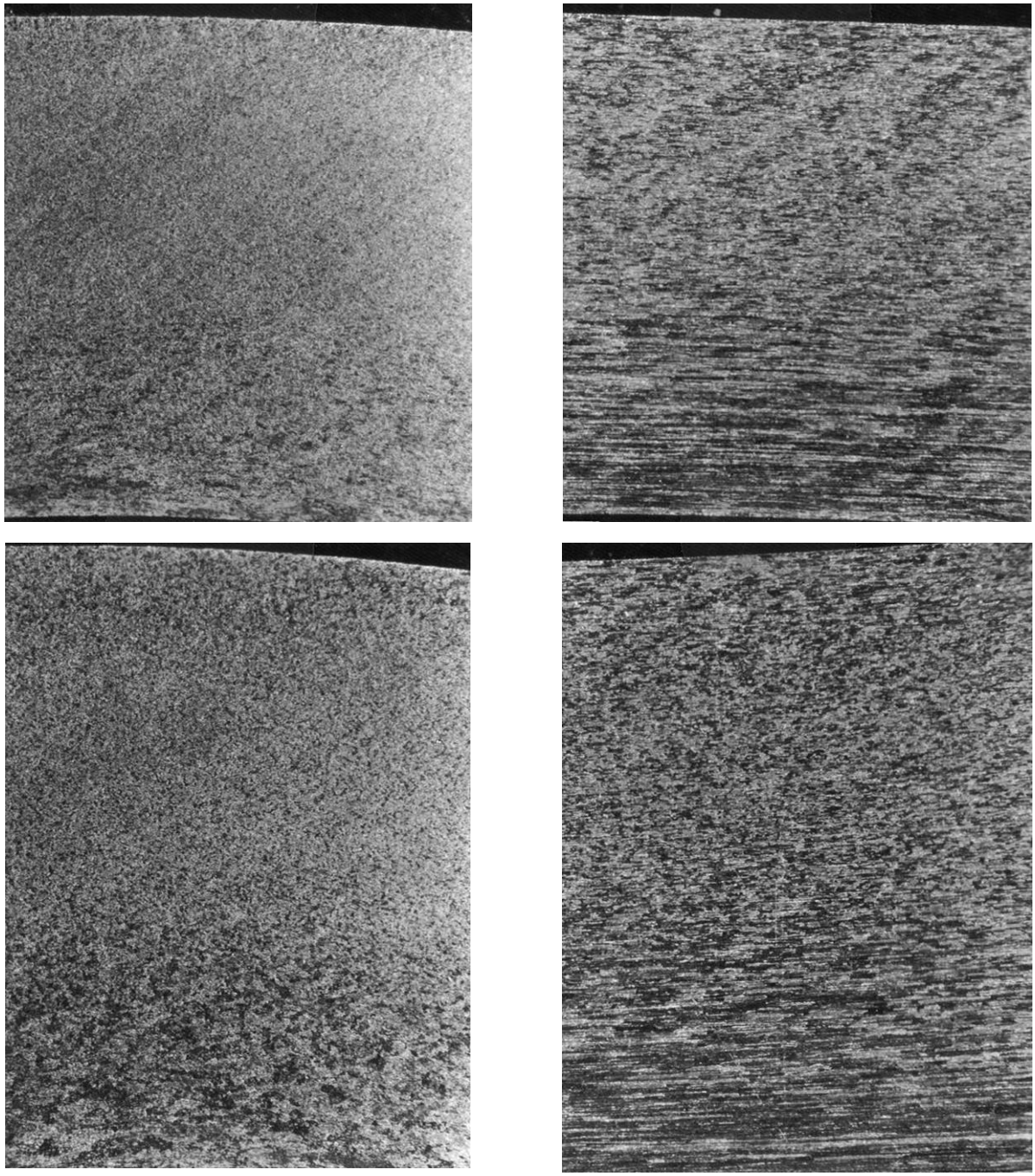

Photomacrographs 16× Magnification Etched

Figure 75. Macrostructure at Extrados (top) and Intrados (bottom) in Commercially-annealed Material shown in 152.4 mm (6-in.) Radius Bend in As-bent Condition (circumferential sections – left, longitudinal sections – right)

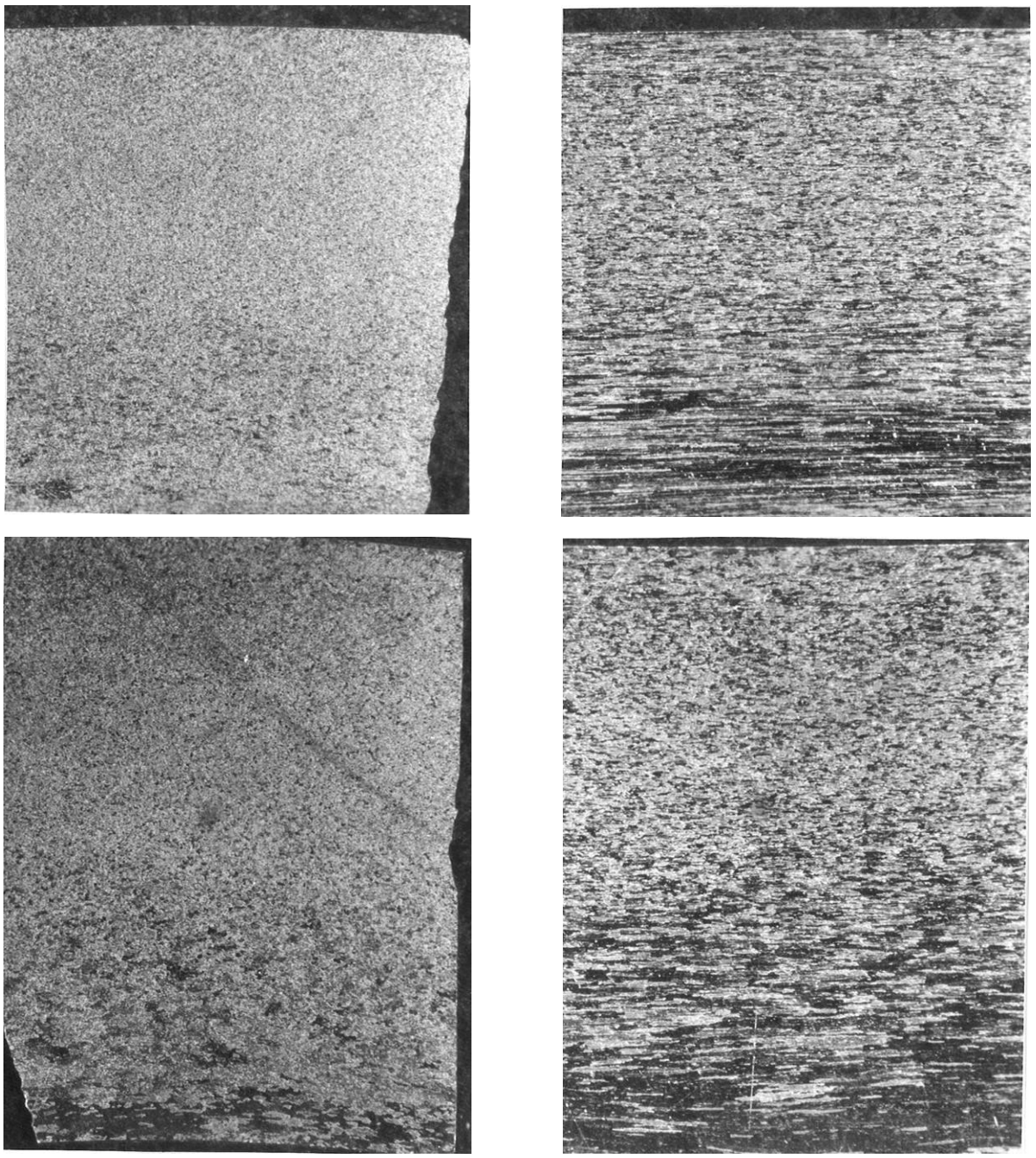

Photomacrographs 16× Magnification Etched

Figure 76. Macrostructure at Extrados (top) and Intrados (bottom) in 152.4 mm (6-in.) Radius Bend in Commercially-annealed Material Illustrated after Thermal Exposure (circumferential sections – left, longitudinal sections – right)

Note: The grain size was similar to that in the as-bent sample (compare with Figure 75).

Photomicrographs 100× Magnification Etched

Figure 77. Microstructure at Extrados (top) and Intrados (bottom) in Commercially-annealed Material in 152.4 mm (6-in.) Radius Bend in As-bentCcondition

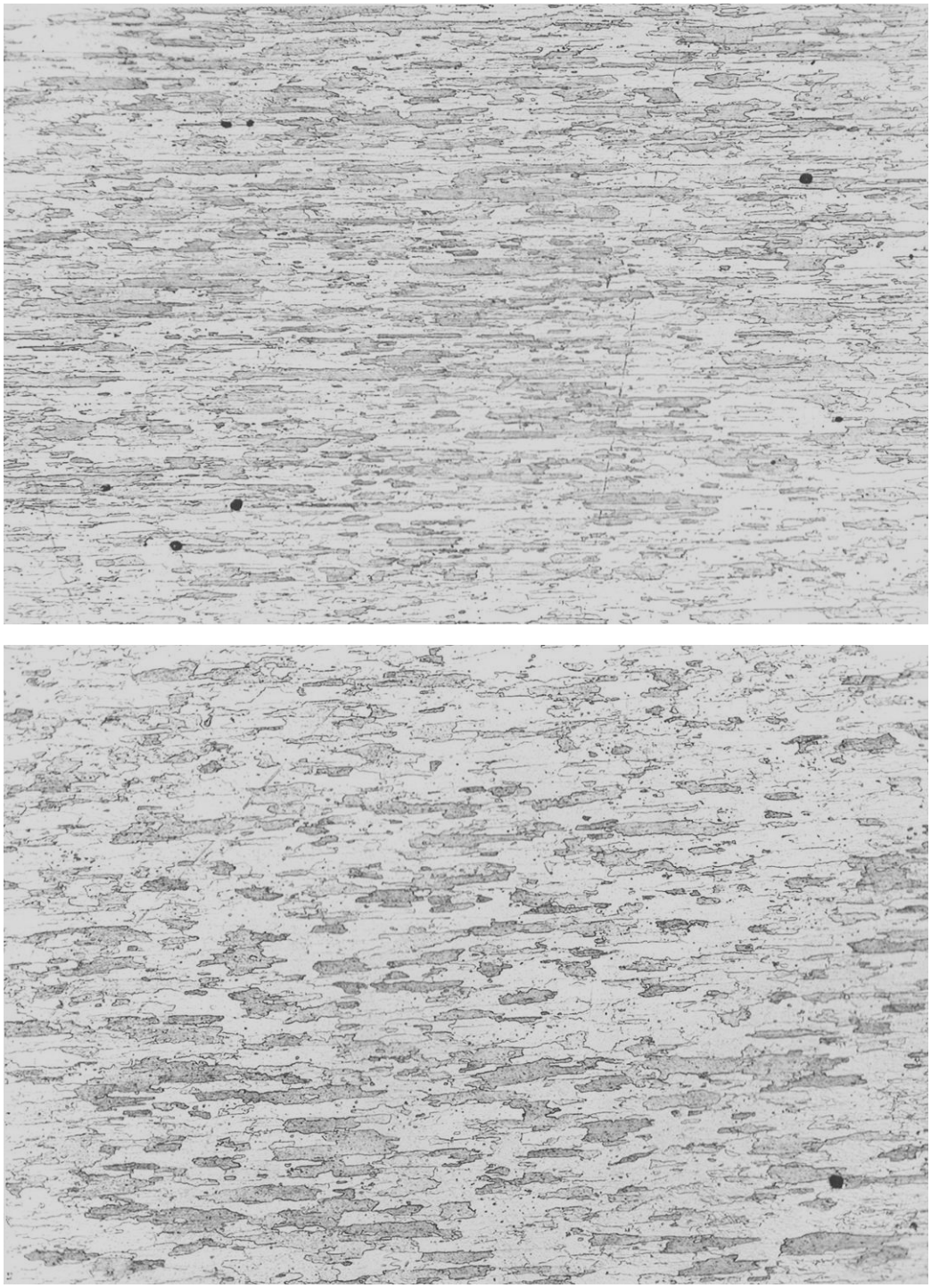

Photomicrographs 100× Magnification Etched

Figure 78. Microstructure at Extrados (top) and Intrados (bottom) in Commercially-annealed Material in 152.4 mm (6-in.) Radius Bend Subjected to Thermal Exposure
Note: The grain size was similar to that in the as-bent sample (compare with Figure 77).

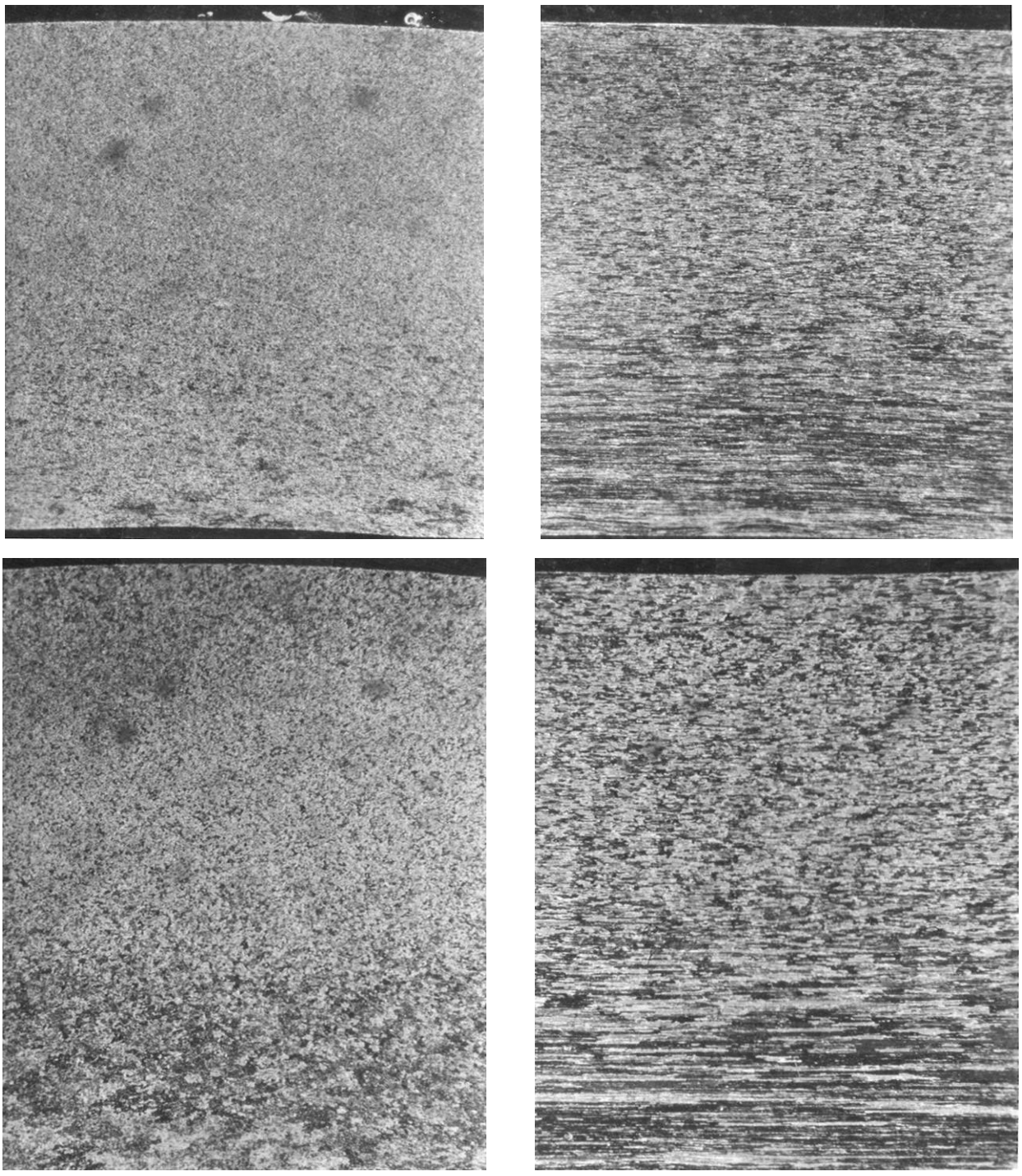

Photomacrographs 16× Magnification Etched

Figure 79. Macrostructure at Extrados (top) and Intrados (bottom) in Commercially-annealed Material in 127 mm (5-in.) Radius Bend in As-bent Condition (circumferential sections – left, longitudinal sections – right)

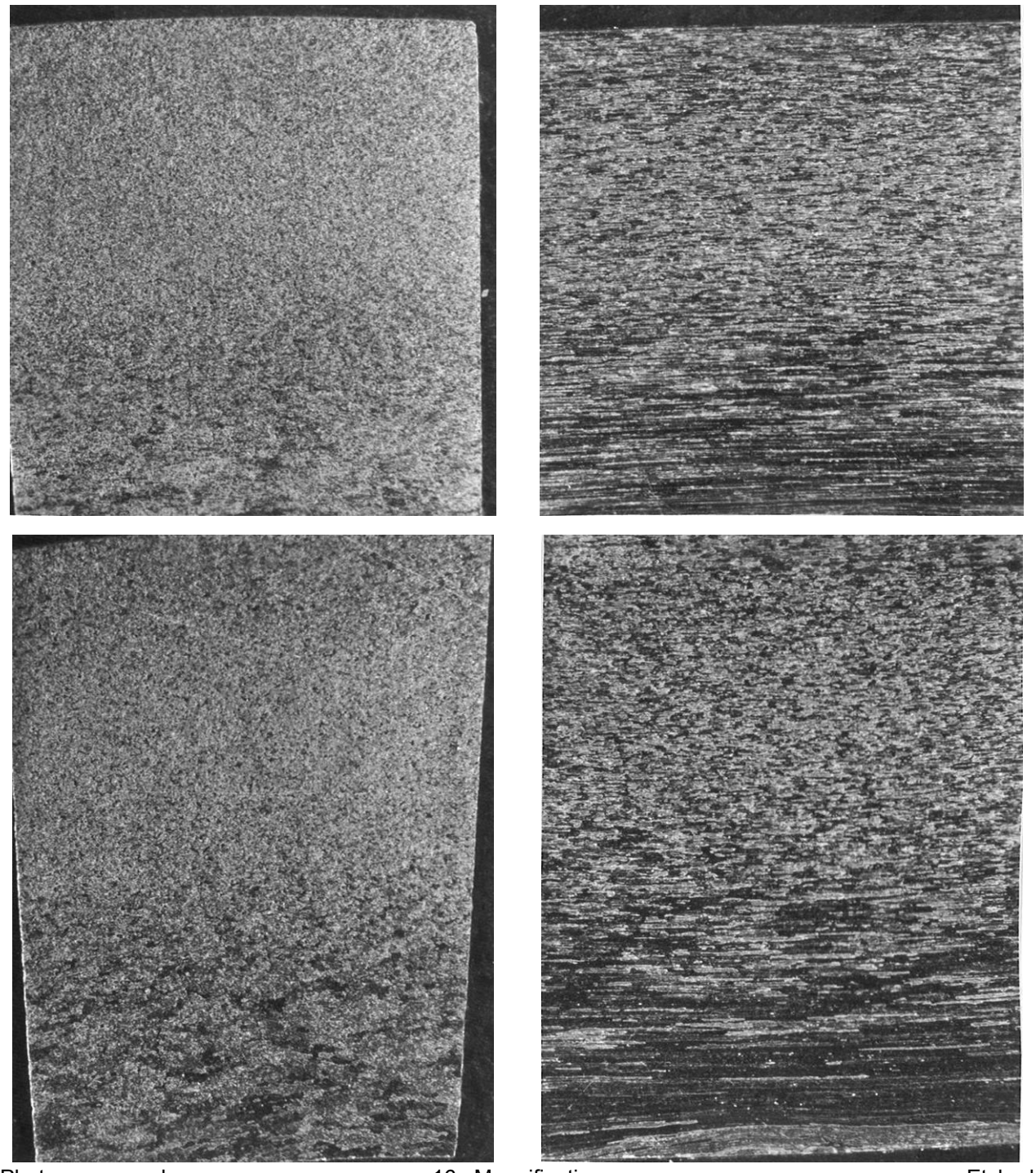

Photomacrographs 16× Magnification Etched

Figure 80. Macrostructure at Extrados (top) and Intrados (bottom) in Commercially-annealed Material in 127 mm (5-in.) Radius Bend Subjected to Thermal Exposure (circumferential sections – left, longitudinal sections – right)

Note: The structure was similar to that in the as-bend sample (Figure 79).

Photomicrographs 100× Magnification Etched

Figure 81. Microstructure at Extrados (top) and Intrados (bottom) in Commercially-annealed Material in 127 mm (5-in.) Radius Bend in As-bent Condition

Photomicrographs 100× Magnification Etched

Figure 82. Microstructure at Extrados (top) and Intrados (bottom) in Commercially-annealed Material in 127 mm (5-in.) Radius Bend Subjected to Thermal Exposure
Note: The grain size was similar to that in the as-bent sample (compare with Figure 81).

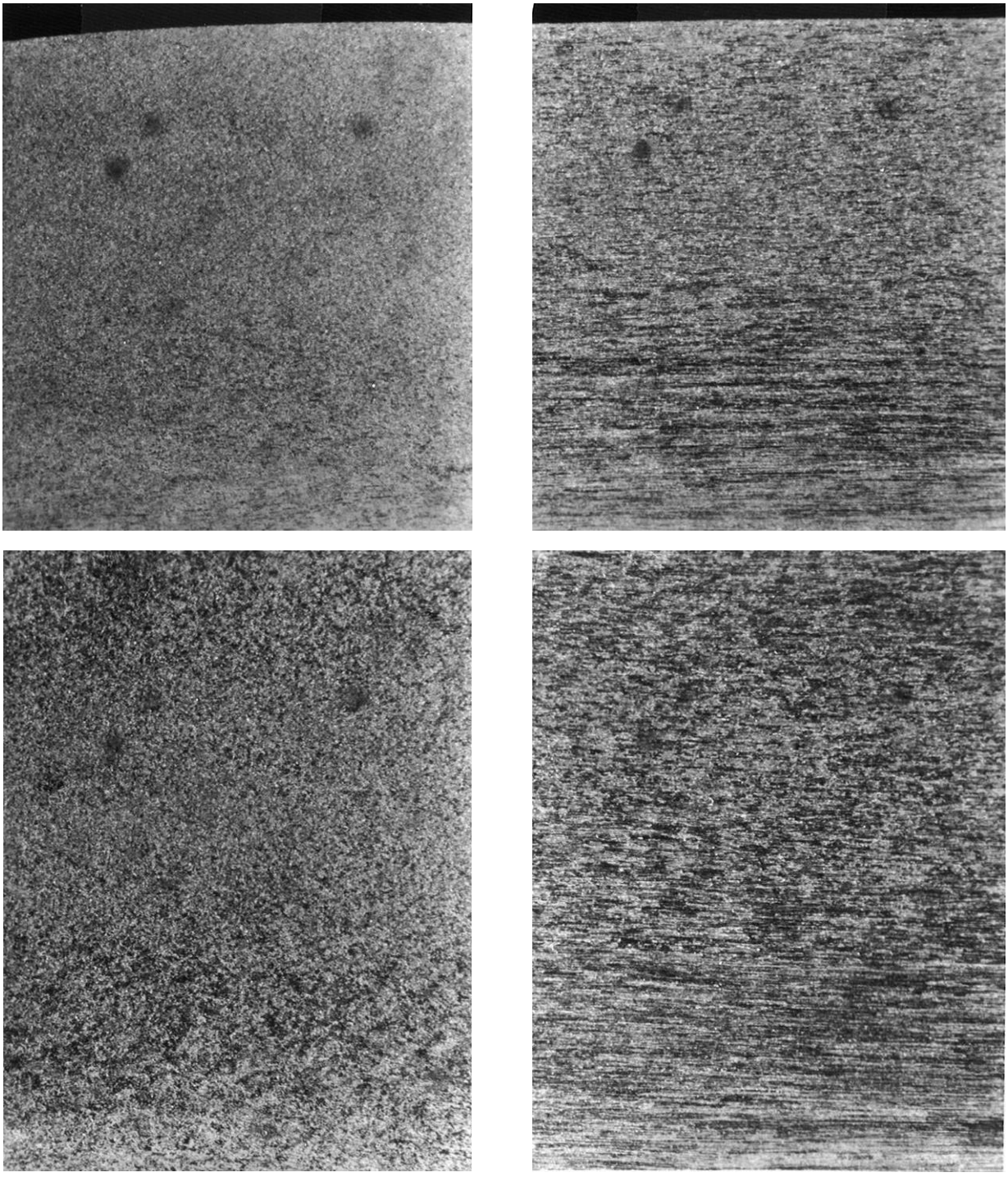

Photomacrographs 16× Magnification Etched

Figure 83. Macrostructure at Extrados (top) and Intrados (bottom) in Modified-annealed Material in 114.3 mm (4.5-in.) Radius Bend in As-bent Condition (circumferential sections – left, longitudinal sections – right)

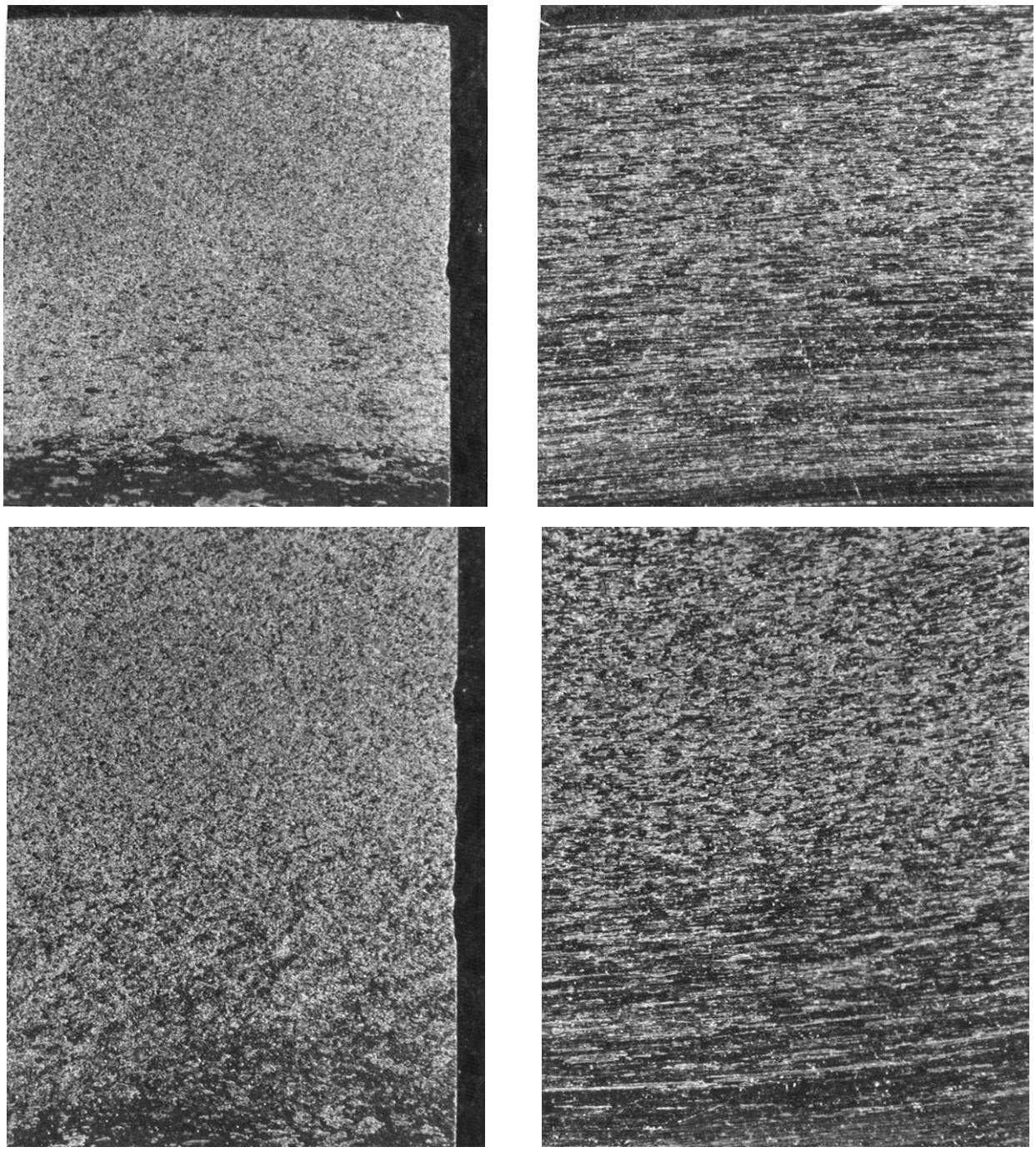

Photomacrographs 16× Magnification Etched

Figure 84. Macrostructure at Extrados (top) and Intrados (bottom) in Modified-annealed Material in 114.3 mm (4.5-in.) Radius Bend Subjected to Thermal Exposure (circumferential sections – left, longitudinal sections – right)

Note: The structure was similar to that in the as-bend sample (Figure 83).

Photomicrographs 100× Magnification Etched

Figure 85. Microstructure at Extrados (top) and Intrados (bottom) in Modified-annealed Material in 114.3 (4.5-in.) Radius Bend in As-bent Condition

Photomicrographs 100× Magnification Etched

Figure 86. Microstructure at Extrados (top) and Intrados (bottom) in Modified-annealed Material in 114.3 mm (4.5-in.) Radius Bend Shown after Thermal Exposure
Note: The microstructure was similar to that in the as-bent sample (compare with Figure 85).

In an issue unrelated to recrystallization, several rounded black nodules were apparent on some of the bends that were subjected to the thermal exposure. When the nodules were "knocked off" with a chisel, the surface of the tube beneath the nodule was still discolored. When explored further via sections cut from these areas, it was discovered that the base material beneath the nodule was pitted, as shown in Figure 87. The diameter and depth of the pit were 12.7 and 2.79 mm (0.5 and 0.110 in.), respectively. A higher magnification view of the pit/base metal interface is illustrated in Figure 88, with energy dispersive x-ray (EDX) analyses of Locations 1, 2, and 3 presented in Figure 89. The elemental spectrums reveal that the particulate in the base metal below the pit (Location 1) was aluminum rich and contained a small amount of nitrogen; no oxygen or sulfur was detected. The spectrums obtained at Locations 2 and 3 indicate that the material in the pit was comprised of oxide of iron, chromium, aluminum, and titanium.

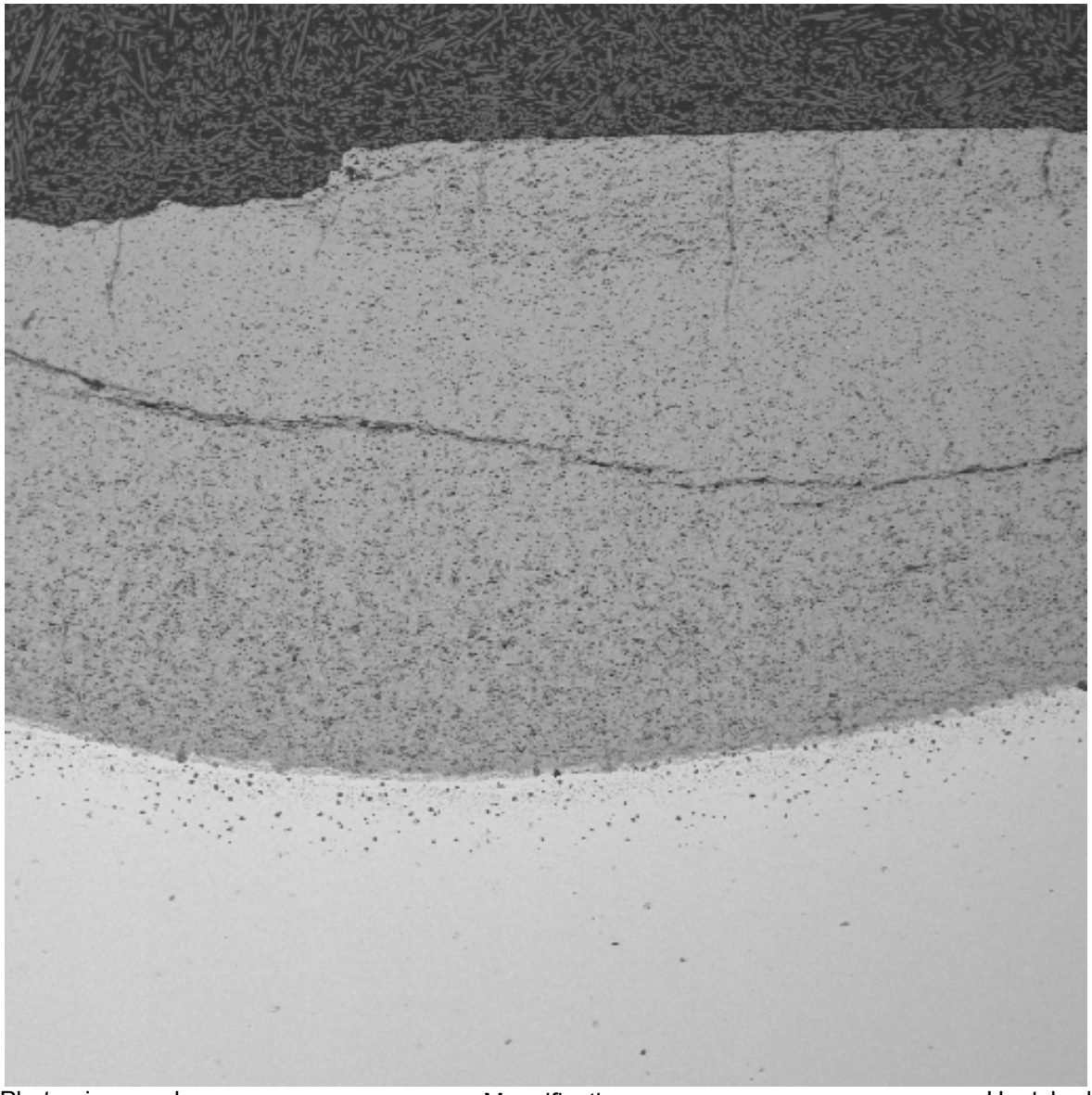

Photomicrograph × Magnification Unetched

Figure 87. Microscopic Appearance of Oxide-like Material Noted below Several Black Nodules Present on Surface of Some Bends Subjected to Thermal Exposure

Note: Macroscopically, the affected areas exhibited a pit-like appearance. (See Figure 88)

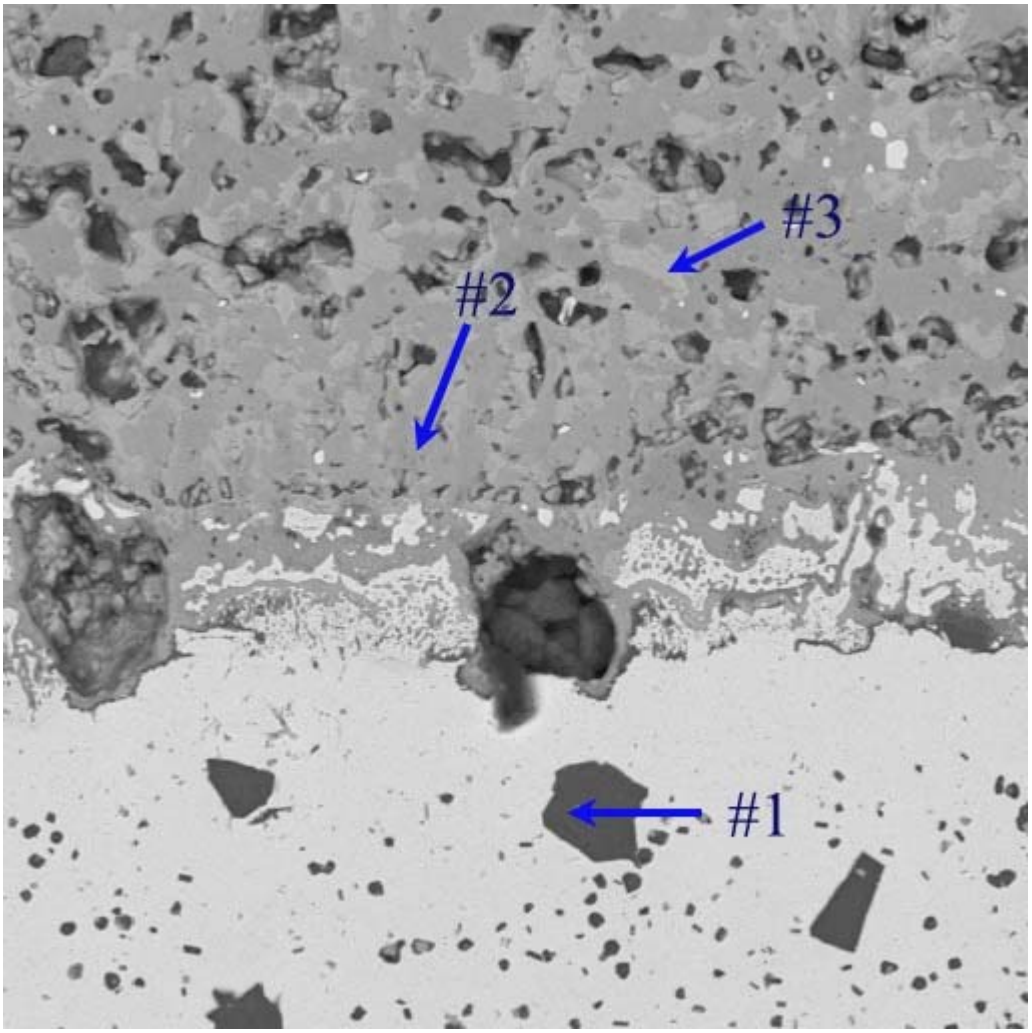

Photomicrograph × Magnification Unetched

Figure 88. Microscopic Appearance of Pit/Tube Interface Illustrated at Higher Magnification

Note: Energy Dispersive X-ray (EDX) analyses were obtained at Locations 1, 2, and 3 and are presented in Figure 89.

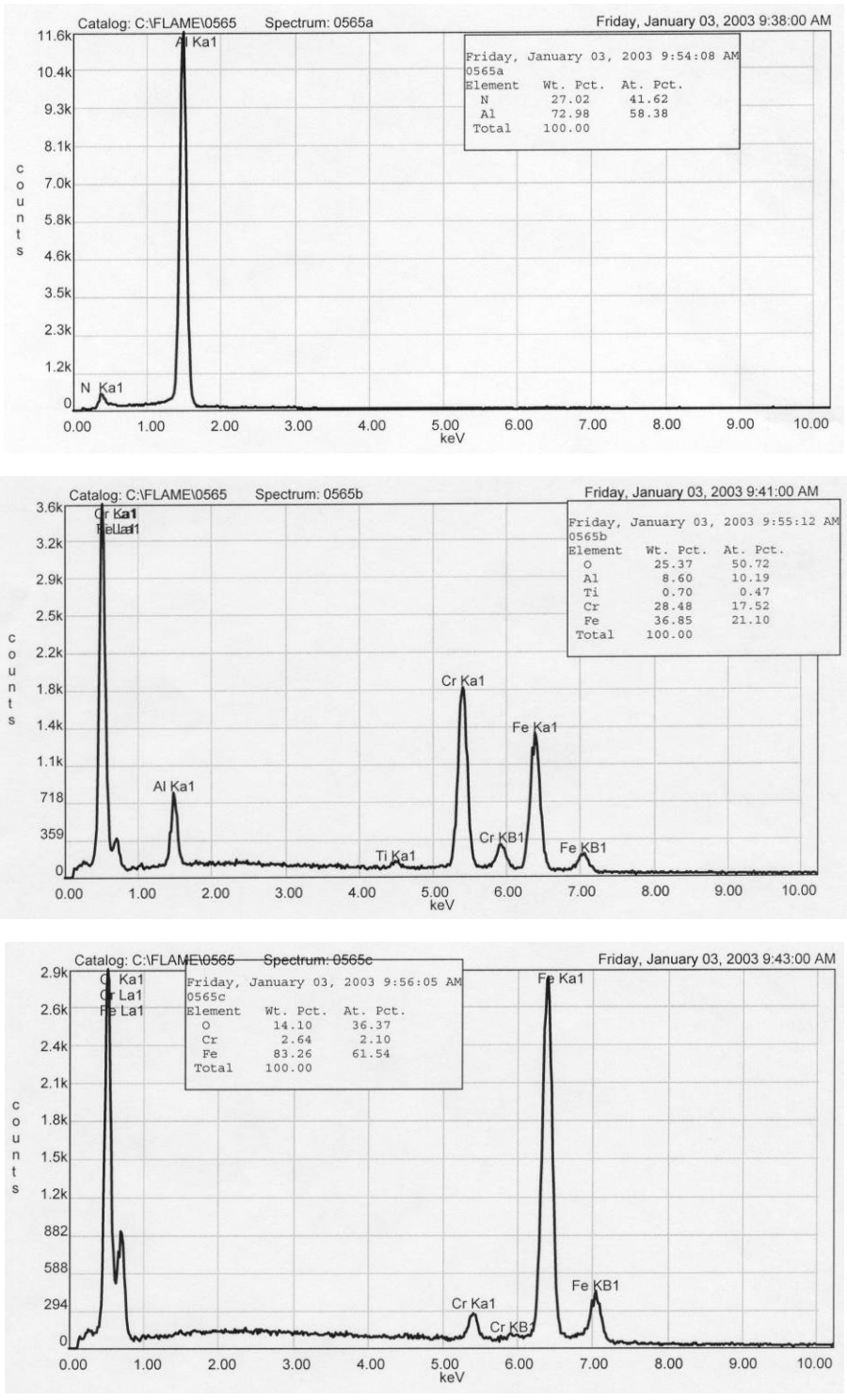

Figure 89. Elemental X-ray Spectrums Indicate Particulate in Base Metal below Pit (Location 1) was Aluminum Rich with Small Amount of Nitrogen, while Material in Pit at Locations 2 and 3 was Comprised of Oxide of Iron, Chromium, Aluminum, and Titanium

5.4.6 Hardness Evaluation

Hardness surveys were performed on the cross sections removed from the center of the bend. Readings were obtained near the center of the wall on the extrados and intrados sides in both the as-bend and thermally-exposed samples. The results are presented in Table 20 along with the original hardness of tube prior to bending. The results indicate a 5-7 point HRC increase in hardness in both the extrados and intrados at the center of the bend compared to the original hardness in the straight tube. After the thermal exposure, the hardness at the center of the bend decreased to values comparable to those in the original tube.

5.5 Task 5. High Temperature Corrosion Limits of MA956

5.5.1 Laboratory Testing for Working Fluid Side – Oxidation Testing

(Note: Reported from Cooperative Agreement DE-FC26-00-NT40970)

Initial development trials investigated the oxidation rate of MA956. Bar samples were created and exposed in air at 1300°C (2372°F). The total mass change data are shown in Figure 90, and the observed and predicted lifetimes as a function of specimen thickness are shown in Figure 91. The lifetime calculations were based on a two-stage oxidation model developed using data for the MA956HT alloy, but using the oxidation rates (parabolic and linear stages) and transition oxide thickness measured for the MA956 alloy. The fit of the model appears to be good, except for the thinnest specimen. The only difference from the fit used for the MA956HT alloy was a change in the factor that qualifies the rate exponent in the 'linear' oxidation phase (fn3) from 0.06 to 0.03 (see Figure 91). Obviously, the oxidation lifetime of the MA956 alloy at 1300°C (2372°F) in air is significantly lower than that of the MA956HT alloy. The important difference between the two alloys appears to be that the rate of oxidation (in Stage 2 and Stage 3) is higher for the MA956 alloy. Since both alloys form the same oxide, the reason for this difference is not obvious. The oxidation rate of alumina-forming alloys can be significantly affected by doping with reactive elements such as Y, but the Y levels of the MA956 and MA956HT alloys are essentially the same (0.40 and 0.38 weight percent, respectively). Specimens have been prepared for examination of the structure and compositions of the alloy-oxide interface and the oxide grain boundaries by TEM.

Further specimens are being exposed at 1250, 1200, and 1100°C (2282,1292 and 2012 °F) in air to determine lifetimes with five samples (out of a total of seven) of different thickness taken from MA956 bar stock having failed at 1250°C (2282°F). The observed oxidation-limited lifetimes are shown in Figure 92 with data points for a similar set of samples of the MA956HT alloy included for comparison. Note that the data points with arrows indicate runs that are still in progress, and that the oxidation lifetime will be longer than presently indicated by those points. The lifetimes of MA956 and MA956HT at 1250°C (2282°F) appear to be more than double those at 1300°C (2372°F). The coincidence of the 1250°C (2282°F) lifetimes for MA956 with the 1300°C (2372°F) data points for MA956HT indicate that the latter alloy has a 50°C (122°F) advantage at these very high temperatures. Analysis of the kinetic data to generate the data needed for testing or modifying the lifetime model has not yet been completed. However, a procedure suggested by Monceau and Pieraggi1 for deducing the 'true' parabolic rate constant, kp, from experimental kinetic data has been examined using the oxidation data for MA956 and MA956HT. The 'true' parabolic rate constant is not influenced by any initial, rapid mass gain from transient oxide formation, which often can bias the value usually calculated. Initial results suggest that the use of the values of the true kp in the life prediction calculations allows an improved fit to the observed lifetime data for MA956 and MA956HT at both 1250° and 1300°C (2282° and 2372°F).

Table 20. Hardness Evaluation

Bend Radius (mm)	Bend Radius (in.)	Material	Original Hardness HRC (BHN)	Hardness – As-Bent HRC (BHN)		Hardness – After Thermal Exposure HRC (BHN)	
			Straight Leg	Extrados	Intrados	Extrados	Intrados
304.8	12	CA	25 (253)	31.5 (297)	30 (286)	25 (253)	25 (253)
304.8	12	MA	24-27 (247-264)	31 (294)	31 (294)	24 (247)	25 (253)
190.5	7.5	CA	25 (253)	32 (301)	31 (294)	25 (253)	25 (253)
190.5	7.5	MA	26-27 (258-264)	33 (311)	31 (294)	25 (253)	25 (253)
152.4	6	CA	25 (253)	34 (319)	31 (294)	27.5 (267)	28 (271)
152.4	6	MA	26-27 (258-264)	32.5 (306)	32 (301)	26.5 (261)	24 (247)
127	5	CA	25 (253)	33 (311)	32.5 (306)	27 (264)	26 (258)
127	5	MA	24-27 (247-264)	33.5 (315)	29 (279)	26 (258)	26 (258)
107.95	4.25	CA	25 (253)	33 (311)	27 (264)	28 (271)	27 (264)
107.95	4.25	MA	26-27 (258-264)	31 (294)	29.5 (283)	26 (258)	26 (258)

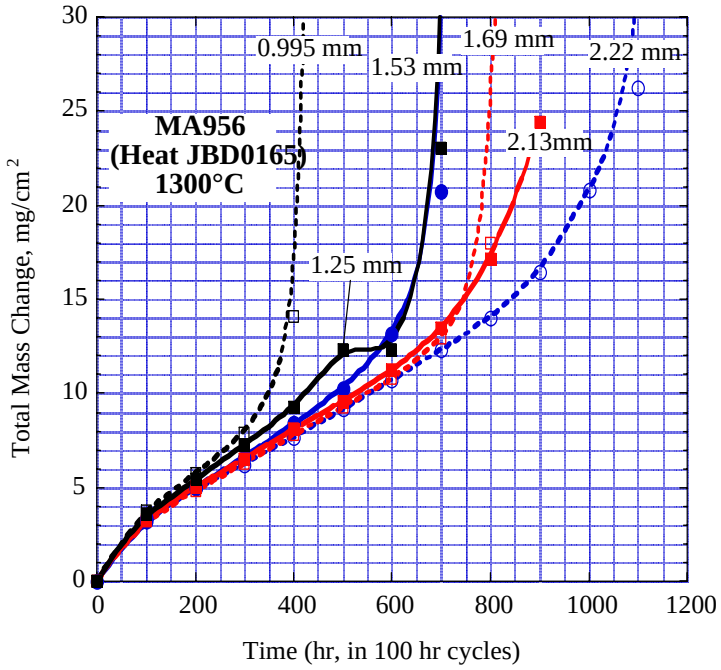

Figure 90. Total Mass Gain Data for MA956 Alloy at 1300°C (2372°F), 100 Cycles in Air

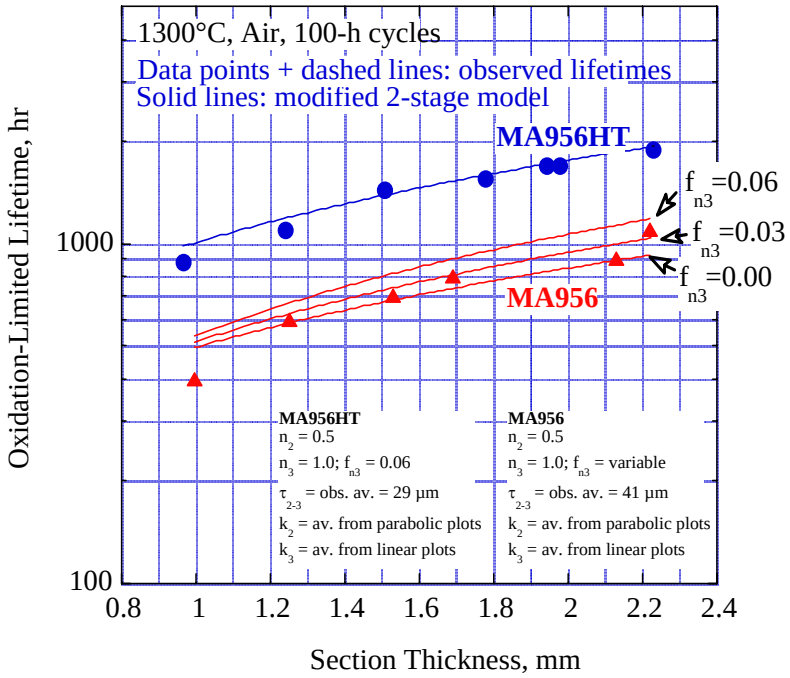

Figure 91. Comparison of Oxidation Lifetimes of MA956 and MA956HT Alloys at 1300°C (2372°F) in Air as Function of Specimen Thickness
Note: The data points indicate observed lifetimes. The solid line is the fit of a two-stage model developed from data on the MA956HT alloy.

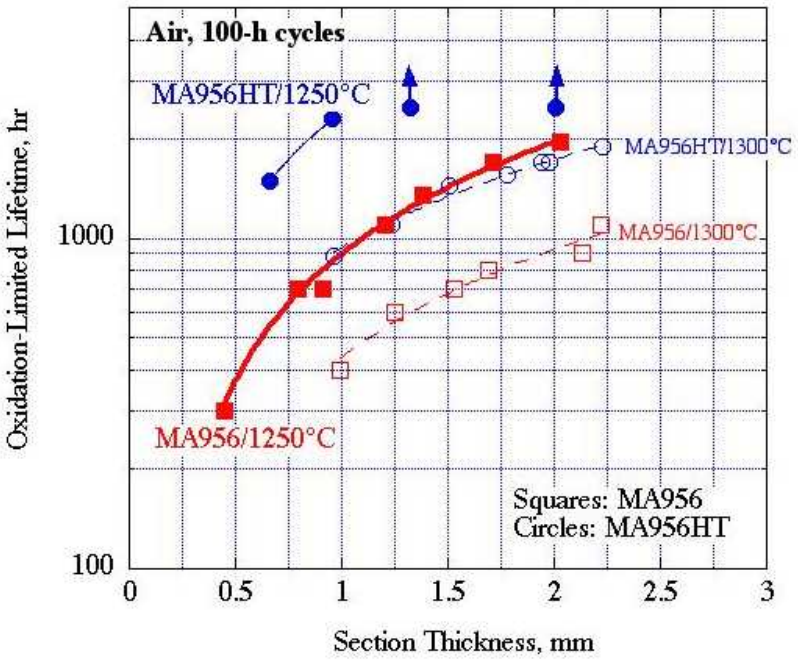

Figure 92. Plot of Oxidation Lifetimes as Function of Sample Thickness for MA956 and MA956HT Alloys at 1250°C and 1300°C in Air

And finally, further modification of the lifing model has involved the replacement of the specimen thickness term by a 'shape factor' (volume/surface area). The lifetime data generated on MA956HT in an ORNL in-house program used disc-shaped specimens, whereas the MA956 specimens are parallelepipeds, so that there existed the possibility that the comparison of oxidation behavior was influenced by specimen shape. The range of V/A values of the specimens used so far is 0.3-0.7 mm (0.0118-0.0275 in.) (discs) and 0.2-0.8 mm (0.0078 - 0.0314 in.) (parallelepipeds). Preliminary calculations using the revised model indicate a reasonable fit to the experimental data at 1300°C (2372°F), without the use of any 'adjusting' parameters, i.e., assuming strictly parabolic (n=0.5) and linear (n=1) segments to the kinetic curves.

5.5.2 Laboratory Base Metal Testing for Fireside Environment

In this task coupons of Incoloy MA956 and Haynes 230 were coated with coal ashes and exposed to high temperature gases in electrically heated furnaces to determine the material's susceptibility to corrosion. The tests were conducted at three different temperatures with two different gas compositions and three different ashes each for 1000 hours. The gases were synthesized from gas cylinders to simulate the combustion exhaust gases from Western (low sulfur) and Eastern (high sulfur) coals. Similarly, the ashes were representative of these coals and they were produced / synthesized by the addition of chemicals to a western bituminous coal char. This investigation was comprised of six isothermal corrosion experiments.

5.5.2.1 Test Parameters and Matrix

The tests were conducted at 1093, 1148, and 1204°C (2000, 2100, 2200°F) with the gas and ash compositions given in Table 21 and Table 22, respectively. With regard to the ashes, the main ingredient was char produced by the partial gasification of bituminous coal from the West Elk Mine of Colorado.

Table 21. Gas Compositions

Species	Composition (volume %)	
	Gas Mixture 1	Gas Mixture 2
O_2	4	2
CO_2	15	15
$H_2O_{(V)}$	10	5
SO_2	0.25	1.0
N_2	Balance	Balance

Table 22. Components Added to Char

Ash ID	Basic Composition	Additional Components
1	Char (West Elk Mine)	——-
2	Char (West Elk Mine)	1.0% Na_2SO_4 + 1.0% K_2SO_4 + 1.0% S
3	Char (West Elk Mine)	2.0% Na_2SO_4 + 2.0% K_2SO_4 + 2.0% S + 1.0% KCl

The compositions/analyses of the ashes that were coated on the coupons are presented in Table 23 and the overall test matrix is presented in Table 24.

Table 23. Analysis of Test Ashes

Component	Ash 1 (Char)	Ash 2	Ash 3
Si Dioxide	14.6	11.6	7.6
Al Dioxide	6.0	6.0	6.0
Ti Dioxide	0.3	0.3	0.3
Fe Oxide	1.3	1.3	1.3
Ca Oxide	3.3	3.3	3.3
Mg Oxide	0.3	0.3	0.3
Na Oxide	0.4	1.4	2.4
K Oxide	0.3	1.3	2.3
S Trioxide	1.2	2.2	3.2
P Pentoxide	0.3	0.3	0.3
KCl			1.0
Carbon	72.1	72.1	72.1

* Ash made from char from partial gasification of Bituminous coal from West Elk Mine therefore all oxides in their highest oxide state.

Table 24. Test Matrix

Test No.	Temperature °C (°F)	Gas Composition	Material	Ash Composition
1	1093°C (2000°F)	#1	MA956 & 230	1 – 3
2	1093°C (2000°F)	#2	MA956 & 230	1 – 3
3	1148°C (2100°F)	#1	MA956 & 230	1 – 3
4	1148°C (2100°F)	#2	MA956 & 230	1 – 3
5	1204°C (2200°F)	#1	MA956 & 230	1 – 3
6	1204°C (2200°F)	#2	MA956 & 230	1 – 3

5.5.2.2 Pre-Characterization of Test Coupons

The basic compositions of the test coupon materials are provided in Table 25. The test coupons were pre-characterized by first giving them a unique identifying number that was stamped near the top of the coupon (outside of the testing area). A pair of test coupons was used for each test condition (e.g., Test #1: MA956 coupons #1 and 2 tested under Ash #1) because one was removed after 500 hours of testing, while the other was tested for the full 1000 hours. Once the coupons were identified, thickness measurements were taken at six locations on each coupon and the results averaged. These measurements were utilized to determine the performance of the samples after exposure.

Table 25. General Composition of Test Materials

Material	C	Si	Mn	Al	Co	Cr	Ni	Mo	Ti	Fe	W	Other
MA956	0.014	0.02	0.07	4.74	0.02	18.7	0.04	—	0.37	Bal	—	0.48 Y_2O_3
230	0.10	0.40	0.50	0.30	5.0 max	22.0	57.0	2.0	—	3.0 max	14.0	0.02-La, 0.015 max B

5.5.2.3 Description of Test Facility

Figure 93 is a simplified schematic of the test facility. The gases used in the tests were produced by blending bottled gases, in proportions controlled by precision-calibrated flow meters, to yield the compositions shown in Table 21. After combining nitrogen, carbon dioxide, and oxygen, the gas mixture passed through a heated humidifying column at a controlled temperature to entrain it with the desired amount of water vapor (by volume). After the column, heated/insulated tubing maintained the gas at 121°C (250°F) to prevent any condensation and carried the gas to a mixing chamber where SO_2 was injected. The mixing chamber extended into the furnace and connected to a catalyst reaction chamber that converted the SO_2 to SO_3. The SO_3 rich gas then passed over the test specimens at a rate of two liters per minute (a rate large enough to prevent the gas from stratifying inside the test area), exited the furnace, passed through a scrubber, and discharged to atmosphere.

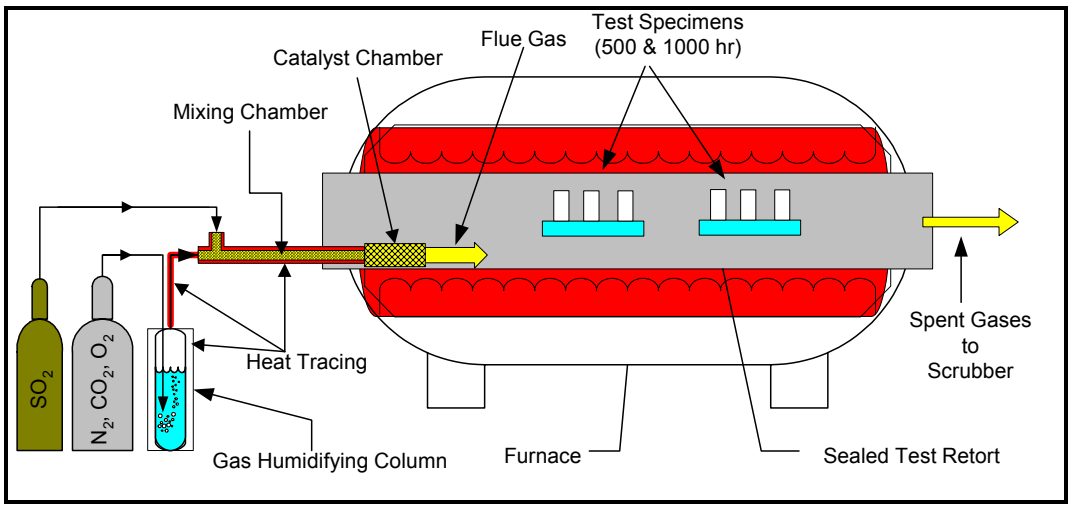

Figure 93. Schematic of Test Facility

5.5.2.4 Test Procedure

The synthetic ash deposits used to coat the corrosion coupons were produced in the laboratory using char and reagent grade chemicals that were ground to a uniform size and then thoroughly blended. An organic binder was added to make the deposit into a paste that was applied to both sides of the test coupons at an approximate thickness of 3 mm (0.118-inch). The ash coated specimens were then suspended from alumina rods hung on a rectangular fixture as shown in Figure 94.

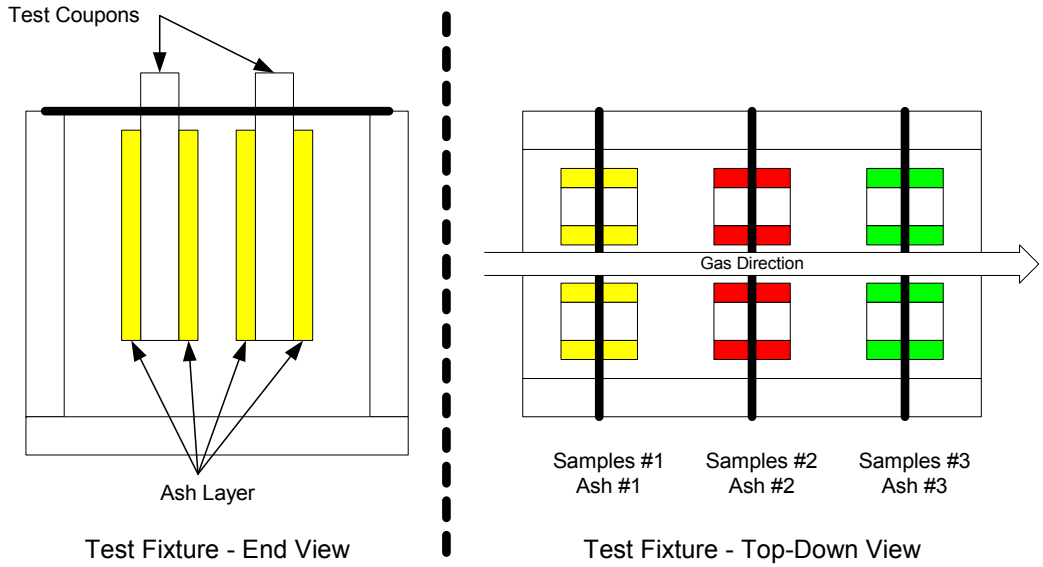

Figure 94. Coupon Arrangement in Test Fixture

There were two fixtures per test, one containing the 500-hour specimens and the other containing the 1000-hour specimens. Once loaded, the ends of the furnace were sealed and the unit was heated to the test temperature while under an inert purge of argon to prevent premature oxidation. Upon reaching the test temperature, the purge gas was switched off and the flue gas mixture was introduced and maintained at a steady flow rate throughout the test cycle. To ensure that the ash remained active during the entire test, it was replenished every 100 hours. Upon completion of a 100-hour cycle, the furnace was cooled under an inert argon purge until ambient temperature was reached. The specimens were then removed, cleaned of the spent ash, re-coated with fresh ash, and returned to the furnace. After 500 hours of testing was complete, the 500-hour samples were removed and subjected to examination. The remaining 1000-hour set of samples continued this test cycling procedure until the total exposure period of 1,000 hours was completed.

After exposure, the coupons were left in the uncleaned condition so that a section with corrosion product could be carefully removed. These sections were mounted for a cross-sectional metallurgical analysis and determination of the sound-metal thickness. The mounts were subjected to a dry polishing procedure to retain any possible chloride species. The depth of subsurface attack was measured on the mounted cross sections as was the remaining wall thickness of the coupons (labeled “X-Section”). Based on the collected data the maximum metal wastage (MMW) and corrosion rate (CR) was calculated. In addition, the remnant deposit/scale layers were examined using a scanning electron microscope (SEM) equipped with energy dispersive x-ray (EDX) analysis.

The remaining portion of each coupon was then thoroughly cleaned of all corrosion products using a low-pressure glass-bead blasting technique. The cleaned coupons were then measured to determine their post exposure thickness. Using the post exposure data, the MMW and CR were calculated (labeled “Descaled”).

5.5.2.5 Macroscopic Examination

The macroscopic examination of the samples consisted of evaluating the coupons for evidence of exterior wastage and documenting the final wall thickness. For this analysis the coupons each had a section carefully removed and set aside for microscopic examination. The remaining portions of each sample were then cleaned of any corrosion product or scale via low-pressure glass-bead blasting. The remaining wall thickness was then measured on each coupon and recorded for corrosion rate calculations. The data for each set was labeled "Descaled" in the graphs, which are discussed in the Corrosion Rate section of this report. The following sections describe the results of this portion of the investigation.

Corrosion Test #1: Corrosion Test #1 was conducted at 1093°C (2000°F) using Gas #1 (15% CO_2 + 10% $H_2O_{(v)}$ + 0.25% SO_2 + 4% O_2 + Bal N_2) and all three ash deposits. The appearance of the Test #1 samples is shown in Figure 95.

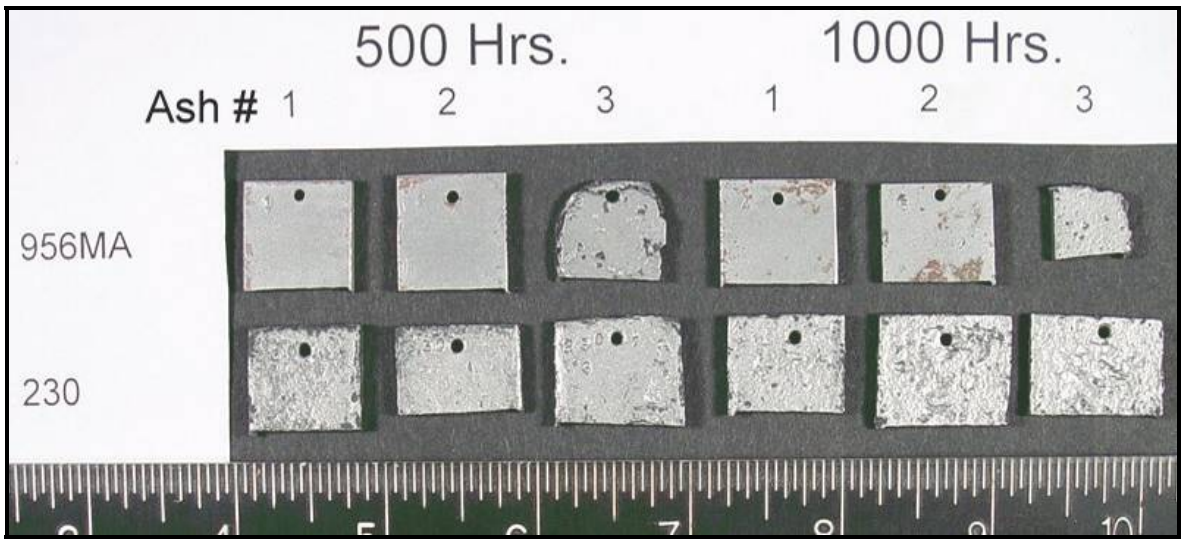

Figure 95. Test #1 Samples After Cleaning

With the exception of the MA956 samples tested under Ash #3, the MA956 samples displayed only minor wastage. The 230 samples displayed damage in the form of pitting that appeared more pronounced in the 1000-hour samples.

Corrosion Test #2: Corrosion Test #2 was conducted at 1093°C (2000°F) using Gas #2 (15% CO_2 + 5% $H_2O_{(v)}$ + 1.0 %SO_2 + 2% O_2 + Bal N_2). Both materials were tested under all three ash deposit compositions. The Test #2 samples are shown in Figure 96. The MA956 samples only exhibited pitting and general wastage after 1000 hours of exposure under Ash #2 and #3. In contrast, the 230 samples displayed substantial wastage after 500 hours and decidedly more wastage after 1000 hours. In fact, two of the three 1000-hour 230 samples fractured during the sectioning process.

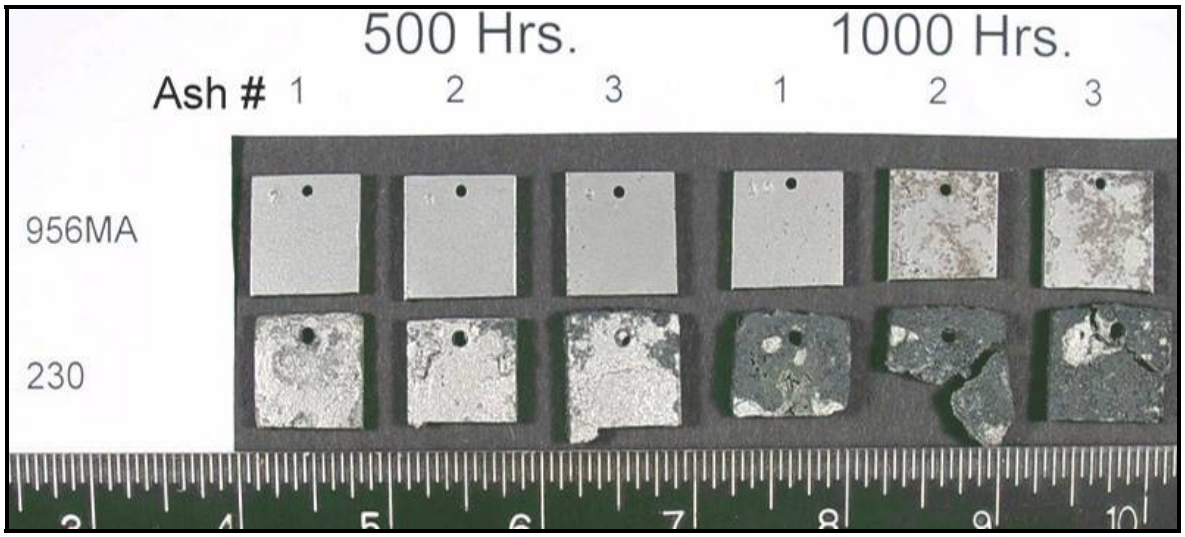

Figure 96. Test #2 Samples After Cleaning

Corrosion Test #3: Corrosion Test #3 was conducted at the second temperature of 1148°C (2100°F) using Gas #1 (15% CO_2 + 10% $H_2O_{(v)}$ + 0.25% SO_2 + 4% O_2 + Bal N_2). Both materials were tested under all three ash deposits. The condition of the Test #3 samples is presented in Figure 97. Both materials displayed little, if any, exterior signs of wastage after 500 hours of testing as can be seen in Figure 97. After 1000 hours of testing, the MA956 samples exhibited minor pitting damage and evidence of general wastage in the samples test under Ash #2 and #3. Conversely, all of the 230 samples displayed significant pitting damage as well as general wastage.

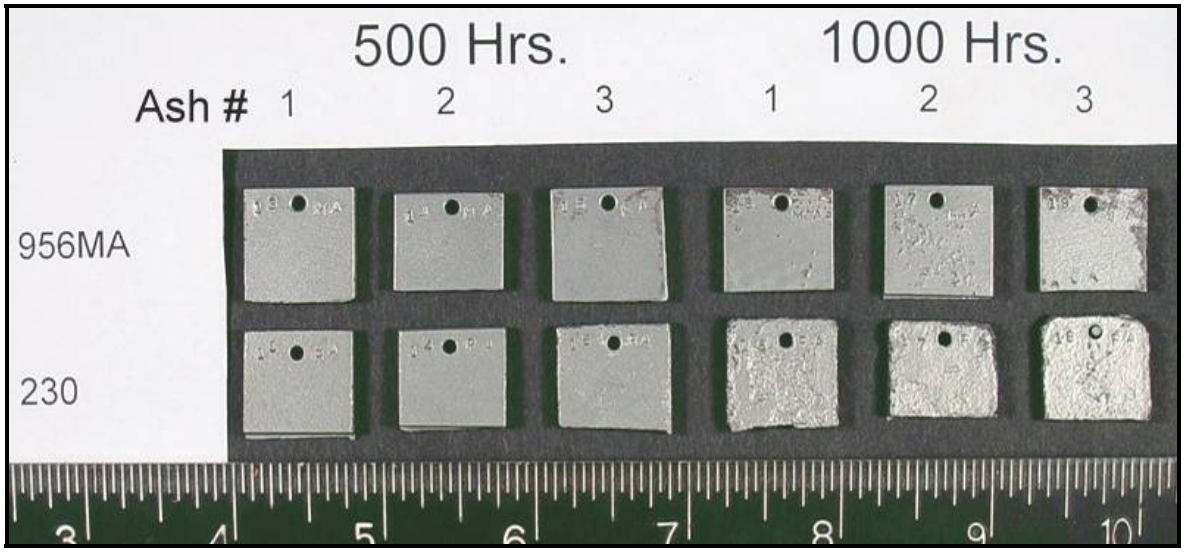

Figure 97. Test #3 Samples After Cleaning

Corrosion Test #4: Corrosion Test #4 was also performed at 1148°C (2100°F) again using all three ash deposits but the samples were tested under Gas #2 (15% CO_2 + 5% $H_2O_{(v)}$ + 1.0 %SO_2 + 2% O_2 + Bal N_2). The samples from Test #4 are presented in the cleaned condition in Figure 98.

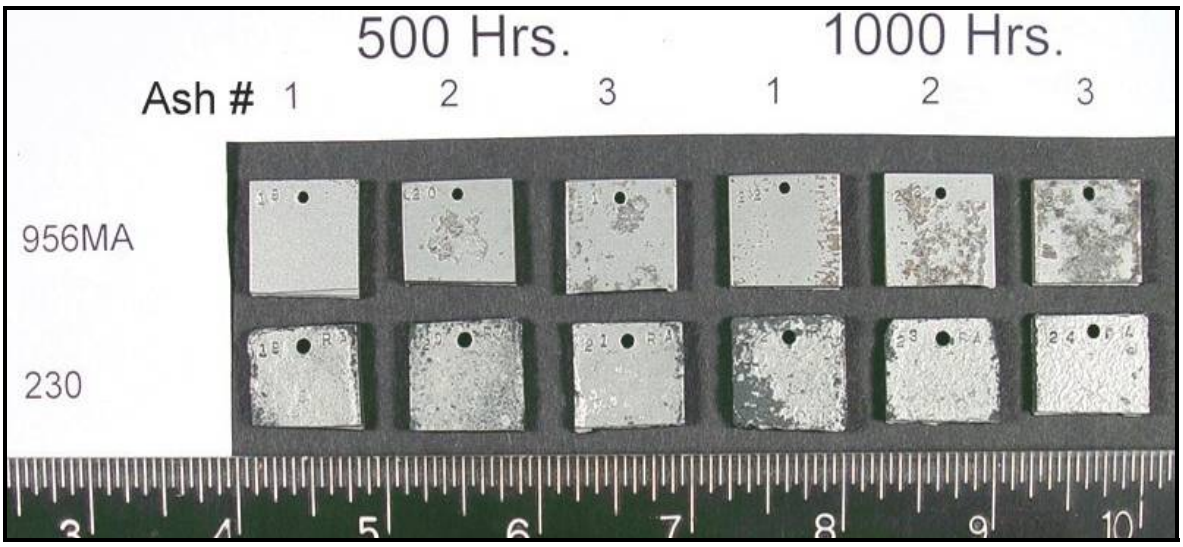

Figure 98. Test #4 Samples After Cleaning

As was the case before, the bulk of the corrosion in the MA956 samples (both 500 and 1000-hour samples) occurred in the coupons tested under Ash #2 and #3. In both cases, the samples exhibited pitting damage. With regard to the 230 samples, it was observed that both sets (500 and 1000-hr) displayed evidence of general corrosion and pitting with a noticeable increase in the severity of the corrosion noted amongst the 1000-hr samples.

Corrosion Test #5: Test #5 was conducted at the highest temperature of 1204°C (2200°F) using Gas #1 (15% CO_2 + 10% $H_2O_{(v)}$ + 0.25% SO_2 + 4% O_2 + Bal N_2) and all three ash deposits. The appearance of the test samples in the cleaned condition is shown in Figure 99. These conditions produced pitting in the MA956 samples under Ash #1 and #3 with the severity of the pitting increasing in the 1000-hr samples. With exception of the Ash #1, 500-hr 230 sample, all of the 230 samples displayed significant corrosion damage. The 1000-hr Ash #1 sample was completely consumed and crumbled into pieces during sectioning. The shorter than normal appearance of the 1000-hr Ash #3 sample is also a result of excessive corrosion damage as the bottom portion of the sample crumbled upon sectioning. Therefore, a second section had to be taken from slightly higher up on the sample in order to have something to examine microscopically.

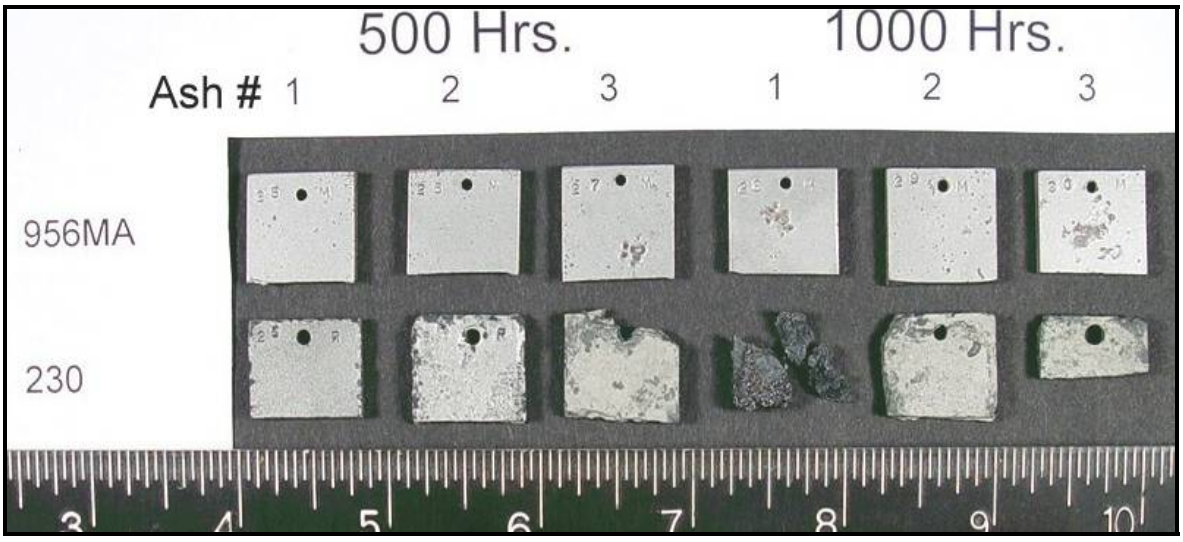

Figure 99. Test #5 Samples After Cleaning

Corrosion Test #6: The conditions for Corrosion Test #6 were 1204°C (2200°F), all three ashes, and Gas #2 (15% CO_2 + 5% $H_2O_{(v)}$ + 1.0 %SO_2 + 2% O_2 + Bal N_2). The samples from Test #6 are presented in the cleaned condition in Figure 100.

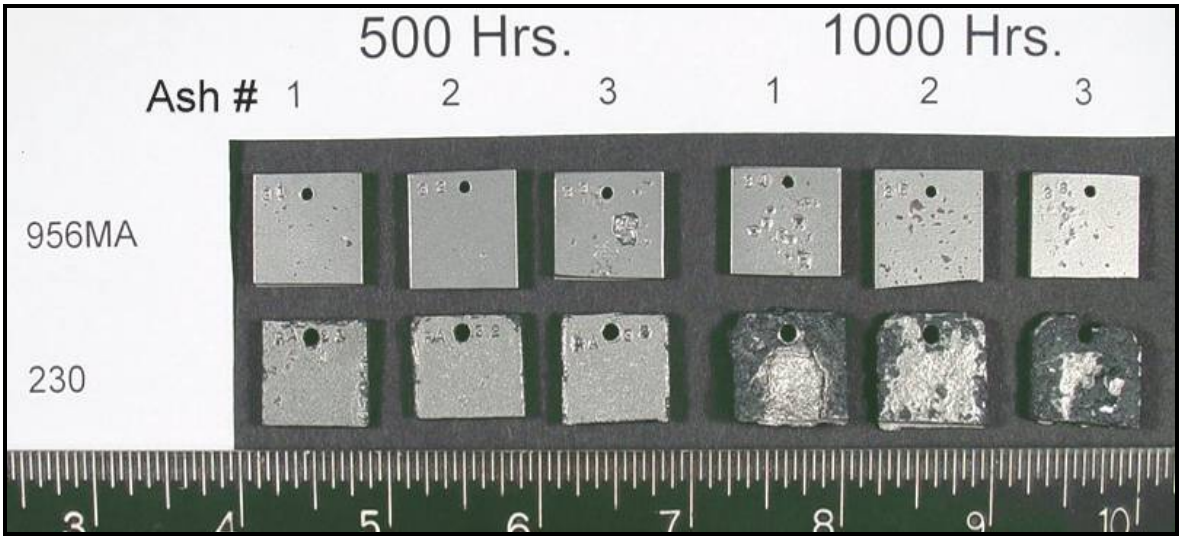

Figure 100. Test #6 Samples After Cleaning

Several of the MA956 samples exhibited pitting damage with the largest pit noted in the 500-hour, Ash #3 sample. The 500-hour 230 samples displayed general wastage damage with some scattered pitting noted along the edges of the coupons. The 1000-hour samples were significantly worse in that they exhibited so much wastage it was difficult to determine if it was all from conjoined pits or from large-scale general damage.

5.5.2.6 Microscopic Examination

The sections removed from the test samples were carefully mounted for microscopic examination to characterize the remnant deposit/scale and corrosion products as well as to search for subsurface attack. Additionally, the wall thickness of each cross section was measured as was the deepest pit and the maximum subsurface penetration. These were combined to calculate the "Descaled" CR. Since similar corrosion morphologies were noted between the 500 and 1000-hour samples, only the photomicrographs of the 1000-hour samples were included in this section. The findings from the microscopic examination of each group of 1000-hour test samples are as follows:

Corrosion Test #1: All of the MA956 samples displayed some wastage either in the form of general wastage or a mixture of general wastage + localized pitting. With regard to subsurface damage, the samples exhibited very little if any noticeable penetration. In contrast, the severity of the exterior wastage noted in the 230 samples ranged from minor to (in some instances) catastrophic. The real damage to the 230 samples occurred subsurface via sulfidation/oxidation. These subsurface damage mechanisms rendered some of the samples completely consumed (e.g. almost no remaining sound metal) because of the severity of the penetration. The appearance of the 1000-hour samples exposed to the conditions of Corrosion Test #1 is shown in Figure 101 and the results of the microscopic examination are:

- The MA956 sample tested under Ash #1 exhibited minor general wastage, with no evidence of any localized attack.
- The other two MA956 samples, tested under Ashes #2 and #3, displayed localized wastage in the form of pitting with the Ash #3 sample containing the deepest pit of the series.
- All of the 230 samples exhibited significant general and localized wastage as well as substantial subsurface sulfidation/oxidation damage.

Corrosion Test #2: Corrosion Test #2 was conducted using the same temperature and ash coatings as Test # 1 but with the higher sulfur content gas. The corrosion morphology of the Test #2 samples was very similar to that observed in the Test #1 samples. Again the MA956 samples coated with Ashes #2 and #3 displayed pitting damage, while the Ash #1 sample showed only minor surface irregularity. The 230 samples all exhibited catastrophic subsurface sulfidation/oxidation. The representative microscopic appearance of the 1000-hour samples is shown in Figure 102.

Corrosion Test #3: Corrosion Test #3 was essentially the same as Test #1 with the exception of temperature, which for Test #3 was raised to 1148°C (2100°F). To reiterate, the Gas #1 mixture was used along with all three ash deposits for this test sequence. The representative microscopic appearance of the 1000-hour samples is shown in Figure 103.

In comparison to the Test #1 samples, the following Test #3 observations are noted:

- The higher temperature promoted the generation of some minor pitting in the MA956, Ash #1 sample.
- An increase in the depth of pitting was observed in the MA956, Ash #2 sample, while a noticeable decrease in the amount and depth of pitting was noted in the MA956, Ash #3 sample.
- The 230 samples all exhibited catastrophic subsurface sulfidation/oxidation.

MA956
Ash #1

MA956
Ash #2

MA956
Ash #3

Typical
Appearance of
230 Samples

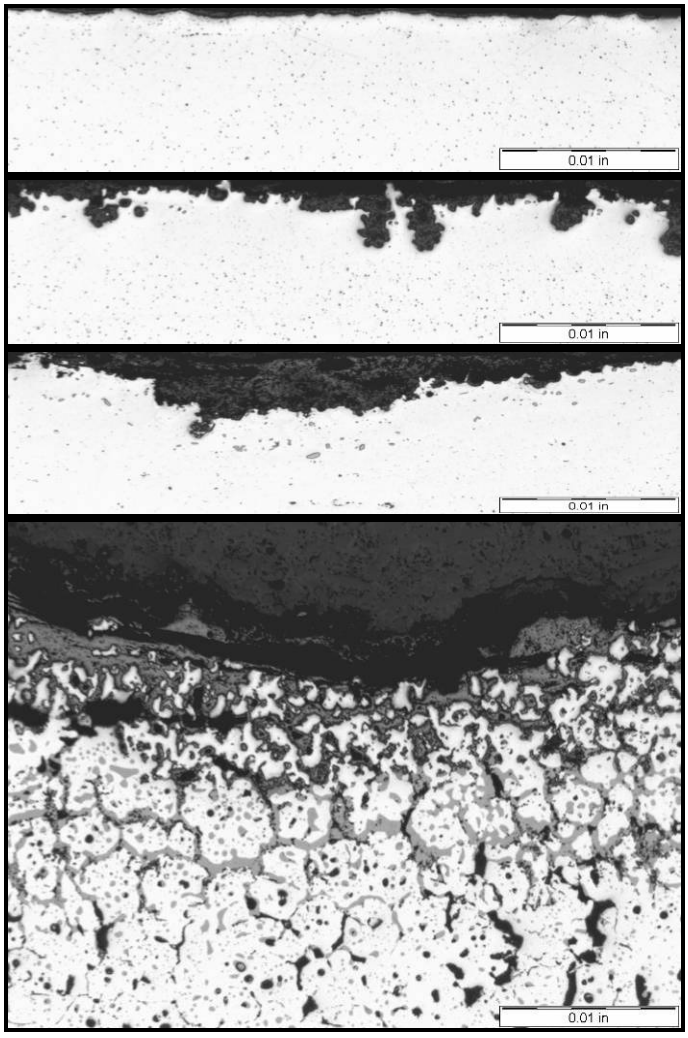

Figure 101. Representative Appearance of Test #1 1000-Hour Samples

MA956
Ash #1

MA956
Ash #2

MA956
Ash #3

Typical
Appearance of
230 Samples

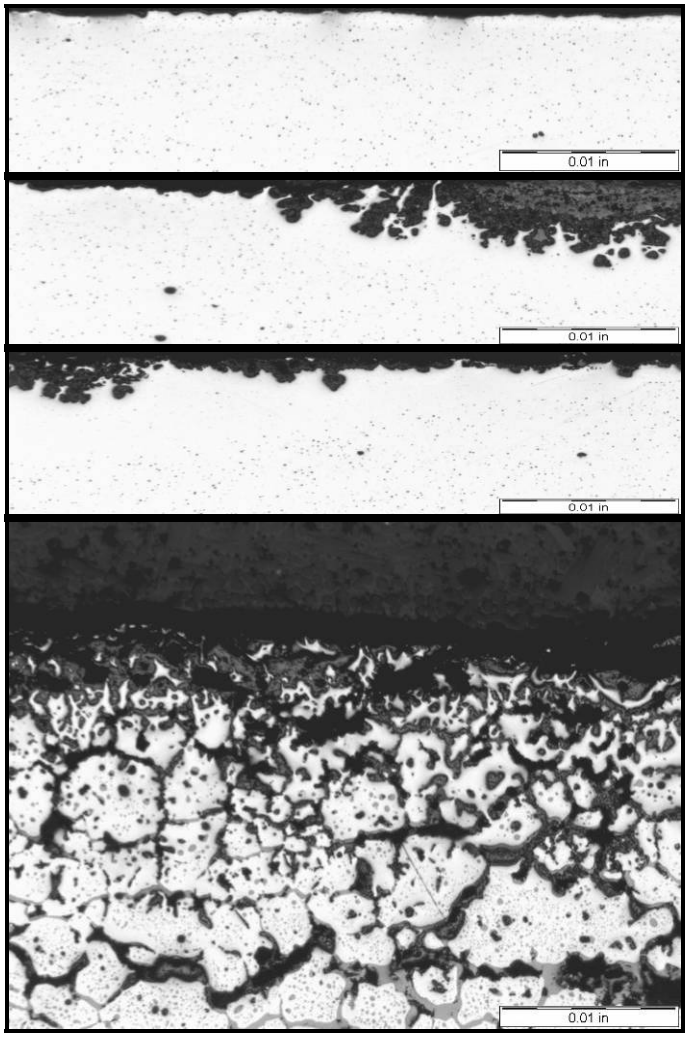

Figure 102. Representative Appearance of Test #2 1000-Hour Samples

MA956
Ash #1

MA956
Ash #2

MA956
Ash #3

Typical
Appearance of
230 Samples

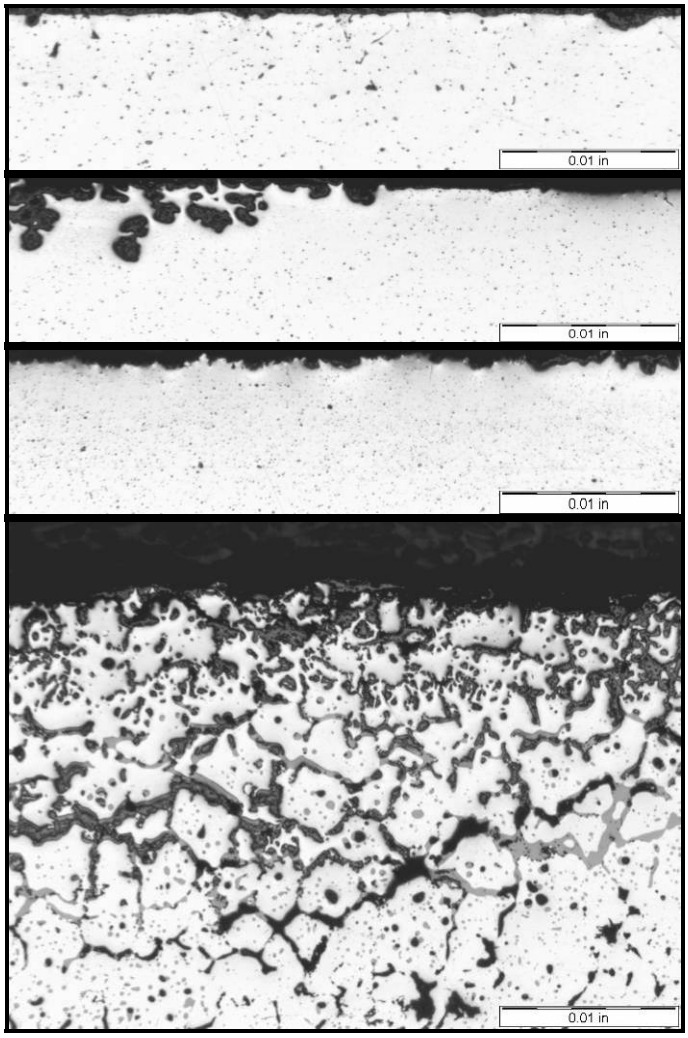

Figure 103. Representative Appearance of Test #3 1000-Hour Samples

Corrosion Test #4: Corrosion Test #4 was also conducted at 1148°C (2100°F), using all three ash deposits and Gas #2. The representative microscopic appearance of the 1000-hour samples is shown in Figure 104.

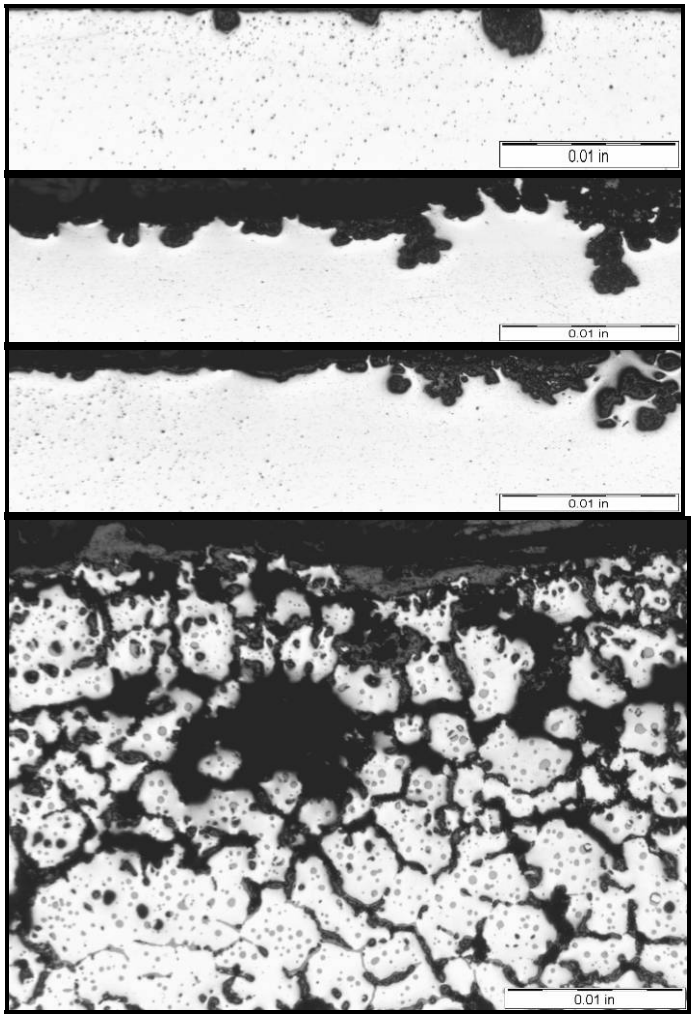

Figure 104. Representative Appearance of Test #4 1000-Hour Samples

The following statements summarize the findings as well as the contrast between this test and Test #2:

- All of the MA956 samples exhibited varying degrees of pitting damage, with the most significant damage noted in the Ash #2 sample.
- The MA956 Ash #2 and #3 samples exhibited greater pitting than was seen in Test #2 samples and the Ash #1 sample had pitting damage whereas the Ash #1 sample in Test #2 contained none.
- The 230 samples displayed significant sulfidation/oxidation that left behind very little sound metal.

Corrosion Test #5: Corrosion Test #5 was conducted at the highest temperature of 1204°C (2200°F). Gas #1 was used along with all three ash deposits. The representative microscopic appearance of the 1000-hour samples is shown in Figure 105.

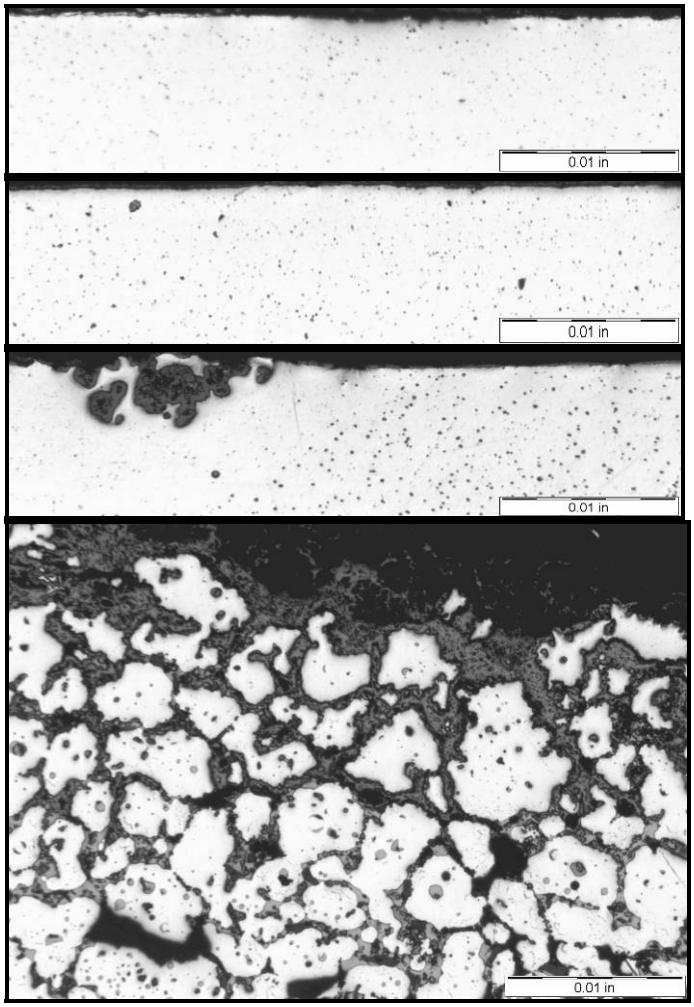

Figure 105. Representative Appearance of Test #5 1000-Hour Samples

Again the 230 samples exhibited catastrophic sulfidation/oxidation that left almost no remaining sound metal. In contrast, with the exception of the Ash #3 sample, the MA956 samples exhibited almost no evidence of exterior or subsurface attack.

Corrosion Test #6: The samples in Test #6 were also exposed to the highest temperature, 1204°C (2200°F), using all three ash deposits and Gas #2. The representative microscopic appearance of the 1000-hour samples is shown in Figure 106.

MA956
Ash #1

MA956
Ash #2

MA956
Ash #3

Typical
Appearance of
230 Samples

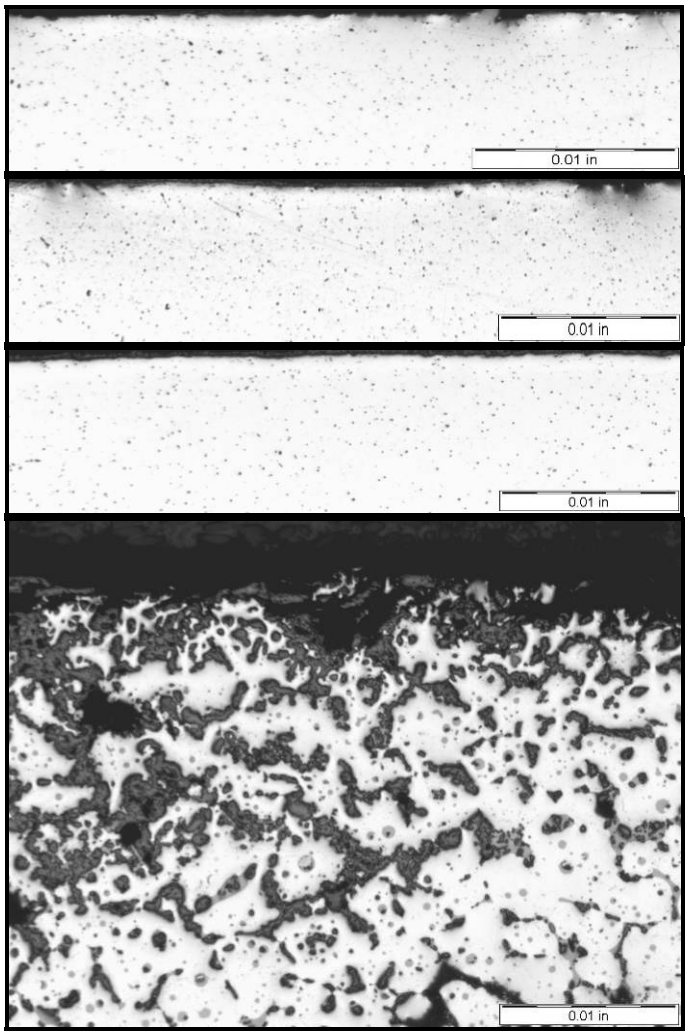

Figure 106. Representative Appearance of Test #6 1000-Hour Samples

The MA956 samples exhibited only minor pitting damage that was noted in the Ash #1 and Ash #2 samples. All of the 230 samples suffered extreme damage as a result of subsurface sulfidation/oxidation that left almost no remaining sound metal.

5.5.2.7 Calculation of Corrosion Rates

The data collected from the macroscopic and microscopic examination (i.e., thickness loss, pit depth, penetration) were combined to calculate the maximum corrosion rates (expressed in µm/100 hours). The calculated data was split into two categories: the macroscopic portion comprised of exterior wastage or descaled thickness loss (shown as "Descaled" in the graphs) and microscopic portion that encompassed cross-section thickness loss (shown as "X-section" in the graphs).

As previously discussed, a section was removed from each coupon and mounted for microscopic examination. The remaining pieces were cleaned of all scale and corrosion product using a low-pressure glass-bead blaster. The remaining thickness of the cleaned pieces was

then recorded using a digital point micrometer. The max corrosion rate (CR) for this method was obtained from the maximum of the thickness loss measurements taken on each coupon. The transverse cross section (containing the remnant corrosion products) was measured microscopically in four areas for remaining wall thickness including the depth of any observed micro-pits. These samples were also examined for signs of subsurface penetration/corrosion. The max CR was determined from the summation of the maximum of the four thickness loss measurements and the maximum observed subsurface penetration.

Corrosion Rate data for Corrosion Test #1: The CR results for the 1000-hour Test #1 samples are presented in Figure 107. The Descaled alloy 230 CRs were much lower than their X-section counterparts, which, based upon the results of the microscopic examination, is due to the significant subsurface sulfidation/oxidation damage the samples suffered.

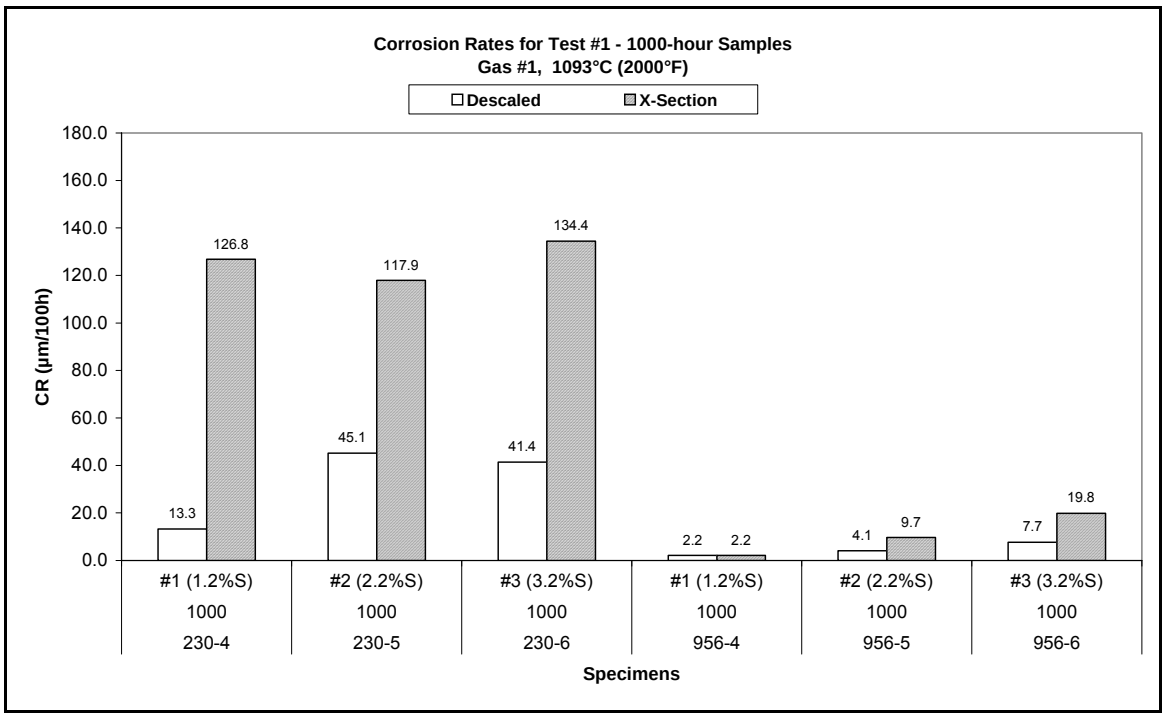

Figure 107. Maximum CR of 1000-Hour Samples from Corrosion Test #1

The MA956 samples exhibited much lower CRs than the alloy 230 samples regardless of the calculation method (e.g., "Descaled" or "X-Section"). The CR increased along with the amount of sulfur in the ash deposit. The differences observed between CR calculation methods were a result of the ability of the microscopic method to discern the depth of the incipient pits or micro-pits. A trend of increased CR was noted with the amount of sulfur in the ash deposit.

Corrosion Rate Data for Corrosion Test #2: The results for Test #2 are given in Figure 108. Examination of the alloy 230 samples revealed that they contained almost no remaining sound metal and were thus categorized as completely consumed (e.g., maximum CR). With regard to the MA956 samples, the highest CR was noted in the Ash #2 sample instead of the one tested under Ash #3. The Ash #1 sample displayed the least amount of wastage and therefore yielded the lowest CR.

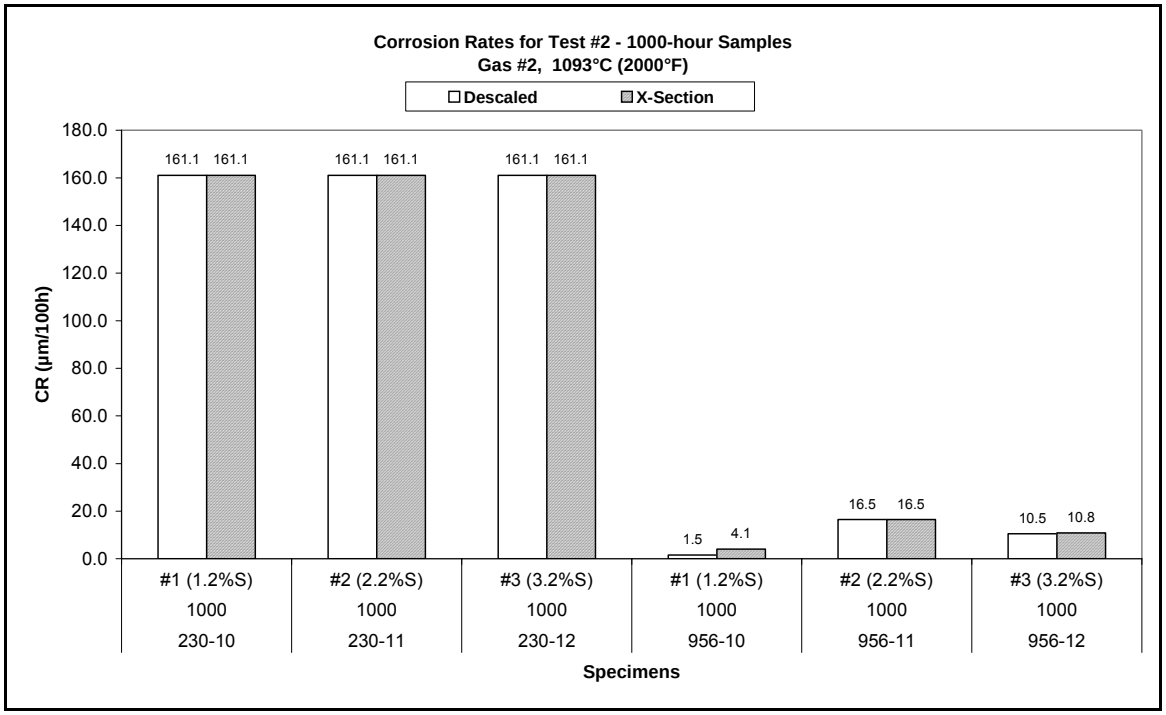

Figure 108. Maximum CR of 1000-Hour Samples From Corrosion Test #2

Corrosion Rate Data for Corrosion Test #3: Overall, the results for Test # 3 were similar to those noted in the previous two tests; extremely high CRs for the alloy 230 samples and much lower rates for the MA956. The CR data for the 1000-hour Test #3 samples are plotted in Figure 109. As previously seen, the high temperatures coupled with the sulfur in the gas and ash combined to cause catastrophic sulfidation/oxidation in the alloy 230 samples leaving behind very little sound metal. On the other hand the resiliency of the MA956 was evident as the corrosion rates of the Ash #1 and Ash #3 sample were (approximately) the same and slightly lower than their Test #1 counterparts, respectively. Another difference was that the Ash #2 sample displayed the highest CR of the three samples in Test #3, whereas, in Test #1 the Ash #3 sample exhibited the highest rate. This is a result of the micro-pitting noted in the Ash #2 sample.

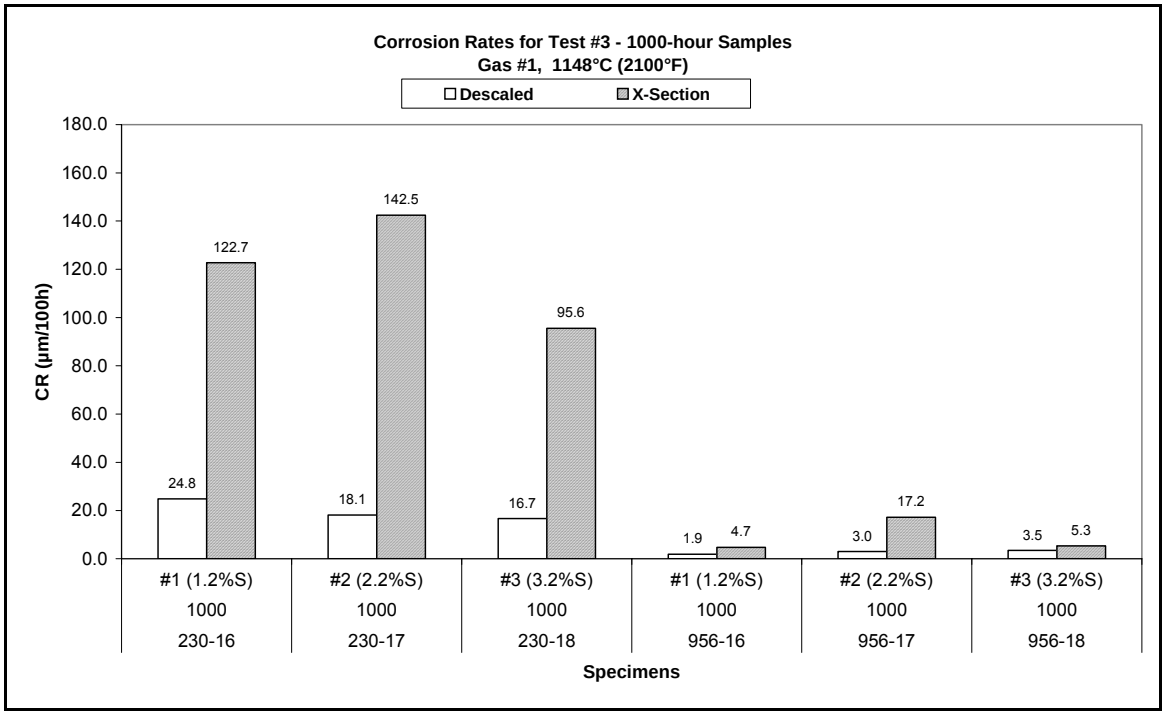

Figure 109. Maximum CR of 1000-Hour Samples From Corrosion Test #3

Corrosion Rate Data for Corrosion Test #4: The CR results for the 1000-hour samples from Test #4 are shown in Figure 110. Even though the temperature was higher, the rates for the alloy 230 samples in this test set were lower than those observed in Test #2. However, the extreme subsurface damage noted during the microscopic examination forced these samples to be categorized as completely consumed. With regard to the MA956 samples, the Ash #1 and #3 samples exhibited slightly higher CRs than those realized in Test #2, while the rate for the Ash #2 sample was approximately the same. This was a result of some incipient pits that were observed in the surface of this set of samples.

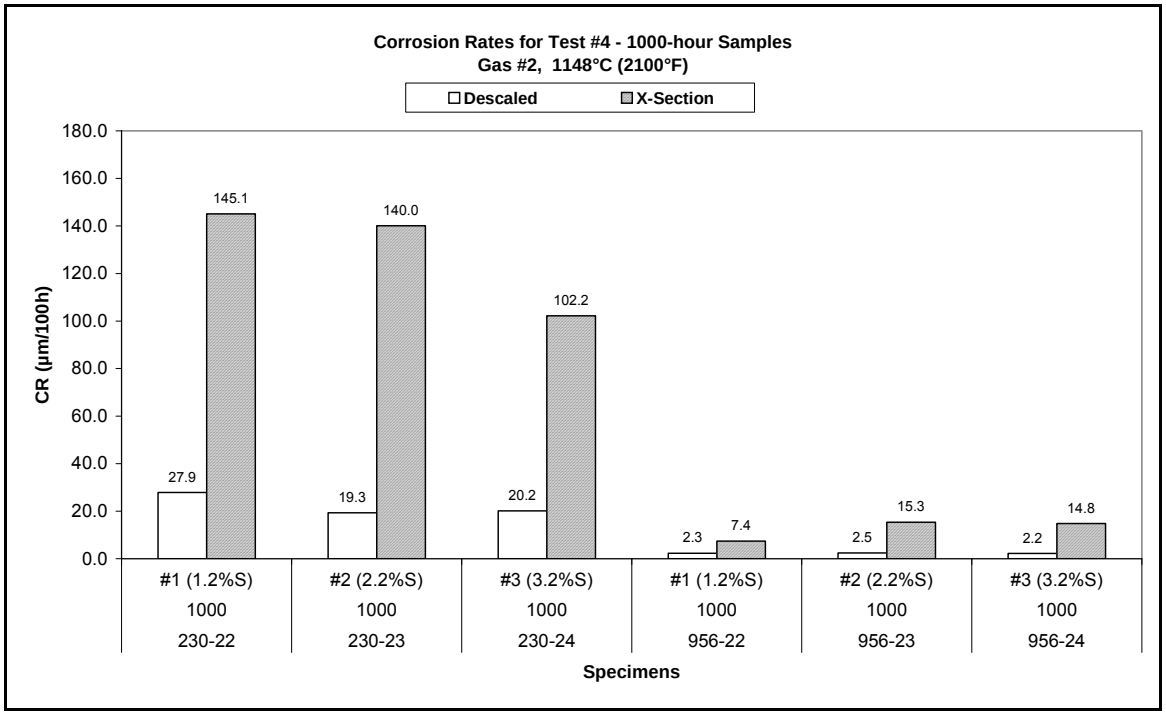

Figure 110. Maximum CR of 1000-Hour Samples from Corrosion Test #4

Corrosion Rate Data for Corrosion Test #5: Corrosion Test #5 was third in the Gas #1 series and it was conducted at the highest temperature, 1204°C (2200°F). The data for this test is shown in Figure 111. This set of alloy 230 samples displayed the highest corrosion rates with Gas #1. The extreme subsurface damage from the combined sulfidation / oxidation mechanisms rendered the samples completely consumed. Conversely, the MA956 samples exhibited rates that increased in direct proportion with the percent-sulfur in the ash deposits.

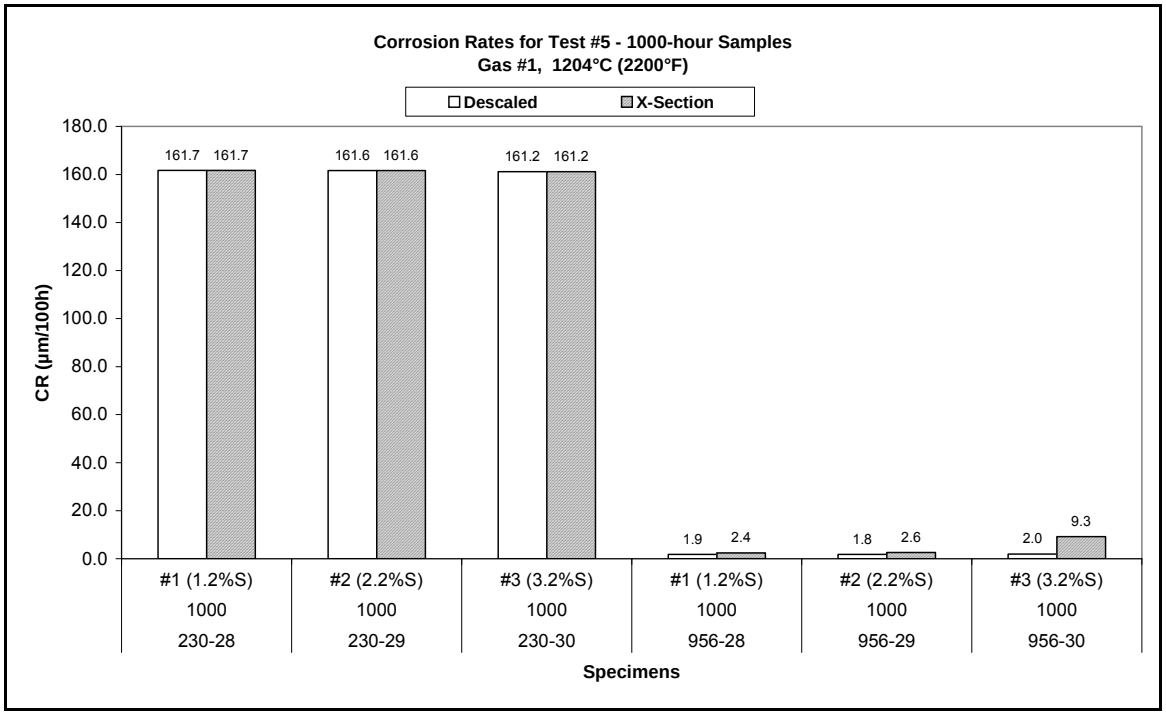

Figure 111. Maximum CR of 1000-Hour Samples from Corrosion Test #5

Corrosion Rate Data for Corrosion Test #6: This was the last in the Gas #2 series and it was conducted at the highest temperature, 1204°C (2200°F). The results are presented in Figure 112. The alloy 230 samples exhibited almost no remaining sound metal and, because of that, they were categorized as completely consumed. Thus these coupons were assigned with the maximum CR available. As was seen in Test #5, the MA956 samples had CRs that were relatively low compared to those noted in Test #2 and Test #4, with the exception of the Ash #1 sample in which some subsurface penetration of a sulfur species was noted.

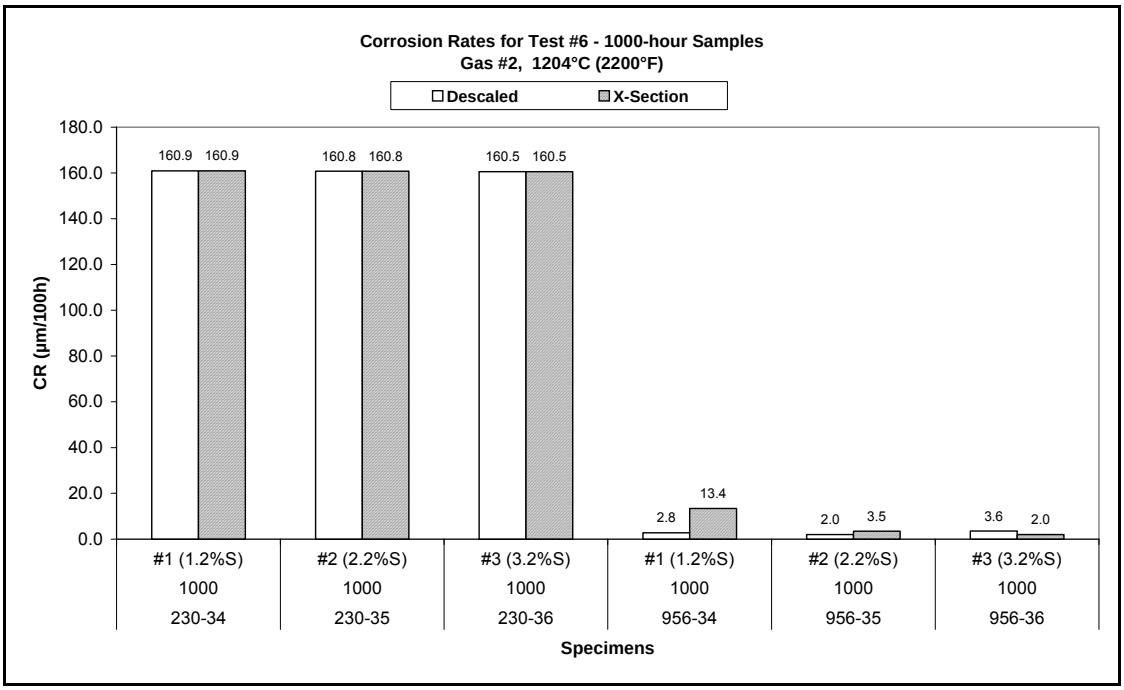

Figure 112. Maximum CR of 1000-Hour Samples from Corrosion Test #6

5.5.2.8 Regression Analysis

Regression analysis was only conducted on the MA956 samples because of the extreme wastage experienced by the 230 material. In analyzing the multiple variables, it was decided that the temperature and the percent sulfur in the ash probably had the largest influence on the samples; therefore, the data was plotted against these two variables to derive formulas for describing the corrosion. It should be noted, however, that the models derived from this plotted data should be used cautiously because they are based on a very limited amount of data. Additionally, it was decided that the X-section corrosion data would be used for the formula derivations because this data set, which included the observed subsurface damage, made it more accurate for predictive modeling and determination of remaining useful life.

5.5.2.9 Corrosion Rate versus Percent Sulfur in Ash

Gas #1 Environment: Examination of the Figure 113 plotted data revealed three distinctly different predictive curves and, more importantly, three different types of corrosion behavior. The Test #1 data (black line) showed a direct relationship between increasing percent sulfur and the corrosion rate, which was explained by the equation CR_1.

The plotted data for Test #3 exhibited a bell-shaped curve (explained by equation CR_3), which indicates an increase in the corrosion activity at the 2% sulfur level where the alkali sulfates were added to make Ash #2. This would suggest that the alkali sulfates strongly influenced the corrosion within this data set. Looking at point 3 for Test #3 shows that at this temperature the corrosion activity is significantly decreased with this mixture of alkali sulfates and chlorides. With regard to the data from Test #5, the data shows a minimal increase in corrosion from the 1% to the 2% sulfur level ash even though the 2% level contained alkali sulfates. The real change occurred from the 2% to 3% level, which would indicate that the combination of alkalis and chloride increases the corrosion at the higher temperature level 1204°C (2200°F).

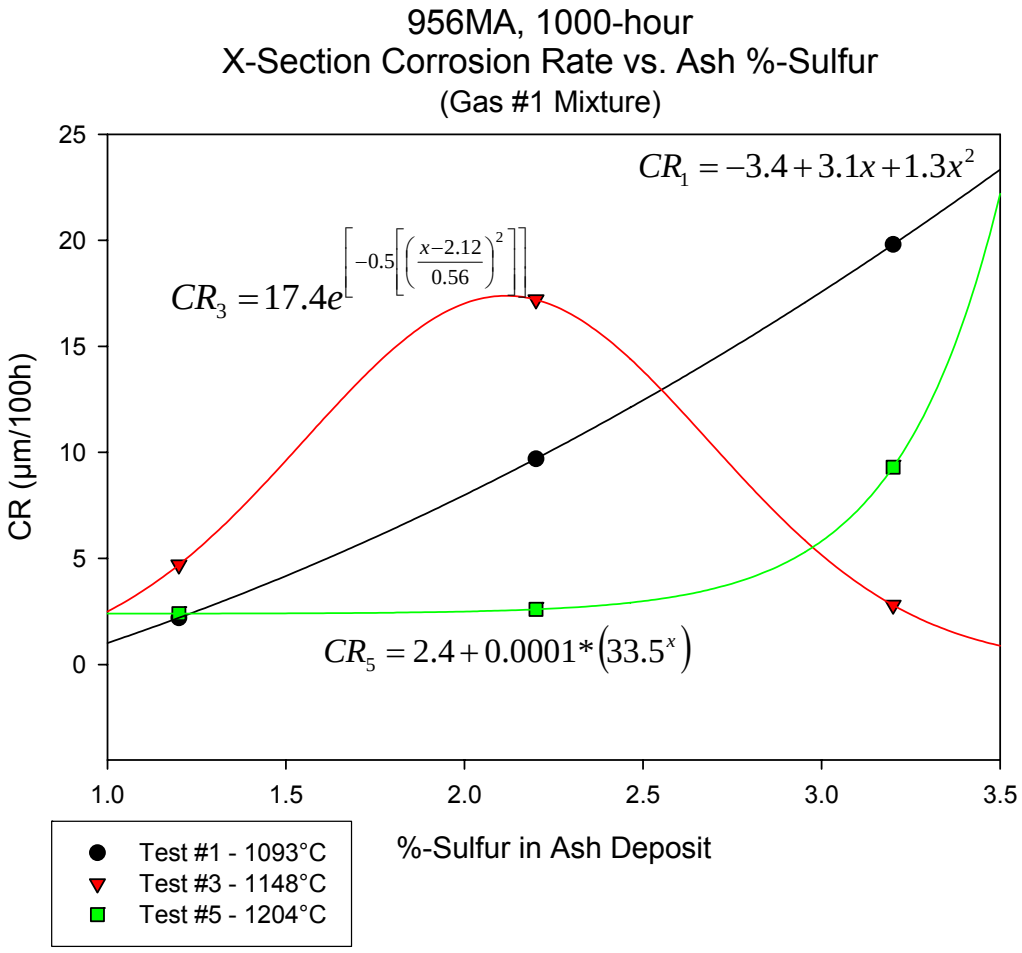

Figure 113. CR vsersus Ash Percent Sulfur for Gas #1 with Predictive Curves

Gas #2 Environment: Data for Gas #2 are plotted in Figure 114 and the resulting bell shaped curve is totally different from that of Gas #1. In the Gas # 2 environment the lower temperature samples caused the bell-shaped curve, indicating that under the reducing conditions created by Gas #2 the effect of the alkali sulfates was more pronounced than at the higher temperatures. This relationship was explained by equation CR_2. The trend for Test #4 was such that the largest increase in corrosion activity was noticed between the 1% and 2% sulfur levels, after which the corrosion was found to decrease slightly (equation CR_4). The data for Test #6 was observed to be so close to one another that it could be argued that the data is essentially the same, therefore the curve generated from this data set (equation CR_6) really should be used for academic purposes only and not to model corrosion rates based upon similar circumstances.

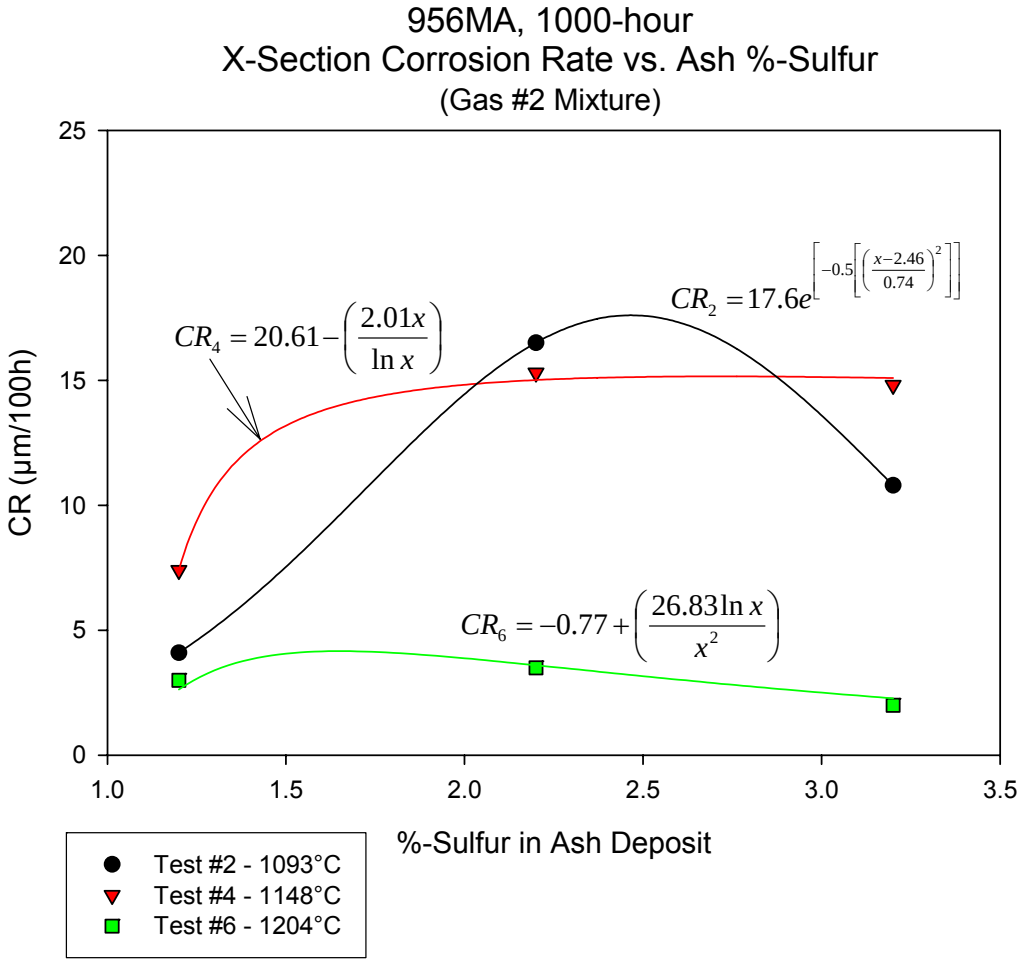

Figure 114. CR versus Ash Percent Sulfur for Gas #2 with Predictive Curves

5.5.2.10 CR Versus Temperature

Gas #1 Environment: Further regression analysis was performed to determine if any relationships could be formulated between temperature and corrosion rate. Here the data was segregated by ash composition and the corrosion rates then plotted versus the test temperatures experienced by each data set (see Figure 115). A similar (albeit shallower) bell-shaped curve was noted for both Ash #1 and #2, indicating that the sulfur and alkali sulfates were most active at 1148°C (2100°F). Their curves are represented by equations CR_7 and CR_8. The opposite was true for the Ash #3 (alkali sulfates + chlorides), which showed an inverse bell curve with more activity at the lower and upper temperature levels than at the median temperature. The curve representing this data set is expressed by equation CR_9.

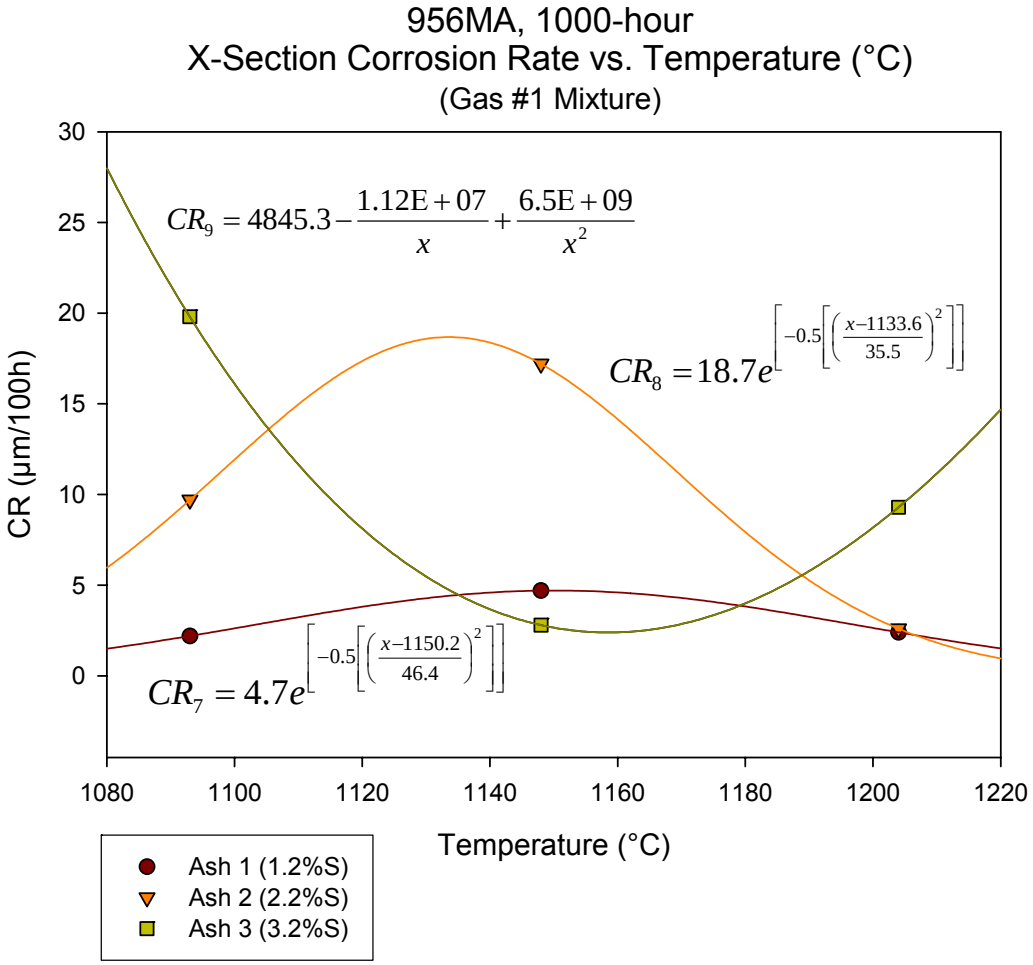

Figure 115. CR versus Temperature for Gas #1 with Predictive Curves

Gas #2 Environment: The same plot was made for the Gas #2 data and it was very different from that of Gas #1 (Figure 116). In the case of Ash #1, the data showed an increase in corrosion activity with an increase in temperature, while the opposite was true of Ash #2. It is possible that in this environment the combination of sulfur and temperature drive the corrosion activity while the addition of alkali sulfates slows it. With regard to Ash #3, the data suggest that the addition of alkali sulfates and chlorides increase the corrosion from 1093°C to 1148°C (2000°F – 2100°F) but then significantly retard the activity once temperatures climb higher. The curves are represented by the equations CR_{10}, CR_{11}, and CR_{12}.

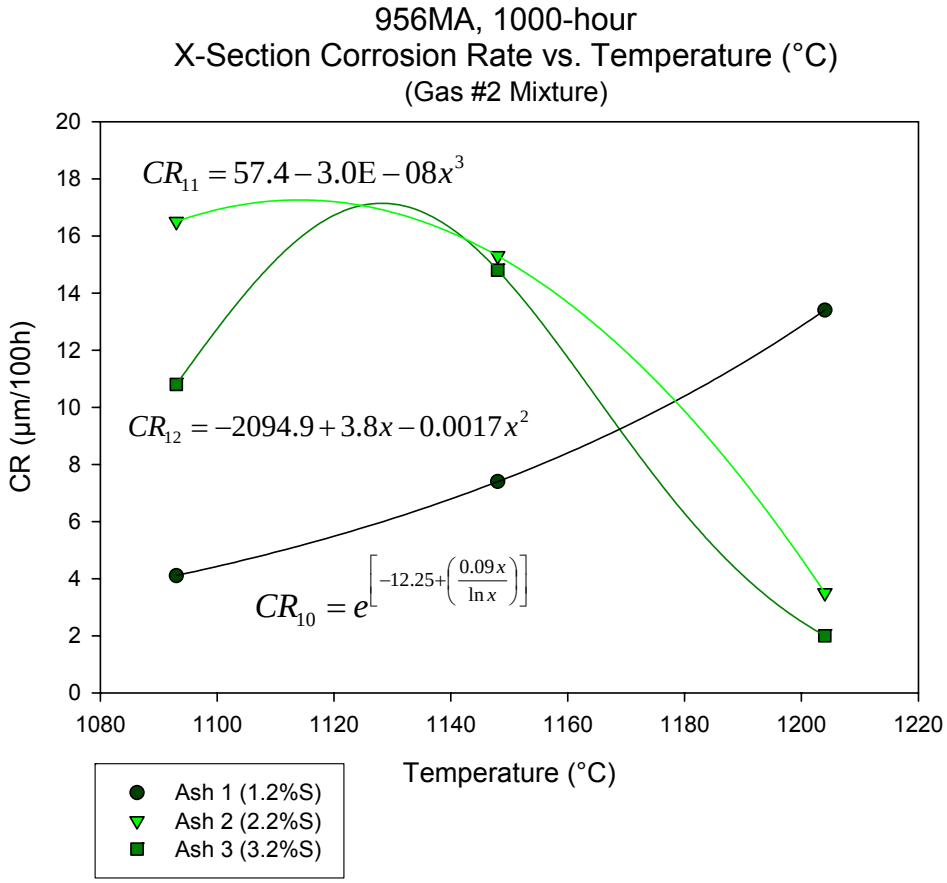

Figure 116. CR versus Temperature for Gas #2 with Predictive Curves

Again, it must be noted that the Figure 116 curves should be used cautiously as they are based on a very small amount of test data; the fact that some of the equations are very complex for a three point curve further justifies the use of caution. More testing should be done to explore the areas between those already tested so the corrosion mechanisms/activities involved can be better understood and the curves either confirmed or improved.

5.5.2.11 Fireside Environment Base Metal Discussion

The results of the corrosion experiments revealed that, overall, the MA956 alloy exhibited better corrosion resistance than the alloy 230. The active wastage mechanism in these experiments was sulfidation / oxidation proceeded by hot corrosion. Hot corrosion is separated into two categories, Type I and Type II. Type I hot corrosion is generally thought to occur between the temperature ranges of 800 to 950°C (1470-1740°F). High temperature alloys that experience Type I hot corrosion have been found to exhibit both oxidation and sulfidation. The morphology of Type I is typically characterized by a porous layer of oxides with an underlying alloy matrix depleted in chromium below which chromium-sulfides can be found. Type II occurs at lower temperatures 670-750°C (1240-1380°F) and is characterized by pitting attack with little or no internal attack.

Type I hot corrosion generally has an incubation period (with a relatively low corrosion rate) followed by a period of accelerated corrosion. The driving force behind the accelerated attack is the breakdown of the protective oxide scale by molten salts, which in our tests were provided by the ash. In addition to the sulfur in the ash, the sulfur in the gas mixtures contributed to raise the sulfur potential at the metal interface making the formation of a protective scale much more difficult.

The damage observed in the alloy 230 samples can be described as no less than catastrophic. Even with a chromium content of 22%, the material exhibited subsurface depletion of chromium to levels below 16% and a significant amount of internal chromium-sulfides. Once this stage was reached the alloy 230 samples experienced breakaway corrosion, which led (in many cases) to the samples being completely consumed e.g. wastage proceeded by intergranular sulfidation/oxidation as is seen in the photomicrographs.

In contrast, the MA956 samples performed much better than their alloy 230 counterparts predominantly as a result of its chemical composition. The fact that it does not contain nickel negates the detrimental effect of this element against the sulfidation damage produced during hot corrosion. The predominant wastage noted in the MA956 samples was pitting from the formation of molten slag species during testing. The photomicrographs detail the predominant "finger-like" morphology of the damaged areas, which upon further examination (using SEM/EDS) was determined to be areas where molten slag from the ash had breached the alumina layer to react with the base metal.

To better understand this phenomenon SEM / EDS was performed on several of the 500-hour samples that displayed evidence of incipient molten slag attack. The analysis revealed the presence of a chromium-rich and aluminum-rich oxide scale on the surface of the samples. The chromium-rich scale was the outer layer and the aluminum-rich oxide was the inner layer. Some iron- and nickel-rich sulfur species were observed on top of the outer layer indicating that diffusion of these elements occurred during the testing. Examination of the 1000-hour samples disclosed only fragments of the chrome-rich scale on top of an almost continuous layer of aluminum-rich oxide. The areas of pitting were in areas where the Al_2O_3 layer had been breached by the molten slag.

An explanation for the loss of the chromia layers in both the alloy 230 and MA956 samples is that chromia scales are known to be prone to cracking and spalling, particularly under cyclic conditions at high temperatures. This cyclic growth and spalling process eventually depletes the underlying matrix of chromium to levels below that needed to re-heal (~16%) making it susceptible to subsurface intergranular attack in the form of sulfidation (e.g., formation of chromium/nickel sulfides). It is noted that during the cooling period between test cycles, cracking of the outer scale layers on both the alloy 230 and MA956 samples were heard. Closer examination prior to the cleaning/ deslagging process revealed partial spalling of the outer scale layers in both material samples.

Additionally, it has been reported that some oxides become volatile at high temperatures. At very high temperatures (above 1000°C (1832°F)) Cr_2O_3 can react with O_2 to form volatile CrO_3. Also, the presence of moisture (present in both gas mixtures) has been shown to further promote the volatilization of Cr_2O_3. This high temperature increase in volatility also causes the chromia layer to progressively lose its protective capability.

On the other hand, the addition of aluminum to high temperature alloys has been found to be beneficial. These alloys (such as MA956) have the ability to form Al_2O_3, which has been shown to be one of the only two oxides that are capable of forming a very protective barrier against oxidation at temperatures above 1200°C (2192°F). The other oxide the other is SiO_2. The addition of aluminum has been shown to be beneficial for sulfidation resistance in Fe-Cr alloy systems. Additionally, oxide dispersion particles have been shown to stabilize the protective oxide layers at high temperatures and to increase the alloys resistance to cyclic oxidation and scale spallation.

The unique chemistry of the MA956 alloy has enabled it to perform well in these corrosion experiments; the material contained enough chromium (18%) to quickly form a protective chromia layer at the low and intermediate temperatures. This chromia layer not only protected the sample as it progressed through the higher temperature regions but it also provided corrosion protection during the time needed for the slower forming Al_2O_3 scale to form beneath it. Even with spalling (during test cycling) and volatilization of the chromia layers, the material was protected by the remaining alumina layer.

In summary:

- The active wastage mechanisms in these experiments was sulfidation / oxidation proceeded by Type I hot corrosion, which generally occurs between the temperature ranges of 800 to 950°C (1470-1740°F) and promotes both oxidation and sulfidation. The wastage morphology of materials suffering from Type I hot corrosion typically exhibit a porous layer of oxides with an underlying alloy matrix depleted in chromium and ripe with internal sulfides.

- The alloy 230 samples, despite having a chromium content of 22%, suffered depletion of chromium from the matrix and subsequent internal sulfidation, which led to breakaway corrosion (in the form of intergranular sulfidation/oxidation). Many of the alloy 230 samples were completely consumed.

- The MA956 alloy performed as well as expected with minimal material loss and subsurface attack. The wastage observed in the MA956 samples was pitting (from molten slag species) in locations where the slag breached the Al_2O_3 layer.

- SEM / EDS of the 500-hour MA956 samples revealed the presence of an outer chromium-oxide layer on top of an aluminum-oxide layer. In the 1000-hour samples the outer chromium layer was all but non-existent indicating its loss during testing.

- Chromium oxide layers are known to be prone to cracking and spalling, particularly under cyclic conditions at high temperatures. During the cooling period between test cycles, audible cracking of the outer scale layers on both the alloy 230 and MA956 samples was noted.

- At high temperatures >1000°C (1832°F) Cr_2O_3 has been shown to become volatile and react with O2 to form volatile CrO3. Also, the presence of moisture has been shown to further promote the volatilization of Cr2O3. This progressively causes the chromia layer to lose its protective capability and depletes the matrix of chromium.

- The addition of aluminum to the MA956 alloy was found to be extremely beneficial because Al2O3 is one of two oxides capable of forming a very protective barrier against oxidation at temperatures above 1200°C (2192°F). Aluminum was also beneficial in aiding against sulfidation attack.

- The MA956 alloy contained enough chromium (18%) to quickly form a protective chromia layer at the low and intermediate temperatures, thereby protecting the sample as it progressed through the higher temperature regions. This ability provided corrosion protection during the necessary time for the slower forming Al_2O_3 scale to form beneath it, which protected it during the volatilization and spalling of the chromia layers.

5.5.3 Laboratory Weld Coupon Testing for Fireside Environment

In Task 5.5.1 coupons of Incoloy MA956 and Haynes 230 were coated with coal ashes and exposed to high temperature gases in electrically heated furnaces to determine the susceptibility of these materials to corrosion. In this task, Task 5.5.2, a similar investigation was conducted on MA956 weld coupons to determine the susceptibility of the weld zones to corrosion. Since the weld coupon corrosion test could be viewed as a continuation of the prior, six test run program, Task 5.5.2 was assigned Test #7. A sketch illustrating the desired configuration and dimensions of the welded specimens was sent to EWI (Figure 117). Specimens containing welds joining MA956 to MA956 made by inertia friction welding and flash butt welding were supplied along with specimens containing welds joining MA956 to Inconel 601 by inertia friction welding. *(Note weld test specimens were removed from welds in 63.5 mm (2.5-inch) O.D. and 6.35mm (0.25-inch) wall thickness).*

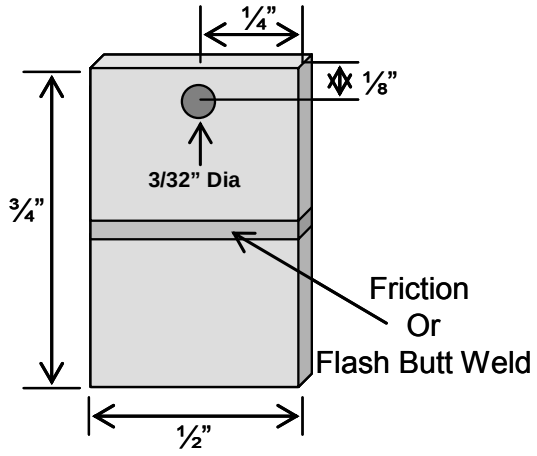

Figure 117. Corrosion Test Coupon Configuration

5.5.3.1 Test Parameters and Matrix

The weld coupon tests were conducted at 1093°C (2000°F) with Task 5.5.1's most corrosive gas composition (Gas # 2) and all three ashes (see Table 21 through Table 24 for gas and ash compositions).

5.5.3.2 Pre-Characterization of Test Coupons

The test coupons were provided by EWI and consisted of:

- 5 Sample Type "B" – MA956 joined to Inconel 601 by inertia friction welding (IFW)
- 5 Sample Type "C" – MA956 joined to itself by flash butt welding (FBW)
- 5 Sample Type "D" – MA956 joined to itself by IFW

The nominal compositions of the materials are given in Table 26. The test coupons were pre-characterized by first giving them a unique identifying number that was stamped near the top of the coupon (outside of the testing area). After being identified, thickness measurements were taken at six locations on each coupon and the results averaged. These measurements were utilized to determine the performance of the materials after exposure.

Table 26. General Composition of Test Materials

Material	C	Si	Mn	Al	Co	Cr	Ni	Mo	Ti	Fe	W	Other
MA956	0.014	0.02	0.07	4.74	0.02	18.7	0.04	—	0.37	Bal	—	0.48 Y_2O_3
601	0.10 max	0.05 max	1.0 max	1.0-1.7	—	21.0-25.0	58.0-63.0	—	—	Bal	—	S:0.015 Cu: 1.0 max

5.5.3.3 Description of Test Facility and Test Procedure

The weld corrosion tests were conducted in the test facility using the same test equipment and the same test procedures, i.e., specimens mounted in a fixture, fixture placed inside an electrically heated furnace, gas synthesized/blended from cylinders, ash replenished every 100 hours, and specimens removed after 1000 hours of exposure for analysis.

After exposure, the coupons were left in the uncleaned condition so that a section with corrosion product could be carefully removed. These sections were mounted for a cross-sectional metallurgical analysis and determination of the sound-metal thickness. The mounts were subjected to a dry polishing procedure in an effort to retain any possible chloride species. The depth of subsurface attack, specifically on the MA956 weld surface, was measured on the mounted cross sections as was the remaining wall thickness of the coupons. Based on the collected data the maximum metal wastage (MMW) and corrosion rate (CR) were calculated.

The remaining portion of each coupon was then thoroughly cleaned of all corrosion products using a low-pressure glass-bead blasting technique for subsequent visual and stereoscopic examination of the exposed surfaces. It should be mentioned that while wall thickness measurements were made pre and post exposure, the variability in coupon thickness within the weld regions made definitive quantification of gross wall loss impossible to ascertain. Thus, corrosion rates were determined strictly through microscopic evaluations.

5.5.3.4 Macroscopic Examination

Mounted cross-sections of the welds in the post-exposure condition are shown in Figure 118. Macroscopic examination of the samples consisted of evaluating the welded coupons, after cleaning, both visually and stereoscopically for evidence of gross wall loss. Due to the variable thickness of the coupon samples, particularly along the weld, changes in wall thickness could not be quantified by thickness measurements.

Corrosion Test #7 – Welded Specimens: Corrosion testing of the welded coupons was conducted at 1093°C (2000°F) using Gas #2 (15% CO_2 + 5% $H_2O_{(v)}$ +1% SO_2 + 2% O_2 + Bal N_2) and all three ash deposits. The macroscopic appearance of the coupon samples after cleaning and exposure is shown in Figure 119 through Figure 121.

For the most part, MA956 weld surfaces exhibited little to no evidence of visually observable gross metal loss under all ash conditions. The surface of the dissimilar weld exhibited some attack on the 601 side of the fusion zone.

5.5.3.5 Microscopic Examination

The sections removed from the test samples were carefully mounted for microscopic examination to quantify the extent of metal loss caused by pitting and possible contributions caused by subsurface attack; the combination of which was used for the determination of CR. Microscopic examination of the MA956 weld joints revealed evidence of wall loss in the form of shallow, highly localized pits. Pitting did not appear to be preferentially deeper or more prevalent along the MA956 weld surface, relative to the base metal. No evidence of subsurface penetration was noted.

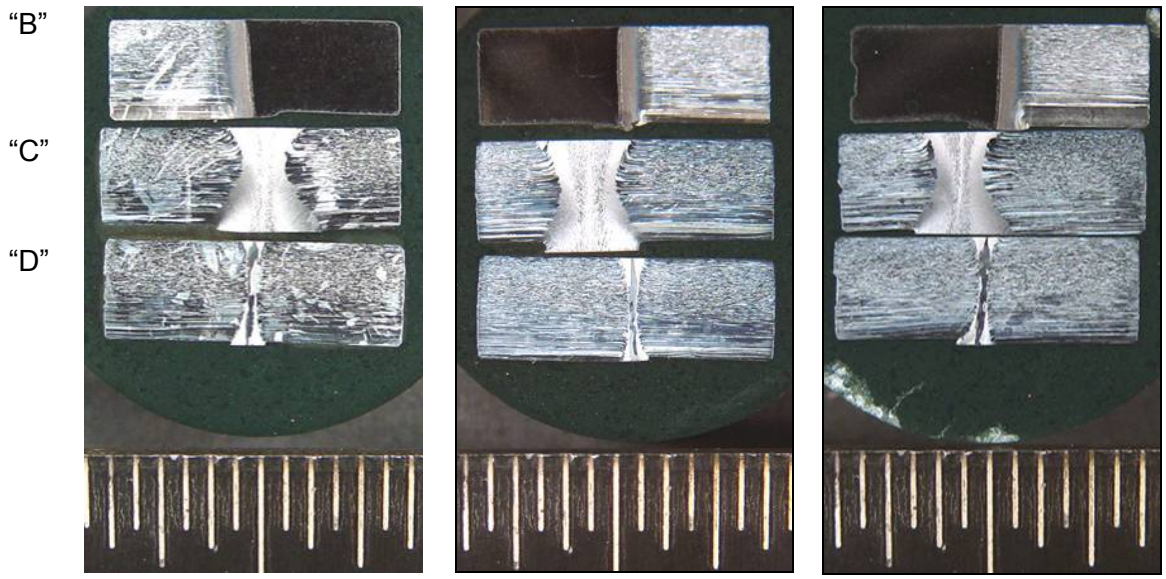

Figure 118. Etched Cross Section Highlighting the Microstructure of MA956 Base Metal and Weld

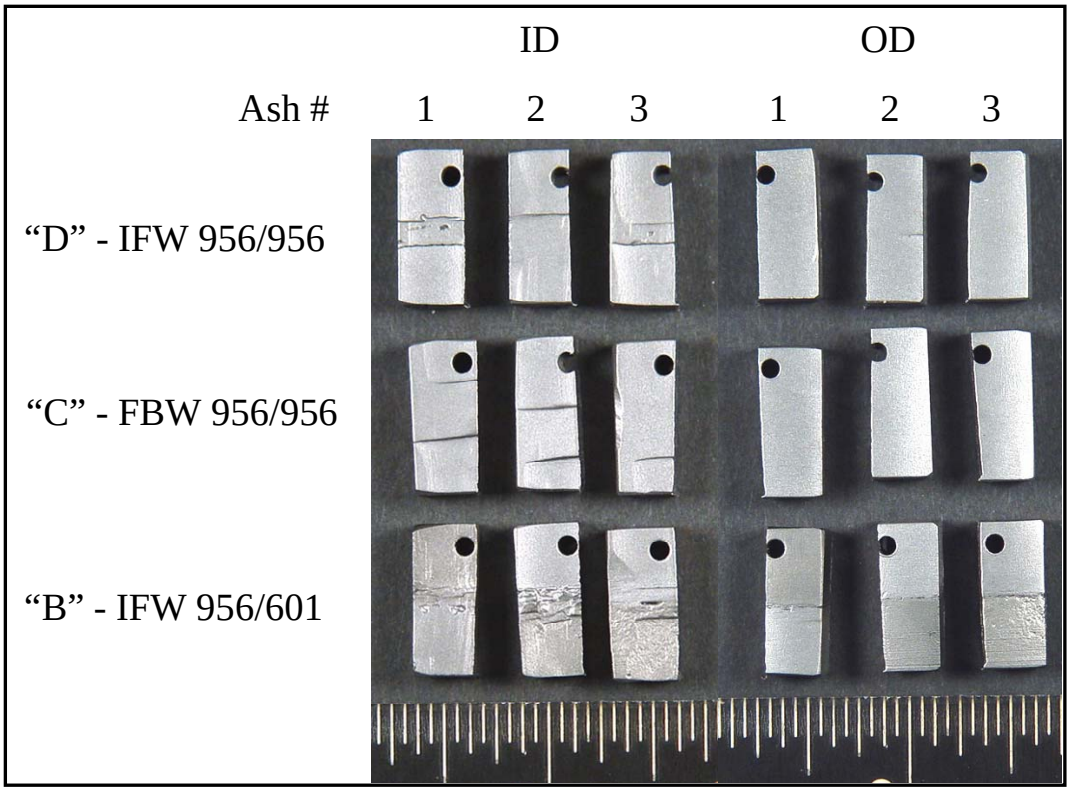

Figure 119. Test #7 Weld Samples After Cleaning

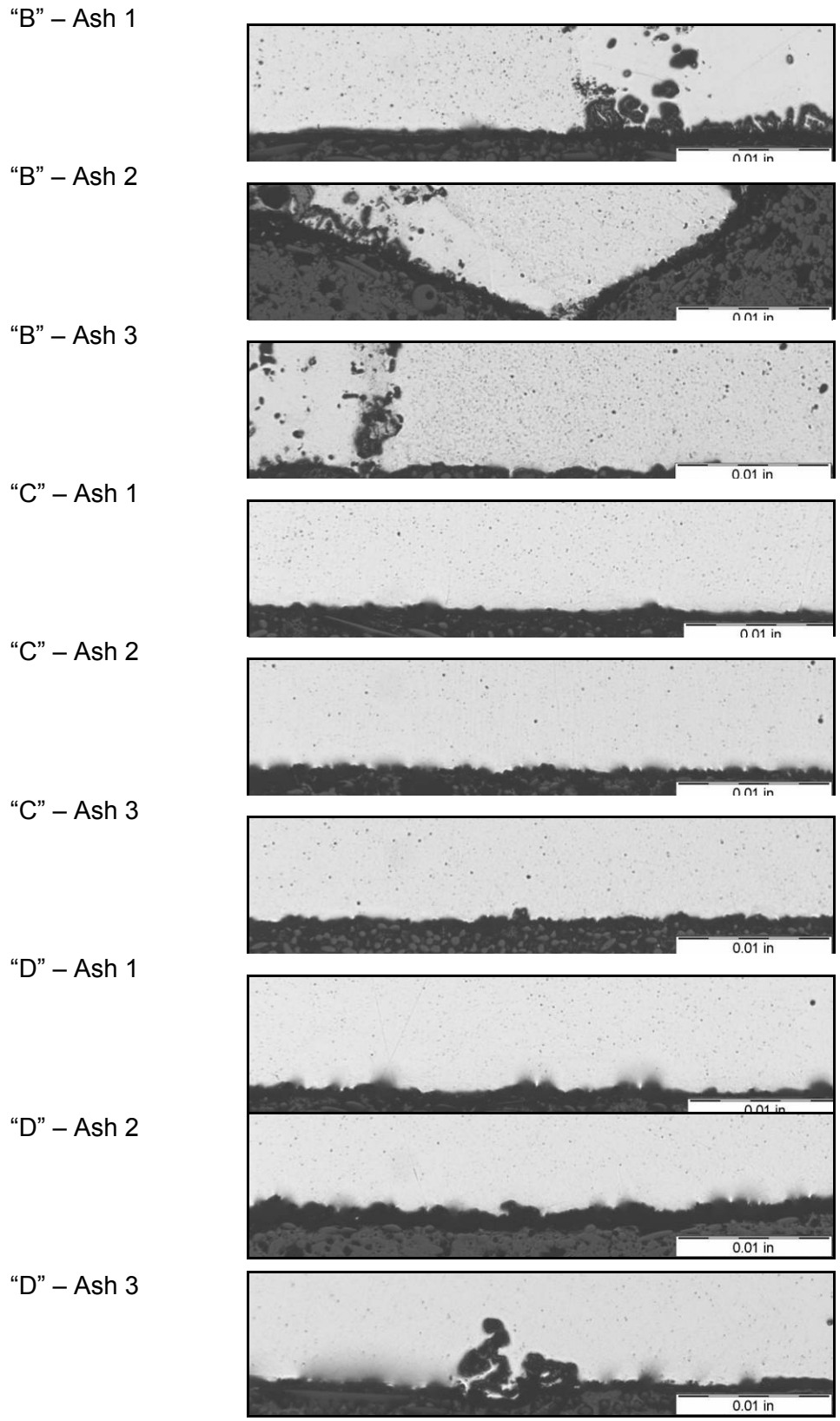

Figure 120. Representative Appearance of Test #7 Weld Surfaces (ID)

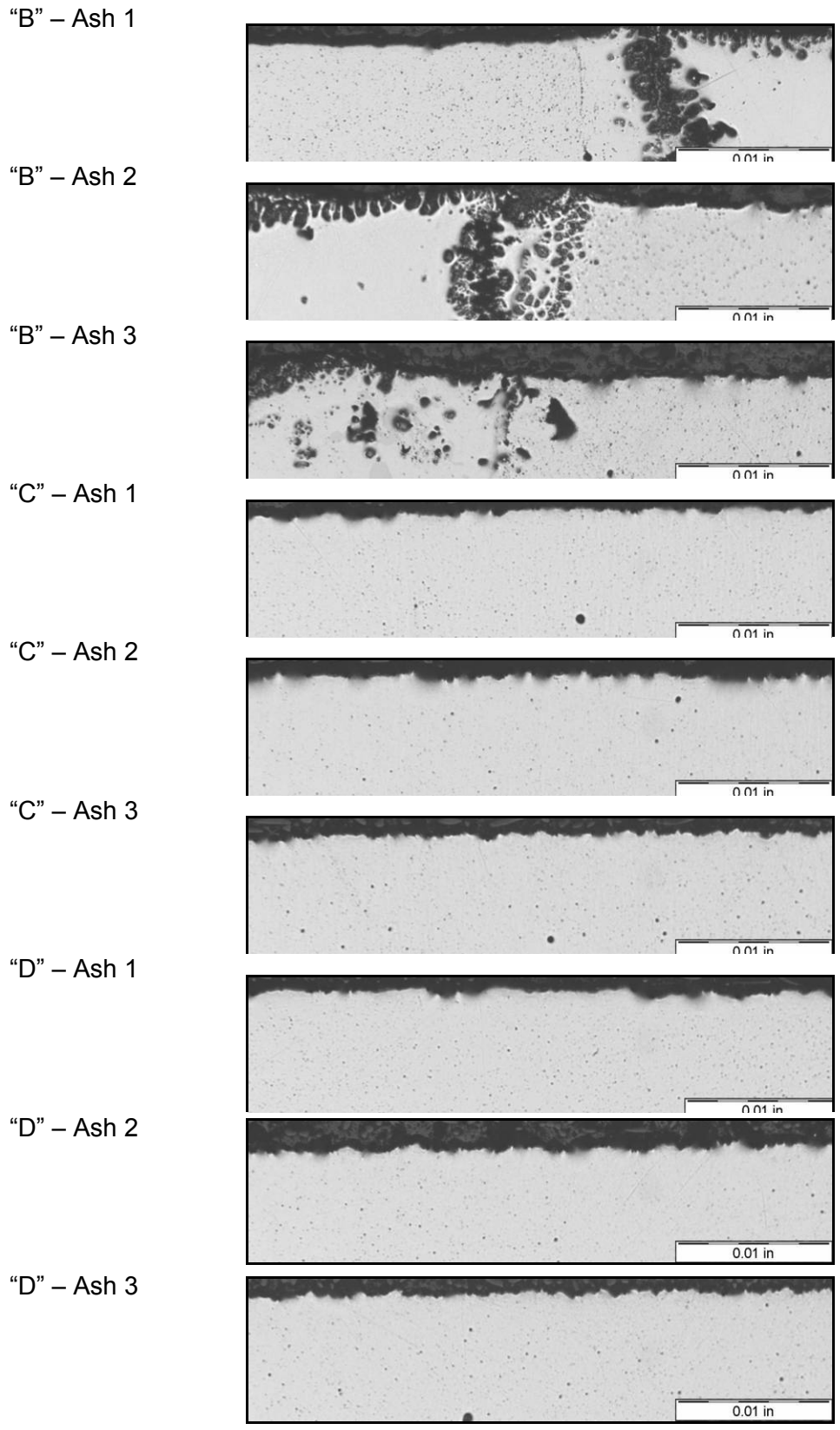

Figure 121. Representative Appearance of Test #7 Weld Surfaces (OD)

Evaluation of the dissimilar weld, specifically the transition zone between the weld and alloy 601 specimens, indicated the presence of microstructural phases and the possible presence of penetration species throughout the entire sample thickness for all ash conditions. Considerable subsurface oxidation was also apparent in alloy 601 in all locations away from the weld. The transition zone between the weld and the MA956, on the other hand, only showed evidence of shallow pitting; however, several cracks and fissures were noted within the weld heat affected zone.

5.5.3.6 Calculation of Corrosion Rates

Due to considerable variability in wall thickness across the weld surfaces, accurate wall thickness measurements before and after exposure could not be made. Thus, the maximum corrosion rates for the welded samples upon exposure to the different ash conditions were determined by combining the maximum measured wall loss resulting from pitting with the maximum measured depth of subsurface penetration. Since the evaluation of the 601 material was not an integral part of this investigation, only the results for the MA956 welds are presented.

The corrosion rate data for the MA956 welded specimens after 1000-hour of exposure to 1093°C (2000°F) and Gas #2 for the three different ashes are shown in Figure 122. The reported corrosion rates are comparable to those previously reported for the MA956 base metal.

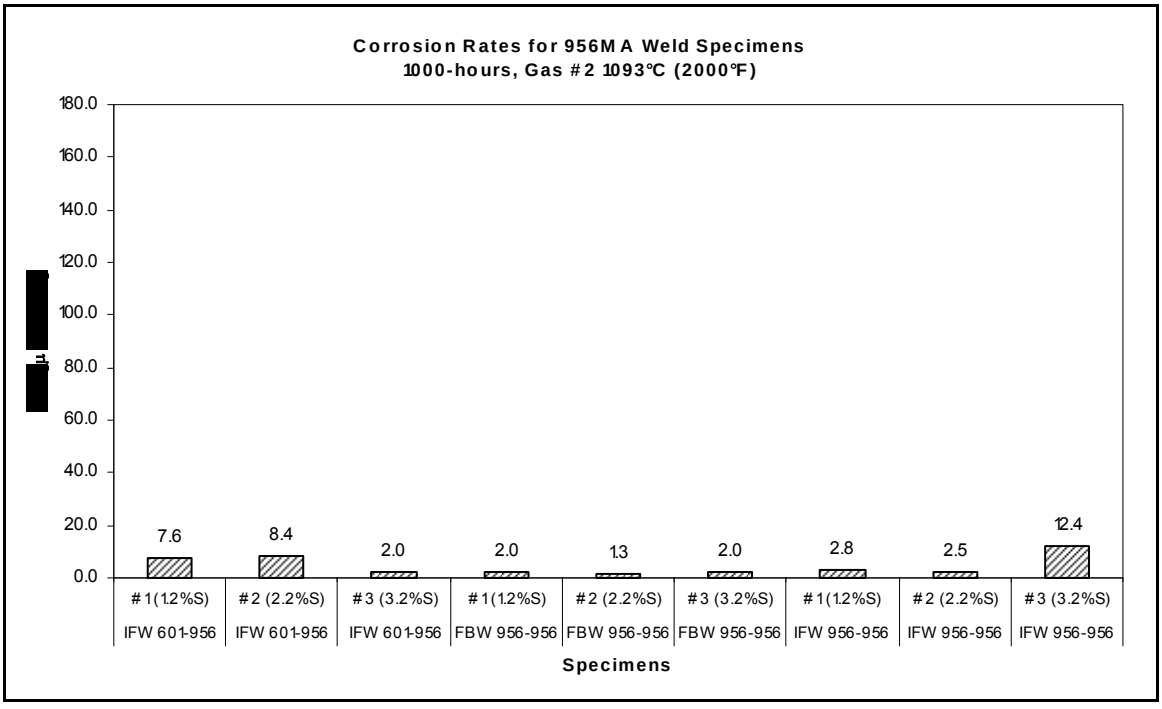

Figure 122. Maximum CR for Test #7 1000-Hour MA956 Weld Samples

5.5.4 Field Exposure Testing – Fabrication of Probes

Early in the project specimens from an initial Vision 21 probe were microscopically evaluated that had been exposed in Gallatin Unit 2 for approximately three months in 2003. Photomacrographs and photomicrographs of the evaluation are presented below. The probe had operated in the temperature range 871°C - 982°C (1600°F - 1800°F) before failing at a MA956 to 602CA fusion-welded joint as displayed in Figure 123. This figure indicates that a fusion type weld is not appropriate in joining MA956. The purpose of the evaluation was to characterize the surface condition of the specimens that were still attached to the probe, i.e., the eight specimens to the left of the elbow in the top photomacrograph in Figure 123. The specimens included MA956 (from 3 locations), 800H, 602CA, 693, 617, and 230. The surfaces were initially documented using a light microscope (Figure 124 through Figure 129), and then they were further examined in a scanning electron microscope (SEM) equipped with an energy dispersive x-ray (EDX) analyzer. Backscatter images obtained in the SEM evaluation are shown in Figure 130 through Figure 132.

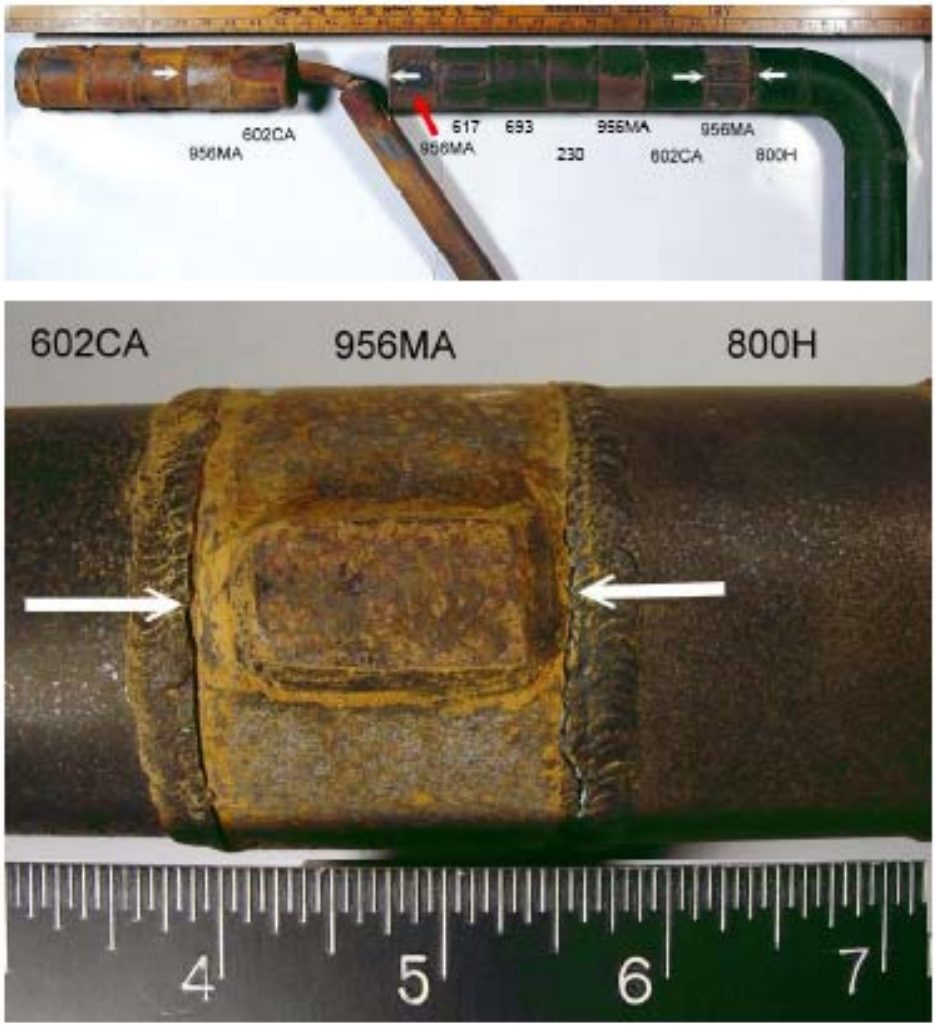

Figure 123. Appearance of Probe Exposed for 3 months in Gallatin Unit 2 at Temperatures in 870°C-980°C (1600°F-1800°F) Range

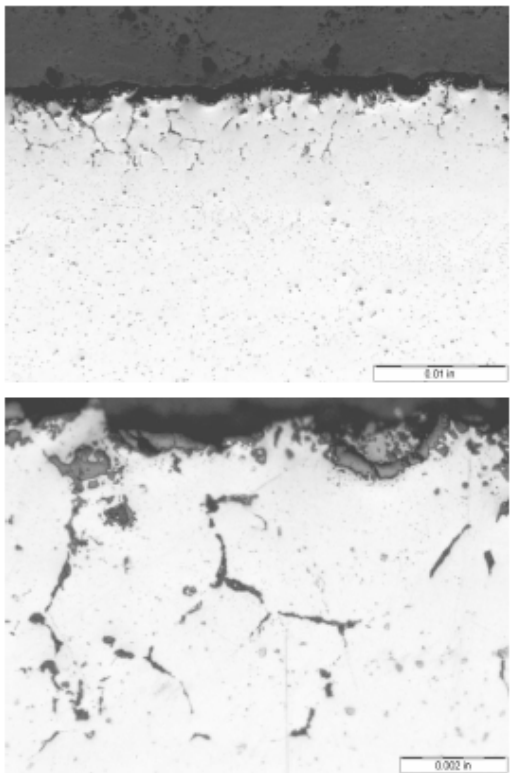

Figure 124. Alloy 800H

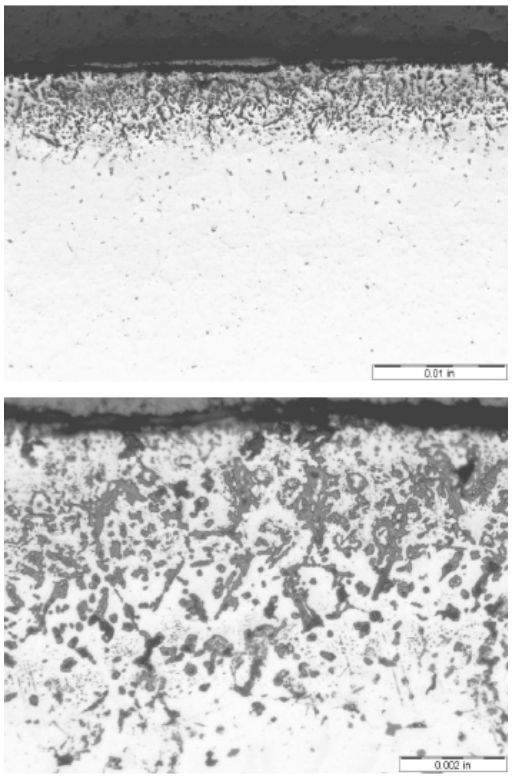

Figure 125. Alloy 617

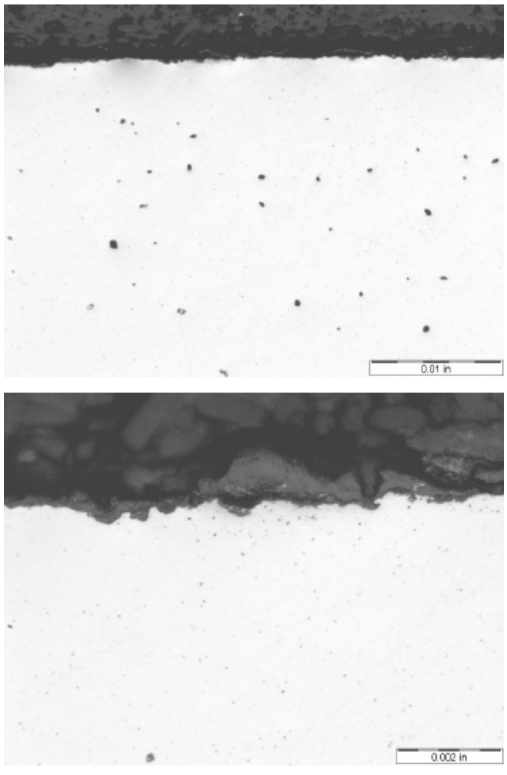

Figure 126. Alloy MA956

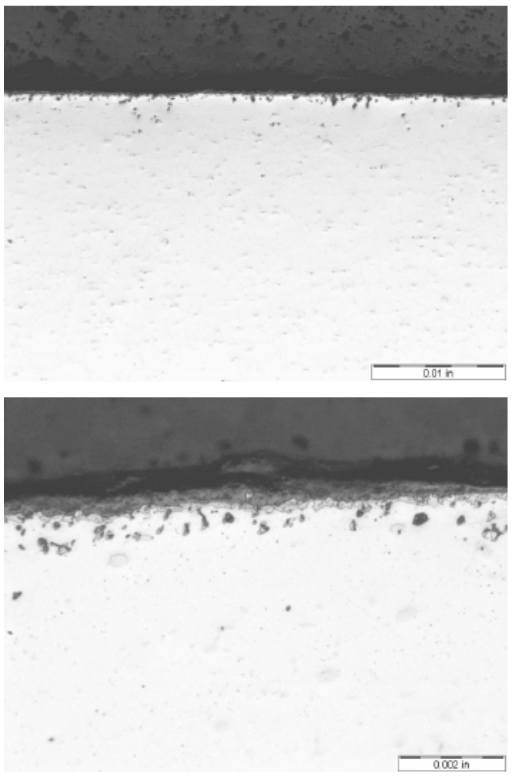

Figure 127. Alloy 230

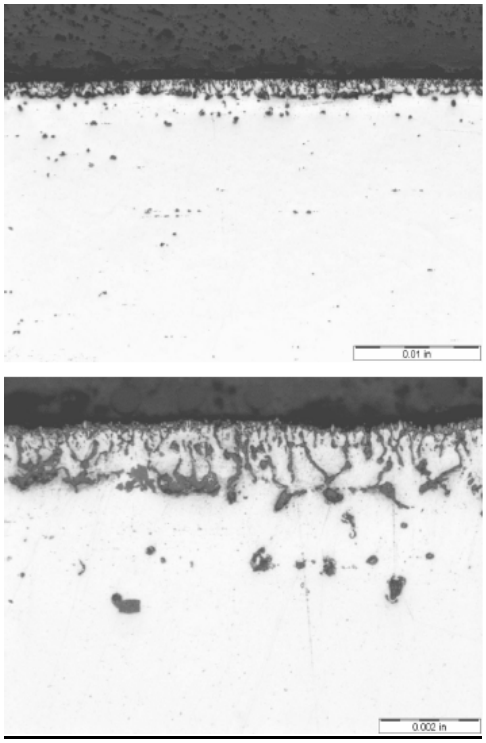

Figure 128. Alloy 602CA

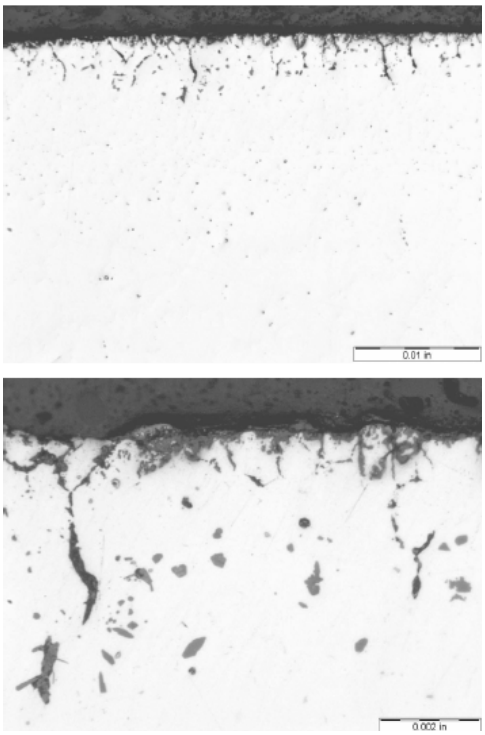

Figure 129. Alloy 693

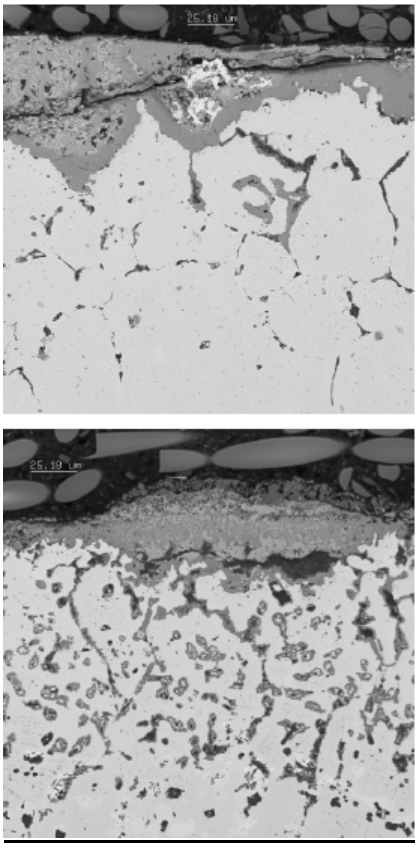

Figure 130. Top: Alloy 800H; Bottom: Alloy 617

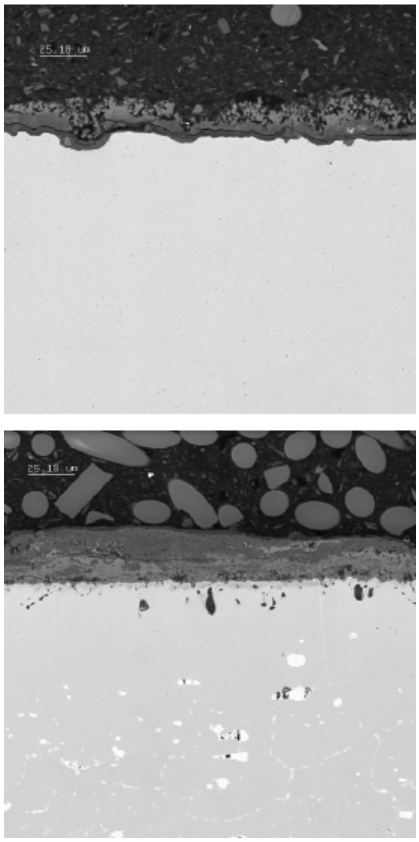

Figure 131. Top: Alloy MA956; Bottom: Alloy 230